ARPA Order No. 529

AD671901

EXPERIMENTS ON RESISTIVE INSTABILITIES IN A TOROIDAL PLASMA

by

Kenneth Stuart

Research Report No. PIBMRI-1379-67
Contract No. NONR 839(38)
December 1967

Sponsored by
Advanced Research Projects Agency

Monitored by
Office of Naval Research
Washington, D. C.

Distribution of this document is unlimited.

JUL 19 1968

POLYTECHNIC INSTITUTE OF BROOKLYN
DEPARTMENT OF ELECTROPHYSICS
Long Island Graduate Center
Farmingdale, New York 11735

Reproduced by the
CLEARINGHOUSE
for Federal Scientific & Technical
Information Springfield Va 22151

BEST
AVAILABLE COPY

ARPA Order No. 529

Research Report No. PIBMRI-1379-67
Contract No. NONR 839(38)

EXPERIMENTS ON RESISTIVE INSTABILITIES IN A TOROIDAL PLASMA

by

Kenneth Stuart

Polytechnic Institute of Brooklyn
Department of Electrophysics
Long Island Graduate Center
Farmingdale, New York 11735

Research Report No. PIBMRI-1379-67
Contract No. NONR 839(38)

December 1967

Distribution of this document is unlimited.

Reproduction in whole or in part is permitted for any purpose of the United States Government.

Sponsored by

Advanced Research Projects Agency

Monitored by

Office of Naval Research
Washington, D. C.

ACKNOWLEDGEMENT

The author is indebted to Professor E. Levi for many useful discussions and constant encouragement during the course of this dissertation. Also, the development of the toroidal structure by K. T. Lian and the assistance of Dr. J. Freidberg during the construction of the primary windings are gratefully acknowledged. Appreciation is also expressed to Professor H. Farber for his generous advice concerning various aspects of the experiment.

The author also wishes to thank Mrs. Evelyn Cooke for the typing and Mrs. Rita Gnaffo for the drafting of figures that comprise this dissertation.

This research has been conducted, in part, under Contract No. NONR 839(38) sponsored by the Advanced Research Projects Agency, ARPA Order No. 529, Program Code No. 5730, and was monitored by the Office of Naval Research, Washington, D. C. Reproduction in whole, or in part, is permitted for any purpose of the United States Government.

AN ABSTRACT

EXPERIMENTS ON RESISTIVE INSTABILITIES IN A TOROIDAL PLASMA

by

Kenneth Stuart

Adviser: Enrico Levi

Submitted in partial fulfillment of the requirements
for the degree of Doctor of Philosophy (Electrophysics)

June 1968

Visual observations made on a pulsed toroidal plasma indicate that the current carrying plasma sheet breaks up into filaments parallel to the direction of the current and perpendicular to the direction of the magnetic field. This process involves the annihilation and fusion of initially opposite magnetic flux lines and leads to a final configuration which corresponds to a lower energy state. Such a state, however, would not be accessible in the absence of dissipation since its attainment requires slippage of the plasma across magnetic flux lines. The operating mechanism must then be associated with a resistive instability of the type first predicted by Furth, Killeen, and Rosenbluth and also by Coppi, Greene and Johnson in Physics of Fluids, Volume 6, 1963. Observations of resistive instabilities under laboratory conditions is of particular interest because these modes are held responsible for many astrophysical and geophysical phenomena such as solar flares and auroras as well as anomalous diffusion rates in fusion devices.

The experimental setup consists of a plasma filled ring-shaped container of rectangular cross section, where a discharge is induced by means of an iron cored transformer. The time development of the current distribution in the plasma is determined with the help of a combination of magnetic probes and an S. T. L. Image Converter Camera. Optical spectroscopy is used to calculate the temporal variation of electron number density and temperature.

It is found that the plasma forms near the inner cylindrical wall, where the primary winding is located, and moves radially outward as time progresses. The radial speed depends on the mass density and magnetic field associated with the plasma in accordance with the snowplow model. Concurrently with the outward motion a resistive instability develops, which breaks the current sheet into separate rings. The wavelength of the instability and therefore the number of rings depend on the geometry of the primary winding and on the initial perturbation it introduces in the field distribution. It was found that for a primary winding having N equal segments, the initially uniform plasma sheet split into N + 1 rings.

Theory predicts that the "tearing" and "rippling" modes of a resistive instability develop with an exponential growth rate that is a function of the resistivity, mass density, magnetic flux density, and plasma thickness. The experiments confirm this functional dependence. Also consistent with the theory is the influence of wavenumber on the growth rate for the two modes mentioned above.

TABLE OF CONTENTS

TABLE OF FIGURES AND GRAPHS

LIST OF TABLES

CHAPTER 1

INTRODUCTION

There are many reasons for investigating instabilities and the confinement of plasmas. These problems are basic to various physical phenomena, proposed fusion devices, propulsion systems and MHD generators. At present, there is much interest in resistive instabilities since some plasma configurations which may be stable in the absence of dissipation become instable for finite electrical resistivities. In particular, instabilities of the resistive type are held responsible for astrophysical and geophysical phenomena such as solar flares and auroras as well as anomalous diffusion rates in fusion devices.

The first theoretical papers written on the topic of resistive instabilities where written by Furth, Killeen, and Rosenbluth[1], and Coppi, Greene, and Johnson[2] in 1963. Experimental evidence of a resistive instability in a theta pinch was reported by Bodin[3] about the same time. Bodin's experiment showed the plasma breaking up into several filaments. Experimental and theoretical papers by Kvartskava[4] and Komarov[5,6] respectively are interesting because they investigate spatially periodic plasma structures which can arise from resistive instabilities.

It is recognized that there should always be a balance of theoretical predictions and supporting experimental data if possible. It is often difficult to design an experimert to isolate and examine a specific instability, however. So at the present time, material devoted to the theory of resistive instabilities far outweighs experimental evidence. As a matter of fact a policy paper[7] by the AEC pointed this out and suggested that experimental efforts be intensified towards the isolation of types of instabilities. It is with this viewpoint the thesis was conducted. This thesis is essentially experimental and presents mainly data supporting the existence of resistive

instabilities in a toroidal plasma composed of hydrogen at a pressure of 500 microns. At a much lower pressure, 50 microns, data supporting the existence of Rayleigh-Taylor instabilities is presented.

Observations made on a pulsed toroidal discharge at 500 microns pressure indicate that the current carrying plasma sheet, see Figure I-1, breaks up into filaments parallel to the direction of the current and perpendicular to the direction of the magnetic field. This process involves the annihilation and fusion of initially opposite magnetic flux lines and lends to a final configuration which corresponds to a lower energy state. Such a state, however, would not be accessible in the absence of dissipation since its attainment requires slippage of the plasma across magnetic flux lines. Thus the operating mechanism must be associated with a resistive instability.

At a much lower pressure, i.e. 50 microns, the plasma moves outward at a high radial speed in accordance with the snow plow model. The acceleration of the interface between the magnetic field and the plasma produces flutes along the surface of the plasma. See Figure I-2. These flutes may be interpreted as Rayleigh-Taylor instabilities, and the wavelength of the flutes can be related to viscous damping [8].

Chapter II presents some physical models that provide insight into the theory of resistive instabilities. A derivation of Rayleigh-Taylor instabilities for zero resistivity and of the damping effect produced by finite viscosity follows. A description of the toroidal discharge and method of excitation is given in Chapter III. Chapter IV is concerned with instrumentation of the experiment which includes voltage and current measurements, magnetic probes, high speed photography, spectrograph, and scanning monochromater. The experimental findings are given in Chapter V. These include data from measurements of magnetic field, electron temperature, resistivity, electron density, and photographs from which the growth rate of the various instabilities may be calculated.

Chapter VI presents conclusions about the measurements of various plasma parameters, the observations of both resistive and Rayleigh-Taylor instabilities and their relationship to respective theoretical predictions.

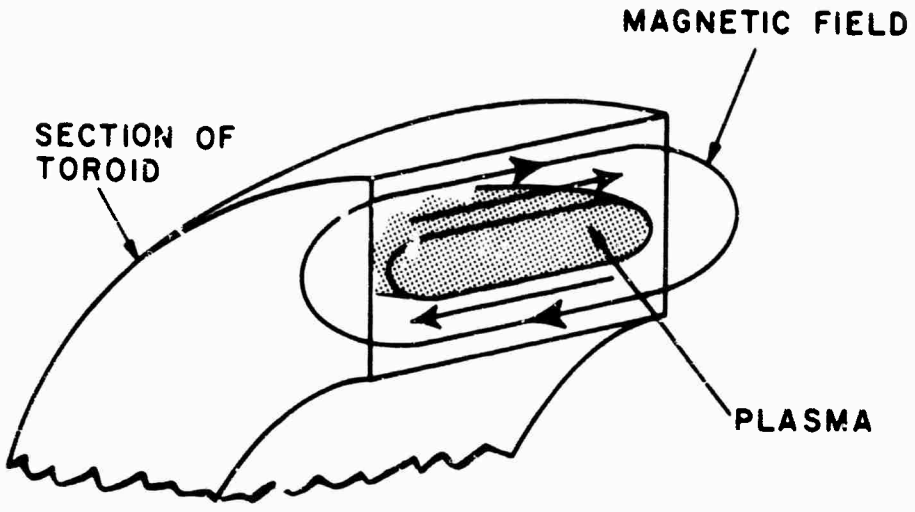

PLASMA SHEET BEFORE BREAK-UP

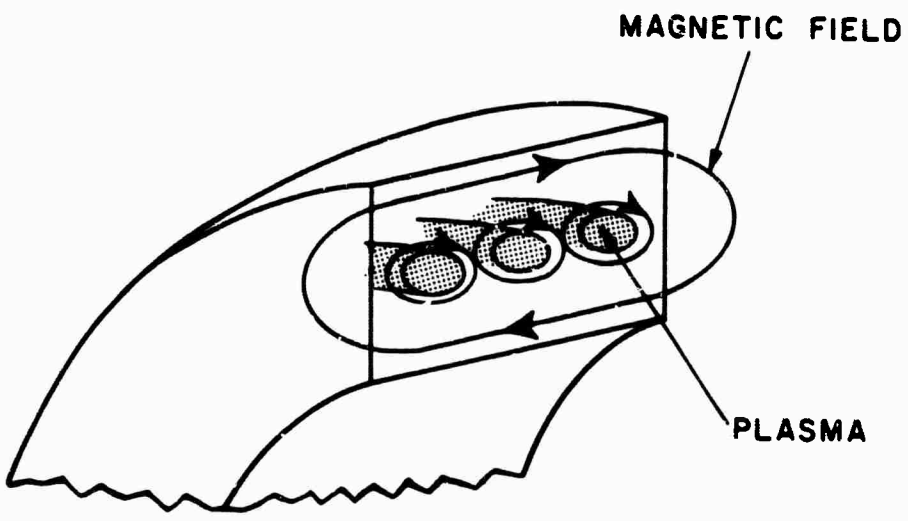

PLASMA SHEET AFTER BREAK-UP

The effect of a resistive instability

Figure I-1

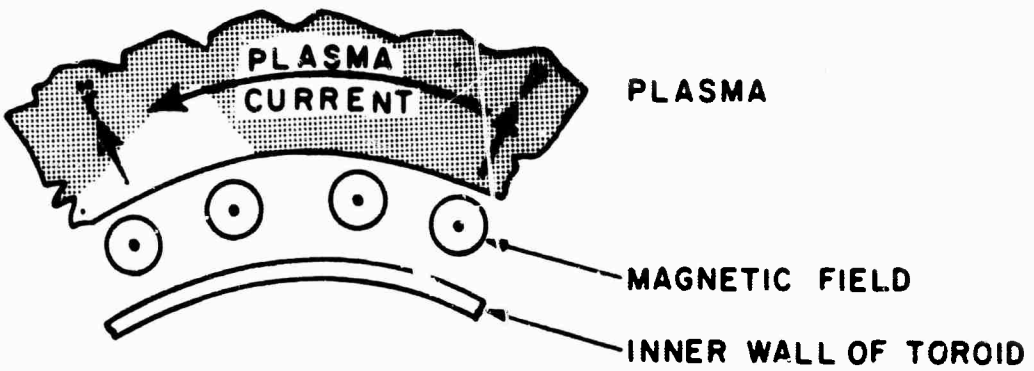

PLASMA SHEET MOVING RADIALLY OUTWARD

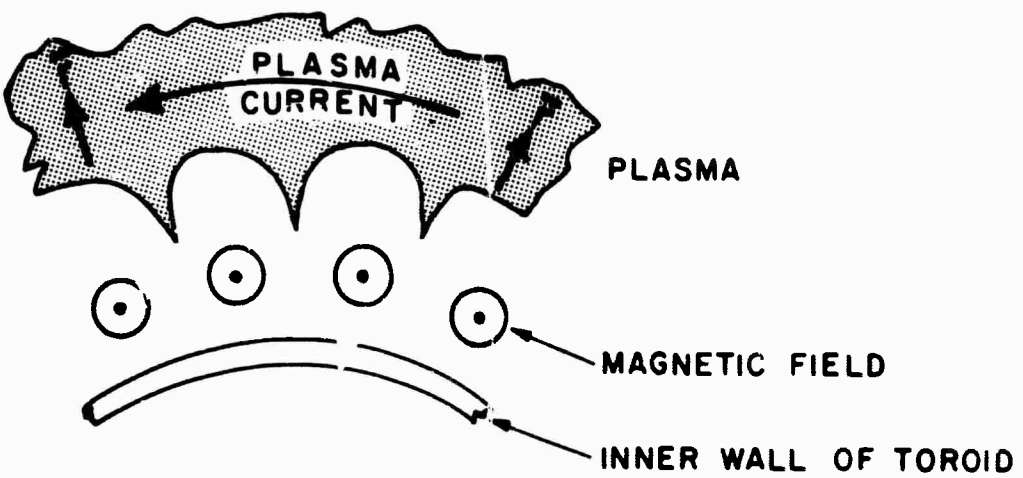

DEVELOPMENT OF FLUTES

The effect of a Rayleigh-Taylor
Instability

Figure I-2

BLANK PAGE

CHAPTER II

THEORETICAL BEHAVIOUR OF THE INSTABILITIES

The experimental configuration is a toroidal current carrying plasma whose cross-section is nearly rectangular or sheet-like. This configuration is described in Chapter III. In any case the experimental plasma when approximated as a sheet pinch takes on the geometry as discussed by Furth, Killeen, and Rosenbluth[1]. The following physical interpretation of resistive instabilities follows their treatment.

Shown first in Figure II-1 is a sketch of a sheet pinch indicating the principal axis and magnetic field supported by the current carrying plasma. The plasma sheet has a thickness characterized by a.

We start with Ohm's law, which is :

$$\eta \underline{J} = \underline{E} + \underline{V} \times \underline{B} \qquad 2.1)$$

and if we choose a frame of reference in which the electric field intensity E vanishes (Bis time invarient) equation 2.1) becomes

$$\eta \underline{J} = \underline{V} \times \underline{B} \qquad 2.2)$$

The motor force, $\underline{J} \times \underline{B}$, on an element of fluid is

$$\underline{Fm} = \underline{J} \times \underline{B} = \frac{\underline{B}(\underline{V}\cdot\underline{B}) - \underline{V}B^2}{\eta} \qquad 2.3)$$

It is seen from Figure II-1 and equation 2.3) that only fluid motion in the y direction results in a force and furthermore this force is a restoring one. So equation 2.3) becomes

$$\underline{Fm} = -\frac{\underline{V}B^2}{\eta} \approx -\underline{Y}_0 \frac{V_y (B')^2 (\sigma a)^2}{\eta} \qquad 2.4)$$

$\epsilon << 1$ and ϵa is the thickness of a small layer about $B = 0$ where $B \sim B'(\epsilon a)$, and the prime $\rightarrow \frac{d}{dy}$. Inspection of the equation above shows that the plasma motion along the y axis, transverse to B, is hampered. In fact for $\eta \rightarrow 0$, the plasma is "frozen" to the flux lines. On the other hand, at a point where B is almost zero we find that $\underline{Fm}$ is correspondingly weak so that the plasma can diffuse easily. The region in which this happens we characterize by a length of ϵa units.

For an instability to occur then, a force must be exerted of magnitude $|Fm|$ and opposite in direction to the restoring force. Also we expect that the instability starts in the region ϵa. The power associated with the restoring force is of the order

$$P \sim - \underline{V} \cdot \underline{Fm}$$

or

$$P \sim \frac{V_y^2 (B')^2 (\epsilon a)^2}{\eta} \qquad 2.5)$$

Any instability that occurs will be observed in the xy plane. In general, the wavelength of the instability ($\lambda = \frac{2\pi}{k}$) is much larger than ϵa so that the direction of propagation of the instability is along the x axis rather than the y axis. Therefore the instability is assumed to have the following functional dependence.

$$F(x, y, t) = F_1(y)\, e^{jkx}\, e^{\omega t} \qquad 2.6)$$

The power associated with the instability is then

$$P_{instab.} = \frac{d}{dt} \left(\frac{1}{2} \rho V_x^2 \right) = \frac{d}{dt} \left[\frac{1}{2} \rho \left(\frac{\lambda}{\epsilon a} V_y \right)^2 \right] \qquad 2.7)$$

where

$$\frac{V_x}{\lambda} = \frac{V_y}{\epsilon a}$$

since at low velocities the plasma is practically incompressible.

Simplifying equation 2.7) and equating it to the restoring power we have

$$\frac{4\pi^2 \omega \rho V_y^2}{k^2(\epsilon a)^2} = \frac{V_y^2 (B')^2 (\epsilon a)^2}{\eta}$$

Then the thickness of the unstable layer ϵa is given by the following :

$$\epsilon a \sim \left[\frac{4\pi^2 \omega \rho \eta}{k^2 (B')^2}\right]^{1/4} \qquad 2.8)$$

In this experiment two specific modes connected with resistive inatabilities are of interest. The modes have been termed the "rippling" mode and the "tearing" mode by F. K. R. The rippling mode has been associated with the gradient in the resistivity that exists across the width of the plasma sheet as shown in Figure II-2. Note that the positions of minimum resistivity and zero magnetic flux density along the y axis are not identical. Physically we can see the mechanism for the rippling mode by examining the three regions of the plasma sheet in Figure II-2. Assume first that a small element of fluid in Region 1 is given an upward velocity V_y. This carries low resistivity fluid into a high resistivity region. Consequently a first order current density J_1 will flow into the plane of the drawing. A motor force, $\underline{J}_1 \times \underline{B}$, is generated that opposes the upward velocity, V_y. It follows that this region is stable. Likewise examination of region 3 shows that it is stable. Pushing a fluid element down in this region produces a J_1 into the plane of the drawing. The subsequent $\underline{J}_1 \times \underline{B}$ is upward. In Region 2, however, an element of fluid moving upward carries a high resistivity into a low resistivity region creating a $\underline{J}_1$ that is out of the plane of the drawing. The motor force is now found to be upward along the y axis. This region is unstable.

Mathematically, we start with equation 2.2) and expand η and J into zero and first order components.

$$\eta_o \underline{J}_1 + \eta_1 \underline{J}_o = \underline{V} \times \underline{B} \qquad 2.9)$$

The driving force for the rippling instability is

$$\underline{F}_{rippling} = J_1 \times B = - \frac{\eta_1 \underline{J}_o \times \underline{B}}{\eta_o} - \frac{\underline{V} B^2}{\eta_o}$$

Since the above equation is valid for a small region ea about B = 0, the second term on the right is dropped. We now have

$$\underline{F}_{rippling} = - \frac{\eta_1 \underline{J}_o \times \underline{B}}{\eta_o} \qquad 2.10)$$

The resistivity η is now assumed to obey the continuity equation below.

$$\frac{\partial \eta}{\partial t} + V \cdot \nabla \eta = 0$$

Expanding and retaining only the first order terms we have

$$\omega \eta_1 + V_y \eta_o' = 0 \qquad 2.11)$$

Solving for η_1 and rewritting equation 2.10) we get the following result.

$$\underline{F}_{rippling} = \frac{V_y \eta_o'}{\omega \eta_o} \quad \underline{J}_o \times \underline{B}$$

But $$\nabla \times \underline{B} = \mu_o \underline{J}_o$$

so we have $$\underline{J}_o \times \underline{B} = \frac{1}{\mu_o} \nabla \times \underline{B} \times \underline{B}$$

and $$\underline{F}_{rippling} = \frac{V_y \eta_o'}{\mu_o \omega \eta_o} \nabla \times \underline{B} \times \underline{B} \qquad 2.12)$$

The driving power for the mode is

$$P \sim \underline{V} \cdot \underline{F}_{\text{rippling}} = \frac{V_y^2 \eta_o'}{\mu_o \omega \eta_o} B' B$$

or

$$P_{\text{rippling}} \sim \frac{V_y^2 \eta_o'}{\mu_o \omega \eta_o} (B')^2 (\epsilon a) \qquad 2.13)$$

This power must be of the same order as the power given in equation 2.5) in order to generate an instability at all. Therefore

$$\frac{V_y^2 \eta_o'}{\mu_o \omega \eta_o} (B')^2 (\epsilon a) = \frac{V_y^2 (B')^2 (\epsilon a)^2}{\eta_o}$$

and

$$\epsilon a \sim \frac{\eta_o'}{\mu_o \omega} \qquad 2.14)$$

Equating equations 2.8) and 2.14) we get an expression for ω, which is the growth rate of the instability.

$$\omega = \left(\frac{\eta_o'}{\mu_o}\right)^{4/5} \left[\frac{k^2 (B')^2}{4\pi^2 \eta_o \rho}\right]^{1/5} \qquad 2.15)$$

The derivations of F.K.R. for resistive instabilities employ two characteristic times to normalize the equations. They are:

τ_R = resistive diffusion time = $\dfrac{\mu_o a^2}{\eta_o}$

τ_H = magnetohydrodynamic transit time = $a\left(\dfrac{\mu_o \rho}{B^2}\right)^{1/2}$

Equation 2.15) can be rewritten in terms os these characteristic times as follows

$$\frac{\mu_o a^2}{\eta_o} \omega = \frac{\mu_o a^2}{\eta_o} \left(\frac{\eta_o'}{\mu_o}\right)^{4/5} \left[\frac{\mu_o (ka)^2 (B'/B)^2}{4\pi^2 \eta_o a^2 \mu_o \zeta / B^2}\right]^{1/5} \qquad 2.16)$$

combining terms

$$\left\{\frac{\mu_o a^2}{\eta_o}\right\} \omega = \left\{\frac{\mu_o a^2}{\eta_o}\right\}^{2/5} \left\{\frac{1}{a(\mu_o \rho / B^2)^{1/2}}\right\}^{2/5} \left(\frac{\eta_o'}{\eta}\right)^{4/5} \left(\frac{B'}{B}\right)^{2/5} \left(\frac{a^6}{4\pi^2}\right)^{1/5} x\,(ka)^{2/5}$$

$$\text{or } \tau_R\, \omega \sim (ka)^{2/5} \left(\frac{\tau_R}{\tau_H}\right)^{2/5}$$

where the remainder of the normalized quantities is assumed to be in the order of unity. This result is in agreement with the detailed calculations of F. K. R. For convenience we finally write the growth rate, normalized to τ_R, in the following form.

$$p \sim \alpha^{2/5} S^{2/5} \qquad (2.17)$$

where

$$p = \tau_R \omega$$

$$\alpha = ka$$

$$S = \frac{\tau_R}{\tau_H}$$

The "tearing" mode differs from the rippling mode principally because the driving force for tearing is not concentrated in a region ea about B = 0, but depends on the magnetic field structure outside the region. The mechanism for tearing can be understood from an examination of Figure II-3 and the discussion that follows. If an element of fluid is pushed downwards, the magnetic field is perturbed as shown resulting in a time rate of change for the first order magnetic field. Taking the y component of the following equation,

$$\nabla \times \underline{E} = -\frac{\partial \underline{B}}{\partial t}$$

we have $-jk\, E_z\, \underline{y}_o = \omega\, B_y\, \underline{y}_o$.

Thus a first order electric field is generated that has the following form

$$\underline{E} = -\frac{\omega B_y}{jk}\, \underline{z}_o \qquad (2.18)$$

The interaction of this electric field with the main mangetic flux density produces a drift velocity downwards in the direction of the initial perturbation. This situation is unstable, so a tearing mode develops.

$$\underline{V} = \frac{\underline{E} \times \underline{B}_c}{B_o^2} = - \frac{\omega B_y}{jk B_o} \underline{y}_o$$

The electric field given by equation 2.18) is complemented by a first order current density, J_1. Now Ohm's law has the following character.

$$\eta_o \underline{J}_1 = \underline{E} + \underline{V} \times \underline{B} = - \frac{\omega B_y}{jk} \underline{z}_o + \underline{V} \times \underline{B} \qquad 2.19)$$

For the instability to develop the first term on the right must dominate the second term.

$$\eta_o J_1 \sim \frac{\omega B_y}{jk} \qquad 2.20)$$

The value J_1 can be related to the magnetic field by

$$\nabla \times \underline{B} = \mu_o \underline{J}_1$$

and $$\nabla \cdot \underline{B} = 0$$

we find that $J_1 \sim \frac{B''_y}{j\mu_o k}$ and if B''_y is approximated by the following

$$B''_y \sim \frac{B'_y}{\epsilon a} \sim \frac{B_y}{k(\epsilon a)} \qquad 2.21)$$

Then we find from substitution in equation 2.20) that

$$\frac{\eta_o B_y}{j\mu_o k^2 (\epsilon a)} \sim \frac{\omega B_y}{jk}$$

and solving for ϵa we have

$$\epsilon a \sim \frac{\eta_o}{\mu_o k \omega} \qquad 2.22)$$

Equating equations 2.8) and 2.22) an expression for growth rate of the tearing mode can be written.

$$\gamma = \left\{\frac{\eta_o}{\mu_o k}\right\}^{4/5} \left\{\frac{k^2 (B')^2}{\rho \eta_o}\right\}^{1/5}$$

Normalizing via the characteristic times as done before, the above equation becomes,

$$\left\{\frac{\mu_o a^2}{\eta_o}\right\} \gamma = \left\{\frac{\mu_o a^2}{\eta_o}\right\}^{2/5} \left\{\frac{1}{a(\mu_o \rho / B^2)}\right\}^{2/5} \{ka\}^{-2/5} \left\{\frac{a B'}{B}\right\}^{2/5}$$

so $$p \sim \alpha^{-2/5} S^{2/5} \qquad 2.23)$$

for the tearing mode where p, α, and S are given by the list under equation 2.17).

The second part of this chapter will be concerned with the development of theoretical growth rate for a Rayleigh-Taylor instability along a plasma-vacuum interface. The method of analysis follows that of Rosenbluth and Longmire.[9]

We shall assume an infinite plasma carrying current with a magnetic field supporting the plasma against gravity. (Note that in our case the acceleration of the plasma under the action of the magnetic pressure generates an equivalent gravitational force.) It will be shown that if the interface is perturbed slightly, an instability occurs. Figure II-4 shows a sketch of the situation.

The gravity produces a drift velocity of the following form

$$\underline{V}_F = \frac{m\underline{G} \times \underline{B}}{q B^2} \qquad 2.24$$

so that the ions and electrons drift in opposite directions. When the interface has a wavelike perturbation this drift results in charge separation. This separation produces an electric field as shown in the figure. This electric field produces a new drift velocity.

$$\underline{V}_{\epsilon} = \frac{\underline{E} \times \underline{B}}{B^2} \tag{2.25}$$

This velocity, $\underline{V}_{\epsilon}$, is in the direction that tends to make the perturbation grow. In order to evaluate the growth rate we assume that the perutrbation is of the form

$$\Delta y = a \sin kx \tag{2.26}$$

so that the change in charge density, $\delta\sigma$, is

$$\delta\sigma = nq\,\delta\Delta y = nq\,\frac{\partial \Delta y}{\partial x}\,\delta x$$

or

$$\delta\sigma = nqak\cos kx\,\delta x \tag{2.27}$$

If $\underline{V}_F = \frac{\delta x}{\delta t}$, then we have for δx the following.

$$\delta x = V_F\,\delta t = \frac{m_i G}{qB}\,\delta t \tag{2.28}$$

Here the electron drift has been neglected since the ion mass is much greater than the electron mass.

The time rate of change for the surface charge density $\sigma(y)$ is

$$\frac{\delta\sigma}{\delta t} = nqak\,\frac{m_i G}{qB}\cos kx$$

or

$$\frac{\delta\sigma}{\delta t} = \frac{\rho_i a k G}{B}\cos kx \tag{2.29}$$

where $\rho_i = n m_i$

For small perturbations and a very thin surface charge layer, σ may be expressed as

$$\sigma = \sigma_o \cos kx \tag{2.30}$$

The electric field produces by this charge density in the static limit can be found by solving

$$\nabla \cdot \underline{E} = 0$$
$$\nabla \times \underline{E} = -\frac{\partial \underline{B}}{\partial t} = 0$$

The electric fields in the plasma are thus

$$\left.\begin{aligned} E_x &= -\frac{\sigma_o}{\epsilon} \sin kx\, e^{-ky} \\ E_y &= \frac{\sigma_o}{\epsilon} \cos kx\, e^{-ky} \end{aligned}\right\} \tag{2.31}$$

where $\epsilon = (\epsilon_o + \frac{\rho_i}{B^2})$

The drift velocities associated with the electric fields given above are

$$V_x = \frac{E_y}{B} = \frac{\sigma_o}{\epsilon B} \cos kx\, e^{-ky}$$

$$V_y = \frac{E_x}{B} = \frac{\sigma_o}{\epsilon B} \sin kx\, e^{-ky}$$

The V_y velocity gives rise to instability and at the boundary y = 0 causes the perturbation Δy to grow as follows

$$V_y = \frac{d\Delta y}{dt} = \frac{\sigma_o}{\epsilon B} \sin kx$$

But $$\frac{d\Delta y}{dt} = \frac{d}{dt}(a \sin kx) = \frac{da}{dt} \sin kx$$

$$\therefore \frac{da}{dt} = \frac{\sigma_o}{\epsilon B} \tag{2.32}$$

Differentiating equation 2.32) again we get

$$\frac{d^2a}{dt^2} = \frac{1}{\epsilon B} \frac{d\sigma_o}{dt}$$

but $$\frac{d\sigma_o}{dt} = \frac{\xi_i a kG}{B}$$ from equations 2.29) and 2.30)

so that $$\frac{d^2a}{dt^2} = \left(\frac{\xi_i kG}{\epsilon B^2}\right) a \qquad 2.33)$$

From equation 2.33) we see that for the case of an instability, a has the following form.

$$a = \exp\left(\frac{\xi}{\epsilon B^2} kG\right)^{1/2} t \qquad 2.34)$$

now $$\frac{\xi}{\epsilon B^2} = \frac{1}{1 + \frac{\epsilon_o B^2}{\xi}} \text{ ; and } \frac{\epsilon_o B^2}{\xi} = \frac{HB}{\xi C^2} \ll 1$$

So equation 2.34) becomes

$$a = \exp \sqrt{kGt} \qquad 2.35)$$

where G does not necessarily have to be gravitational acceleration but can be a result of magnetic pressure or curvature of a current carrying plasma .

This theory neglects any damping mechanisms. One form of damping can be a result of viscous friction resulting from motion of the plasma undergoing a Rayleigh-Taylor instability. The damping due to finite viscosity can be calculated simply from the following equation.

$$\xi \frac{d\underline{V}}{dt} = \frac{1}{3} \xi \nu \cdot (\nabla \cdot \underline{V}) + \xi \nu^2 \underline{V} \qquad 2.36)$$

where ν is the viscosity .

The plasma configuration is the same as shown in Figure II-4. We assume that near the interface the velocity has the form

$$\underline{V} = V_o^{-mt} e^{jky} \underline{x_o} .$$

Substituting in equation 2.36) we have

$$m\underline{V} = \nu k^2 \underline{V} \quad . \tag{2.37}$$

Therefore the viscous damping constant is νk^2.

Therefore as the wavelength of the instability decreases, damping due to finite viscosity increases so that there is a minimum wavelength at which the instability can grow. The approximate wavenumber, k, corresponding to this situation can be determined from the following equations,

$$\nu k^2 = (kG)^{1/2} \tag{2.38}$$

Solving for k, we have:

$$k = G^{1/3} \nu^{-2/3} \tag{2.39}$$

and the minimum wavelength is

$$\lambda \min = \frac{2\pi}{k} = 2\pi G^{-1/3} \nu^{2/3} \tag{2.40}$$

We see that although G is responsible for the Rayleigh-Taylor instability, its influence on λmin is much smaller than that of ν, and therefore λmin is essentially a measure of the viscosity.

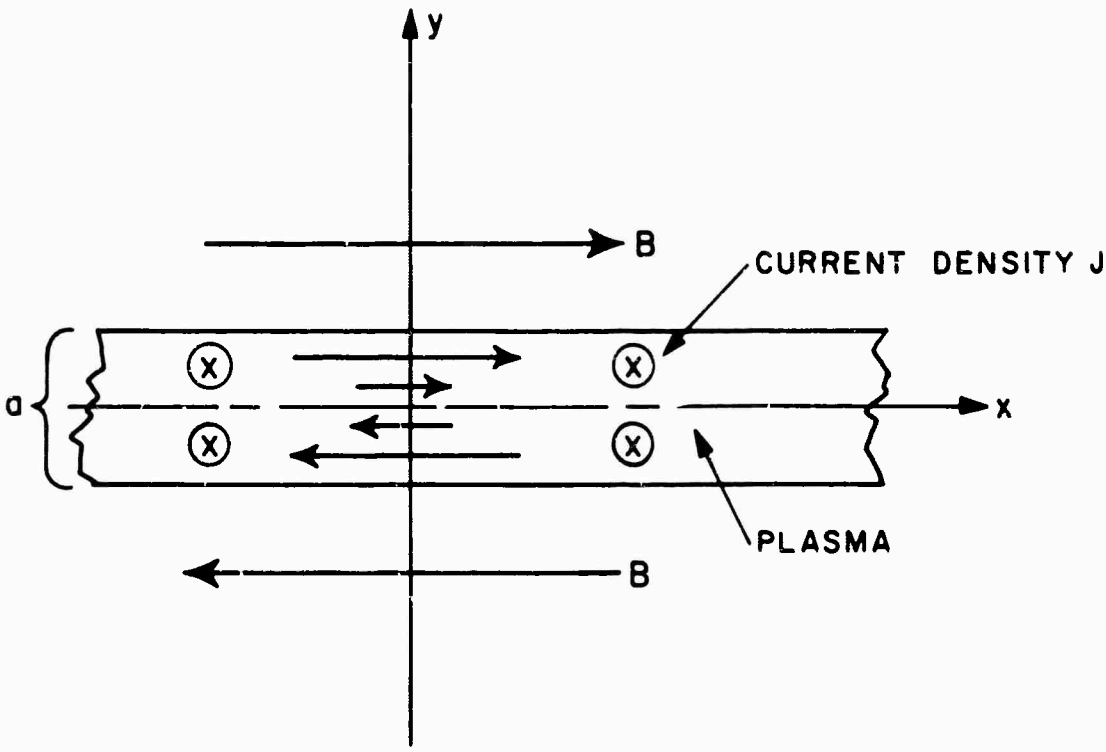

Sheet Pinch

Figure II-1

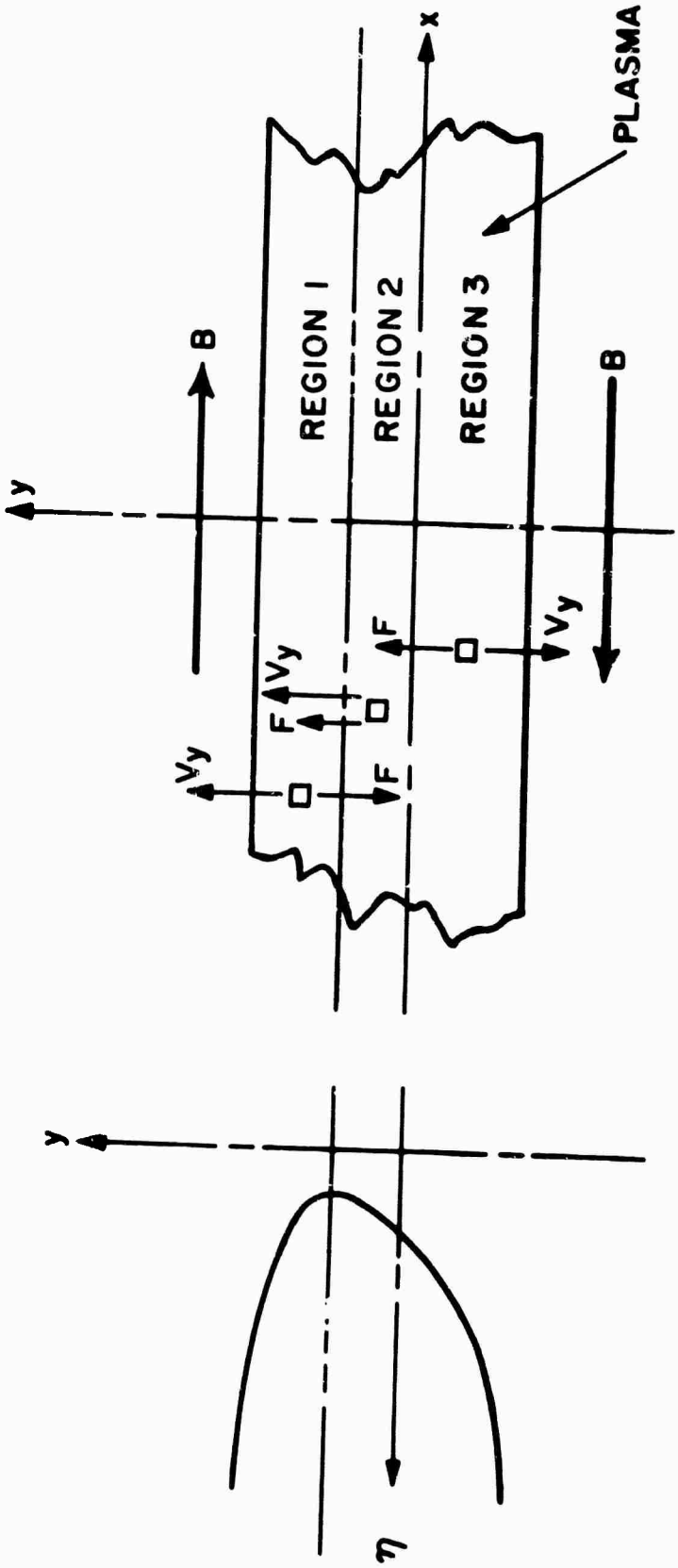

Rippling Mode Diagram

Figure II-2

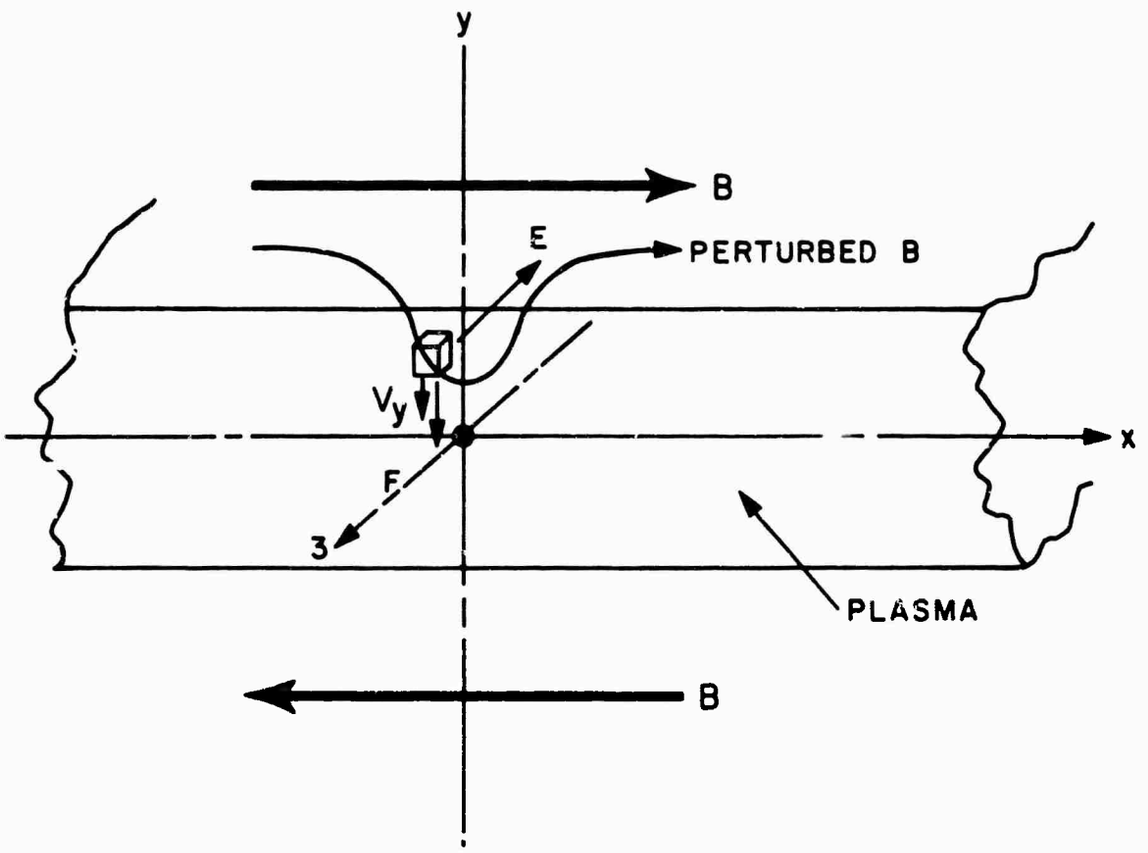

Tearing Mode Diagram

Figure II-3

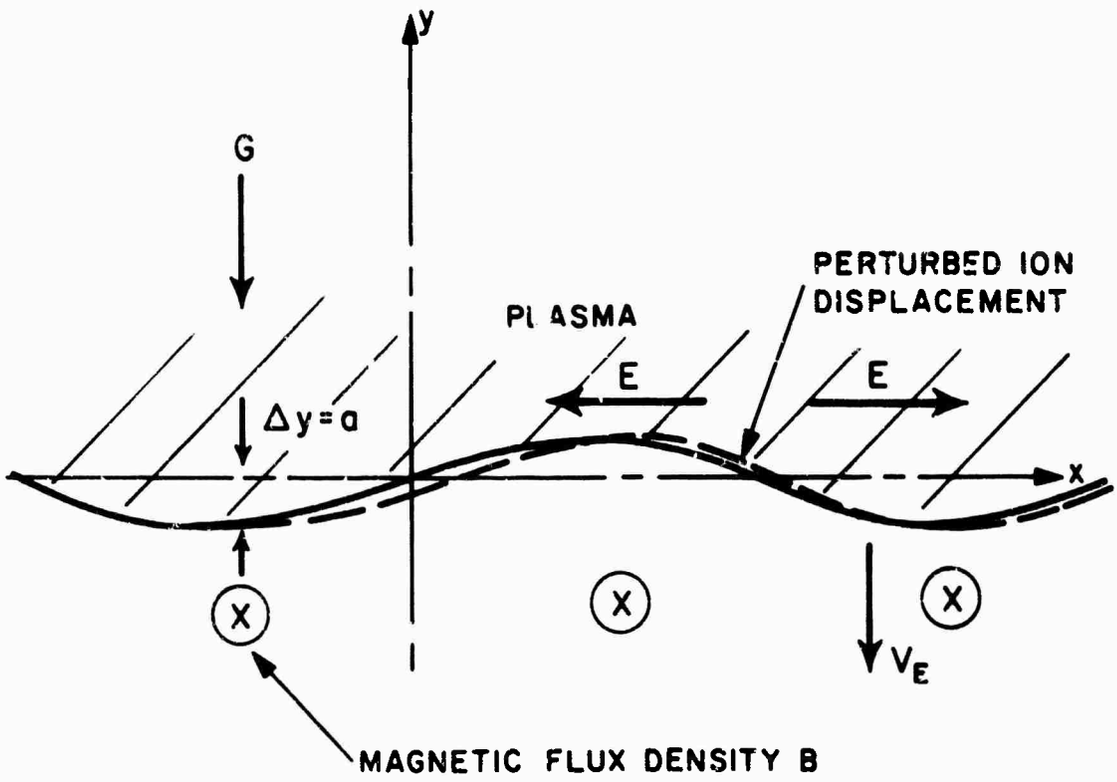

Development of Rayleigh-Taylor
Instability

Figure 4-4

CHAPTER III

ARRANGEMENT OF EXPERIMENTAL TOROID

The experiments were performed on an electrodeless toroidal plasma of a type conceived by K. T. Lian[10] for the purpose of high power switching. The container for the plasma was a pyrex toroid having a rectangular cross section. During the course of the experiment both narrow and wide bottles were used. Shown in Figure III-1 is a sketch of the wide toroidal bottle. The narrow bottle also had a small glass pipe inserted radially and equidistant from the side walls of the toroid so that magnetic field measurements in the core of the discharge region could be obtained.

The toroidal bottle was connected to a high vacuum system and baked out for twenty four hours at 400^{o} centigrade. Vacuum pressures of about 10^{-8} mm. of Hg were achieved routinely between experimental runs. Hydrogen was used for the experiment mainly and filling pressures varied between 50 microns and 500 microns of Hg depending on whether Rayleigh-Taylor or resistive instabilities were being studied.

A plasma discharge was induced in the hydrogen by means of an iron cored transformer. A hypersil core threaded the bore of the toroidal bottle and a primary winding was placed between the core and the inner surface of the glass envelope. The primary winding was energized by a high voltage modulator. When the hydrogen in the bottle becomes ionized, it becomes a gaseous conductor that assumes the role of a secondary winding and load on a transformer.

Figure III-2 shows the various primary winding configurations used during the course of the experiment. The function of these different winding arrangements is to introduce a spatial periodicity in the electromagnetic field. This causes an initial perturbation in the plasma that determines the wavelength of the resistive instability that will develop. Copper strips are

placed over the windings along the major axis so that perturbations in the applied electric field are minimized, while the major perturbation is due to the magnetic field developed by the various windings. The uniform winding gives rise to a plasma structure with two filaments; in general, if N is the number of groups into which the primary winding is divided, the discharge will break into N + 1 separate filaments. The windings are fabricated so that the ampere-turns of each segment are cumulative while at the same time generating a spatial periodicity that causes the plasma to form the appropriate number of filaments.

The high voltage pulse modulator is capable of delivering up to 20 megawatts power to the toroidal plasma configuration. Figure III-3 shows a simplified schematic of the modulator. Initially the R-L-C combination is impressed across the D.C. voltage power supply. The L-C elements form a tank circuit and therefore the voltage and current are of an oscillatory nature. Because of the diode shown in the circuit, only the first half cycle of oscillation is allowed and the voltage drop across the capacitor at the end of charging is double that of the D.C. voltage supply. The resistor, R_1, serves to limit the charging current while R_2 is adjusted so that the pulse current to the toroid is essentially critically damped.

The current pulse is applied to the toroid by triggering the hydrogen thyratron. A low energy pulse with a 60 Hertz repetition rate is applied to a driver unit that amplifies the trigger and then drives the grid of the hydrogen thyratron positive, thus firing it into a conducting state. The current pulse has a duration of approximately six microseconds and its peak amplitude was adjusted between 4 kiloamperes and 7 kiloamperes during the course of the experiment.

Preionization of the toroidal plasma was employed to insure that the plasma was initially uniform in the axial direction before the large current pulse from the modulator was applied. Energy for preionization is coupled into the plasma capacitvely via the two copper sheets encircling the outer circumference of the toroid as shown in Figure III-1. An overall schematic

of the experiment is given in Figure III-4. In this figure is shown the R. F. transmitter, which is tuned to 7 MHz, that supplies power to a tank circuit. The inductance of the tank circuit is about 120 μh wound on a six inch coil form and this is connected in parallel to the copper sheets that form the capacitor mentioned above.

Also shown in the figure is the modulator that supplies the current pulse to the toroid, timing circuitry, and various instrumentation. Included in instrumentation are an S. T. L. image convertor camera for taking ultra high speed photographs, monochromater and spectrograph for making optical measurements of plasma electron temperature and density, and probes for measuring magnetic field, plasma current, and modulating voltage. Electrical outputs from the instrumentation are monitored on a Tektronix 555 dual-beam oscilloscope. Electrical timing of instrumentation, oscilloscope and high voltage pulse modulator are accomplished by a 60 Hz clock driving an S. T. L. pulse generator. This generator develops fixed and time delayed pulses that have rise times of 2 nanoseconds. The time delayed pulses can be varied between 0 - 100 microsecond delay time in 10 nanosecond steps with an accuracy of one nanosecond. This results in an ability to record data with great precision and makes correlation of various data from the instrumentation easier.

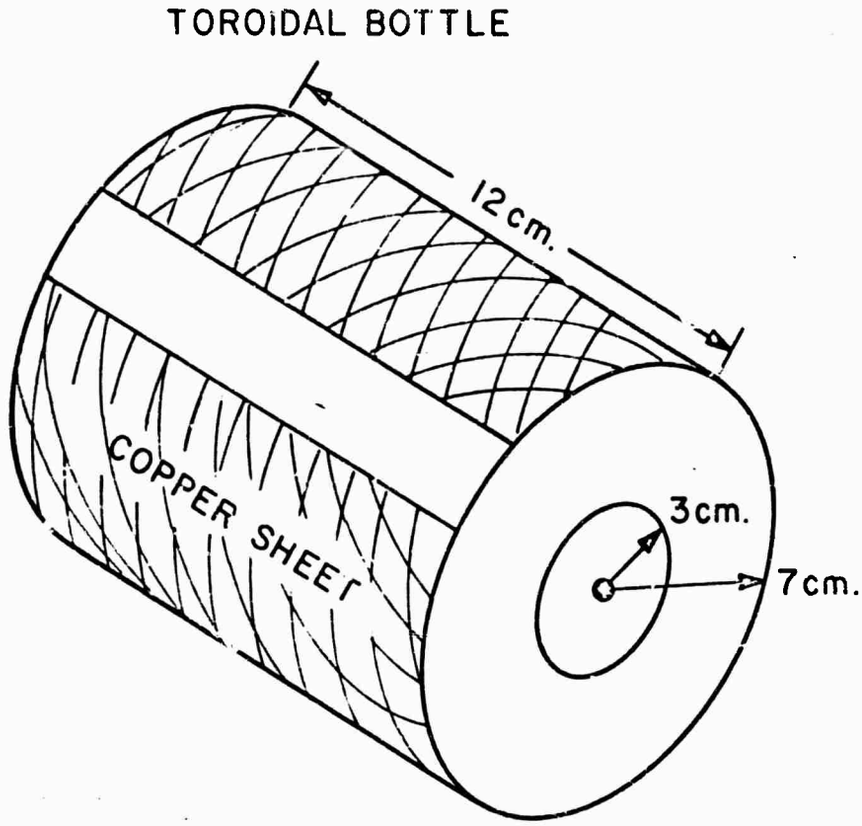

Schematic of Toroidal Bottle

Figure III-1

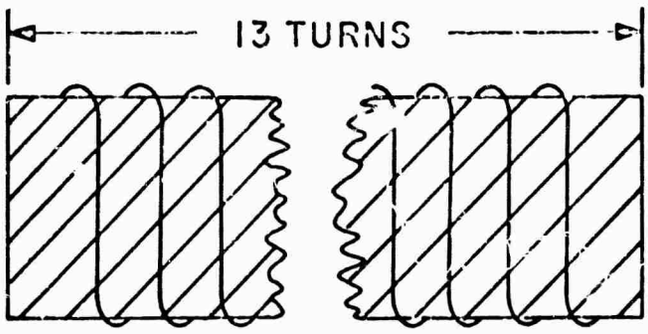

WINDING FOR TWO PLASMA RINGS

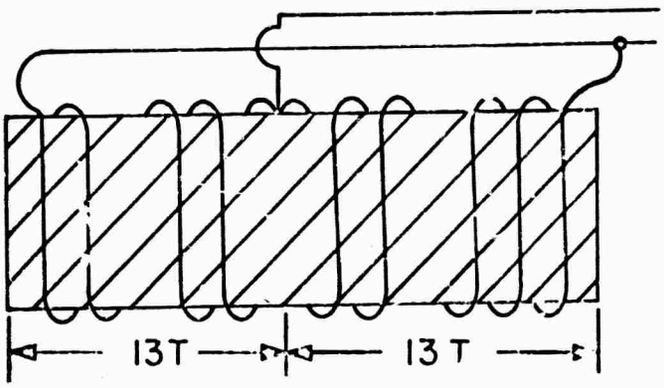

WINDING FOR THREE PLASMA RINGS

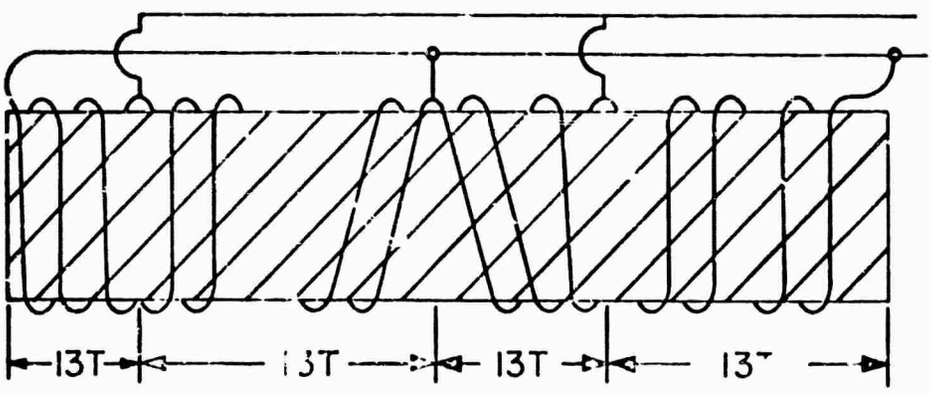

WINDING FOR FIVE PLASMA RINGS

Primary Winding Configurations

Figure III-2

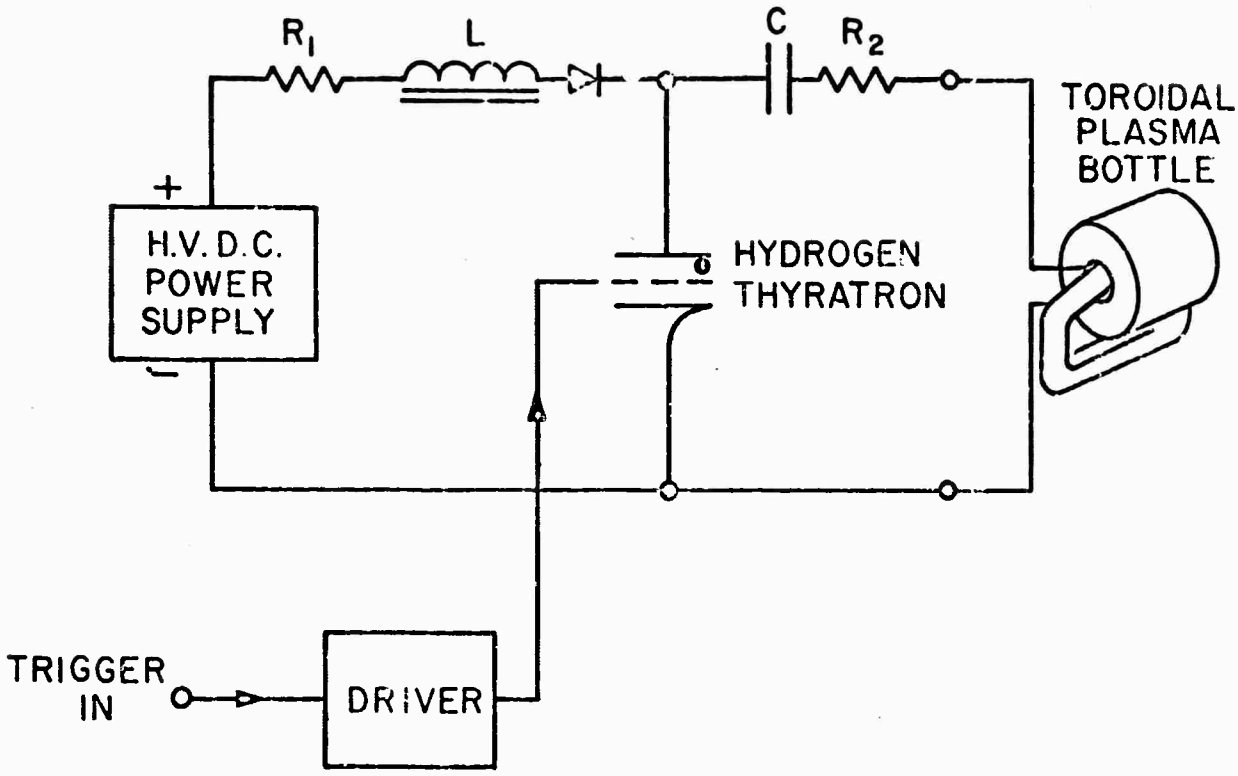

High Voltage Pulse Modulator

Figure III-3

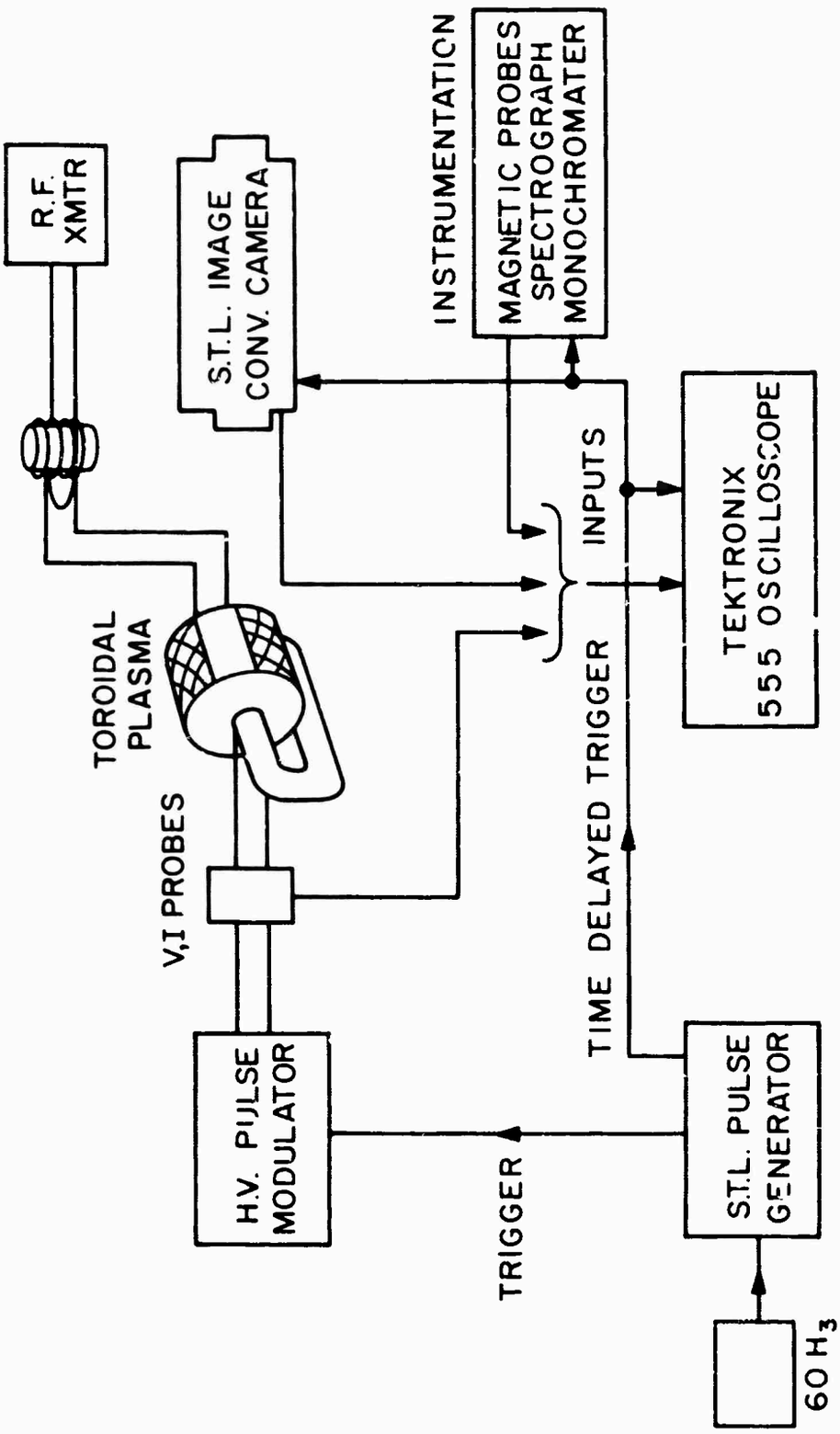

Schematic of Experimental Set-up

Figure III-4

BLANK PAGE

CHAPTER IV

INSTRUMENTATION

Several methods are employed to determine the properties that characterize the toroidal plasma. Voltage and current measurements, magnetic probes, fast photography with an image converter camera, and spectroscopic determination of density and temperature are included in the instrumentation methods.

A. Voltage Measurements

Voltage measurements are obtained with a Tektronix P6015 high voltage probe. The probe is attached to a single turn of wire encircling the magnetic core of the toroidal plasma bottle. The voltage measured, then, is equivalent to the voltage drop for a complete circular path in the plasma ring.

The voltage signal is helpful for determining rapid inductive changes in the system. For example, at breakdown of the gas, the initially high voltage drops to a low value. Also changes in radial plasma motion can be detected by the behaviour of the voltage signal.

B. Current Measurements

The current fed to the primary winding from the modulator is monitored by a current transformer. The current transformer consists of a permalloy core about 1 1/2" in diameter and the primary of this transformer is a single wire passing through the center of the core. This wire carries the modulator current. The secondary winding consists of many turns coupled to a resistive load of approximately a few ohms. The voltage developed across this resistor is proportional to the modulator current if the leakage flux of the transformer is neglected.

Actually it is the measurement of plasma current that is of prime interest. Although this current can't be measured directly, the difference between primary current and plasma current can be. A core for a difference current transformer is made of permalloy tape. This tape is threaded so that it links both the primary winding and the plasma in the toroidal bottle.

The ampere-turns associated with the primary winding and the plasma make up the primary flux for the difference current transformer. Again many turns encircling the tape form a secondary winding and this is terminated in a resistor of only a few ohms. Ideally the voltage developed across this resistor should be zero; for this indicates perfect coupling between the plasma and the primary winding of the toroidal bottle. However, if the voltage is not zero the plasma current can be computed since the difference current transformer can be calibrated against the modulator current in the absence of a plasma, and then the plasma current is computed as the following: $I_{plasma} = N_{\substack{primary \\ turns}} I_{primary} - I_{diff.\ cur.\ xfmr.}$

C. Magnetic Probes

Both stationary and movable probes were constructed. The stationary probes were mounted on two lucite disks. Each disk was positioned on a side wall of the toroidal bottle. Imbedded on each disk are ten concentric loops as shown in Figure IV-1. Their main purpose is to sample the axial component of the magnetic flux density, Bz, and thus determine its time resolved variation of the radius. From this variation one can ascertain the radial motion of the plasma current sheet. The symmetry and stability of this motion is checked by four small probes mounted on each lucite disk 90° apart. These probes sample Bz also. Further examination of Figure IV-1 reveals another set of small fixed probes that are orthogonal to the set of probes mentioned above. This last group of four probes are also 90° apart and measure the symmetry of the radial component of magnetic flux density, Br.

The small movable probe is shown in Figure IV-2. Two such probes were made, one to measure Br, and the second to measure Bz (Bθ can be measured by merely rotating this last probe 90°). The probes consist of a coil of 50 turns of #50 enameled copper wire wound on a $\frac{1}{16}$ inch bakelite rod. These probes can be moved around and inside the glass envelope of the plasma toroidal bottle allowing the magnetic field to be mapped. Application of Maxwell's equations yields the current distribution.

The leads from all probes were twisted to eliminate stray pickup In addition the small movable probes incorporated both magnetic and electric shielding on the leads. Signals from the probes were electronically integrated with a RC circuit to obtain Br, Bz, and B_θ. The time constant of the RC circuit was 80 usec., which is approximately ten times the modulator pulse length.

D. Fast Photography with a S. T. L. Image Converter Camera

An independent sampling of the dynamics of the plasma discharge is obtained with the help of a S. T. L. image converter camera. This camera is fitted with two tubes, one with sensitivity peaking in the red and the other peaking in the blue portion of the optical spectrum. Both tubes have a light flux gain greater than 50 X each. It is thus possible to obtain a photograph of the overall light emission of the plasma, and by using appropriate interference filters, to follow the space and temporal development of specific spectral lines.

The camera can be operated in two modes: framing and streaking. In the framing mode a sequence of nine pictures of the plasma discharge can be taken with an exposure time of 50 nanoseconds typically and with a time interval between pictures of 500 nanoseconds. When operating in the streaking mode, the camera is used at a lusec/ 10mm. writing speed. However the camera can scan as slow as 1 usec/5mm. or as fast as 1 nanosec-/1mm. The camera is triggered by a variable time delay pulse from a S. T. L. trigger delay generator. The same generator triggers the thyratron in the modulator with a fixed pulse. Satisfactory time resolution in the photograph sequence is assured, since the jitter in the time delay doesn't exceed 2 nanoseconds.

Figures IV-3 and IV-4 show the camera set up to take a sequence of framing pictures along the z-axis and perpendicular to the z-axis respectively. When taking streak photographs it is necessary to select light emission whose rays are almost parallel, in other words, a small solid angle.

Streak photographs taken of light along the radial axis require no auxillary equipment since the camera must be far from the plasma bottle in order to accept all radial light rays emitted along the z axis of the plasma discharge. See Figure IV-5 . However streak photographs of z axis light emission with a radial distribution have a smaller field of view than in the previous case. This requires the camera to be closer to the event which causes the solid angle to increase. In this case a mechanical collimator with a $1/2^{o}$ acceptance angle is mounted directly in front of the camera. This set-up is illustrated in Figure IV-6 .

E. Quantitative Streak Photography

Streak photographs are particulary suited for quantitative measurements of variation in light intensity emitted by the plasma because this photograph is a continuous temporial record of either radial or axial distribution of essentially parallel light rays. A major difficulty is the fact that the information is stored logarithmically and a suitable calibration of the film must be made.

The method employed here is to reserve a small portion of the film for making a calibration record. The plasma bottle is completely masked except for a small pinhole. A streak photograph of light emission from pinhole is recorded in the reserved spot. Next a photodiode, which has a linear response to light intensity, is exposed to the pinhole . The photodiode signal is fed to an oscilloscope and photographed.

A Wihtol microdensitometer and Brown Electronik recorder shown in Figure IV-7 are used to analyse the film. First, the calibration record on the film is scanned and plotted against the photodiode signal at identical instants of time. This results in a calibration curve for the film. Then the streak pictures of the plasma are scanned, each data point being unfolded by the calibration curve to its proper value of light intensity.

This technique was used extensively for the determination of growth rates for resistive instabilities .

F. Spectrograph

A set-up employing a Baush and Lomb 1.5 meter spectrograph to survey the spectrum emitted by the plasma discharge is shown in Figure IV-8. Royal X pan film was used. An exposure time of approximately 15 minutes and development in Acufine was required to produce acceptable results. The film was then microdensitometered in order to facilitate interpretation of the spectrum for impurities. In addition the Balmer series spectral lines or Hydrogen were examined and the number density calculated using the method of Inglis and Teller. In this technique the micro fields of both ions and electrons cause broadening of the higher energy levels in the series. When the last distinguishable line has a width half the "distance" to the preceding line the relation between electron density and the last line is the following

$$3.7\,\frac{{}^{3}/_{2}\, a_o n_m^2 N_e^{2/3} e^2}{Z} = \frac{{}^{1}/_{2}\, e^2 Z^2}{a_o n_m^3} \qquad 4.1)$$

or

$$N_e^{2/3} = \frac{Z^3}{11.1 n_m^5 a_o^2} \qquad 4.2)$$

where a_o - Bohr radius

Z - atomic number

n_m - total quantum number of last distinguishable line

e - electron charge

N_e - electron density

The electron density can thus be ascertained by identifying the last distinguishable line.

G. Monochromater

A 500mm. Baush and Lomb grating monochromater equipped with a photomultiplier tube was used to examine the light emission in detail. The monochromater was attached to a motor drive so that scans of 2Å / second or 20Å/ second could be made. In addition, Hilger-Watts slits (repeatability of less than 2 microns) were used to increase the systems efficiency. Following Griem,[11] temperature measurements were made by comparing the ratio of the H_δ line in the Balmer Series of Hydrogen to the neighboring 100Å continuum. This measurement was performed at a 2Å/second grating speed, and since the plasma discharge is pulsed, a Tektronix 151 plug-in was used to sample the photomultiplier tube output at a particular instant of time. The output of the 151 plug-in unit drove a strip chart recorder (see Figure IV-9). Thus, the plot on the chart was a time resolved spectrogram. This set-up was prepared by R. Chimenti.

A planimeter was used to measure the area under the H_δ line and 100Å continuum so that the ratio could be calculated. The curve of H_δ/100Å continuum versus temperature, taken from Griem, is shown in Figure IV-10.

A technique for measuring electron number density via examination of Stark profiles described in a paper by Griem et. al.[12] appeared attractive. In this method, the Stark profile is not measured per se, instead the monochromater is set at the line core, and photomultiplier tube outputs are recorded for narrow and wide slits. The ratio of narrow to wide exit slit signals uniquely determines the number density and this measurement is practically independent of temperature. Griem worked with H_δ; however in my experiment H_β was selected as the optimum choice. The curve of density versus the ratio of signals with .1mm exit slit and 1mm exit slit is shown in Figure IV-11.

The agreement between the experimental line profiles and those due to the general theory of line broadening set forth by Griem, Kolb and Shen[13] is about 5% for H_β. Unfortunately the solutions for the theoretical line profiles can not be expressed in closed form, so numerical tables have been prepared by the authors which enable one to plot a particular line for various electron densities and temperatures.

The Holtsmark theory,[14] presented in 1919, yields a profile that gives good agreement in the wings, and moreover predicts the correct half width of the broadened line.

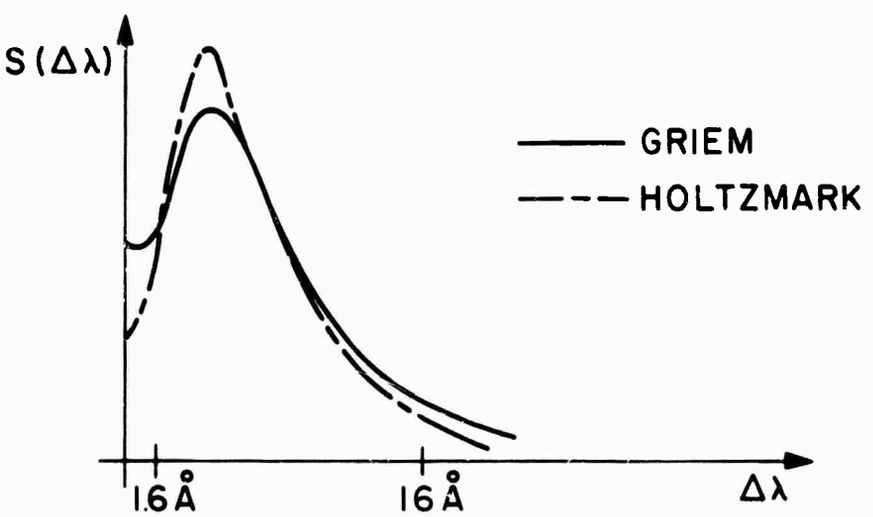

The sketch shown above illustrates the comparison between Holtsmark's theory and that due to Griem et. al.[13] Disagreement between the two curves is pronounced in the neighborhood of the line core. Here, doppler broadening plays a greater role. This phenomena is not taken into account by the Holtsmark theory.

The following is an explanation of why the ratio of light flux for 1.6Å and 16Å wavelength bands centered at the line core of the H_β line results in a unique determination of electron density. First it is asserted that the

effect of doppler broadening is confined mostly in the 1.6Å wavelength band, and for larger wavelength bands, eg. 16Å the Holtsmark theory is a fair approximation to the actual line profile, $S(\Delta\lambda)$. We next assume that the total line profile is prescribed by the Holtsmark function given below

$$H(\beta) = 3/2\ \beta^{-5/2} \exp\left[-(\beta)^{-3/2}\right] \qquad 4.3)$$

where $\beta = \dfrac{\Delta\lambda_k}{C_k E_o}$ and

$\Delta\lambda_k$ = shift in wavelength of k^{th} line due to Stark effect .

C_k = constant depending on initial and final quantum numbers involved in the transition for excitation of H_β .

E_o = "average" electric field associated with the Stark broadening effect .

The light intensity distribution for the Stark broadened line is related to the Holtsmark function by

$$I_k = \frac{I_k^o}{C_k} H(\beta) \qquad 4.4)$$

where I_k^o = intensity of unbroadened k^{th} line

I_k = intensity of Stark broadened k^{th} line.

Now equations 4.3) and 4.4) can be combined to yield

$$I_k = \frac{I_k^o}{C_k} 3/2 \left(\frac{\Delta\lambda_k}{C_k E_o}\right)^{-5/2} \exp\left[-\left(\frac{\Delta\lambda_k}{C_k E_o}\right)^{-3/2}\right] \qquad 4.5)$$

The average electric field, E_o, is really a function of the electron density. This can be demonstrated by first calculating the "average" separation between ions for a density of ions equal to N_i . This is done by solving the equation below.

$$\frac{4}{3}\pi R_o^3 N_i = 1 \qquad 4.6)$$

where R_o = average separation, N_i = ion density. Now the average electric field is

$$E_o = \frac{e}{4\pi \epsilon_o R_o^2} \qquad 4.7)$$

Substituting equation 4.6) into 4.7) we have

$$E_o = A N_i^{2/3}$$

where A = constant

For hydrogen we have electron density equal to ion density, therefore

$$E_o = A N_e^{2/3} \qquad 4.8)$$

where N_e = electron density.

Finally the substitution of equation 4.8) into 4.5) results in

$$I_k = \frac{I_k^o}{C_k} \frac{3}{2} \left(\frac{\Delta\lambda_k}{\hat{C}_k N_e^{2/3}}\right)^{-5/2} \exp\left[-\left(\frac{\Delta\lambda_k}{\hat{C}_k}\right)^{-3/2} N_e\right] \qquad 4.9)$$

where $\hat{C}_k = A C_k$

The total light flux of the Stark broadened spectral line, H_β, over a wavelength band $\Delta\lambda$ is the following:

$$A = \int_0^{\Delta\lambda} I_k (\Delta\lambda_k)\, d(\Delta\lambda_k)$$

$$A = \frac{I_k^o}{C_k} \exp\left[-\left(\frac{\Delta\lambda}{\hat{C}_k}\right)^{-3/2} N_e\right] \qquad 4.10)$$

If we now let $\Delta\lambda_1 = 1.6\mathring{A}$ wavelength band and $\Delta\lambda_2 = 16\mathring{A}$ wavelength band and form the ratio of light flux for the two bands we have :

$$\frac{A_1}{A_2} = \frac{\exp\left[-\left(\frac{\Delta\lambda_1}{\hat{C}_k}\right)^{-3/2} N_e\right]}{\exp\left[-\left(\frac{\Delta\lambda_2}{\hat{C}_k}\right)^{-3/2} N_e\right]} \qquad 4.11)$$

Simplifying, equation 4.11) becomes

$$R = \frac{A_1}{A_2} = \exp\left[-\hat{C}_k^{3/2} N_e \left(\Delta\lambda_1^{3/2} - \Delta\lambda_2^{3/2}\right)\right] \qquad 4.12)$$

Now the variation of the light flux ratio, R, with electron density is given by

$$\frac{dR}{dN_e} = -\hat{C}_k^{3/2}\left(\Delta\lambda_1^{-3/2} \quad \Delta\lambda_2^{-3/2}\right) R \qquad 4.13)$$

We know that $C_k > 0$

$$0 < R < 1$$

and $$\Delta\lambda_1 < \Delta\lambda_2$$

$$\therefore \lambda_1^{-3/2} - \Delta\lambda_2^{-3/2} > 0 .$$

The above implies that $\frac{dR}{dN_e} < 0$, or that R monotonically decreases as N_e increases. This, in fact, is the behavior of Figure IV-11 which shows N_e versus A_1/A_2 .

Electron density was also determined by inserting the observed half width of a line into an equation of the form

$$N_e = C\,\Delta\lambda^{3/2} \qquad 4.14)$$

where C is a quantum mechanical constant that is a weak function of electron density. Such an expression[15] has its roots from the equation given below, which relates the wavelength shift of a spectral line to an impressed electric field. This is the first order Stark effect.

$$\Delta\lambda \sim \lambda^2 (n n_F - n' n_F) E \qquad 4.15)$$

where n, n' = principal quantum numbers

and n_F, n'_F = electric field quantum numbers related to electric dipole moment of atom and perturbing electric field, E.

From before, equation 4.8), we have that

$$E = A N_e^{2/3}$$

where A is a constant.

Therefore, equation 4.15) becomes

$$\Delta\lambda \sim \lambda^2 (n n_F - n' n'_F) A N_e^{2/3}$$

or

$$N_e \sim \frac{1}{\lambda^2 (n n_F - n' n'_F) A} \Delta\lambda^{3/2} \qquad 4.16)$$

and letting

$$C = \frac{1}{\lambda^2 (n n_F - n' n'_F) A}$$

This last equation has the same form as equation 4.14). Values of C are given in the book "Plasma Spectroscopy" by Griem.

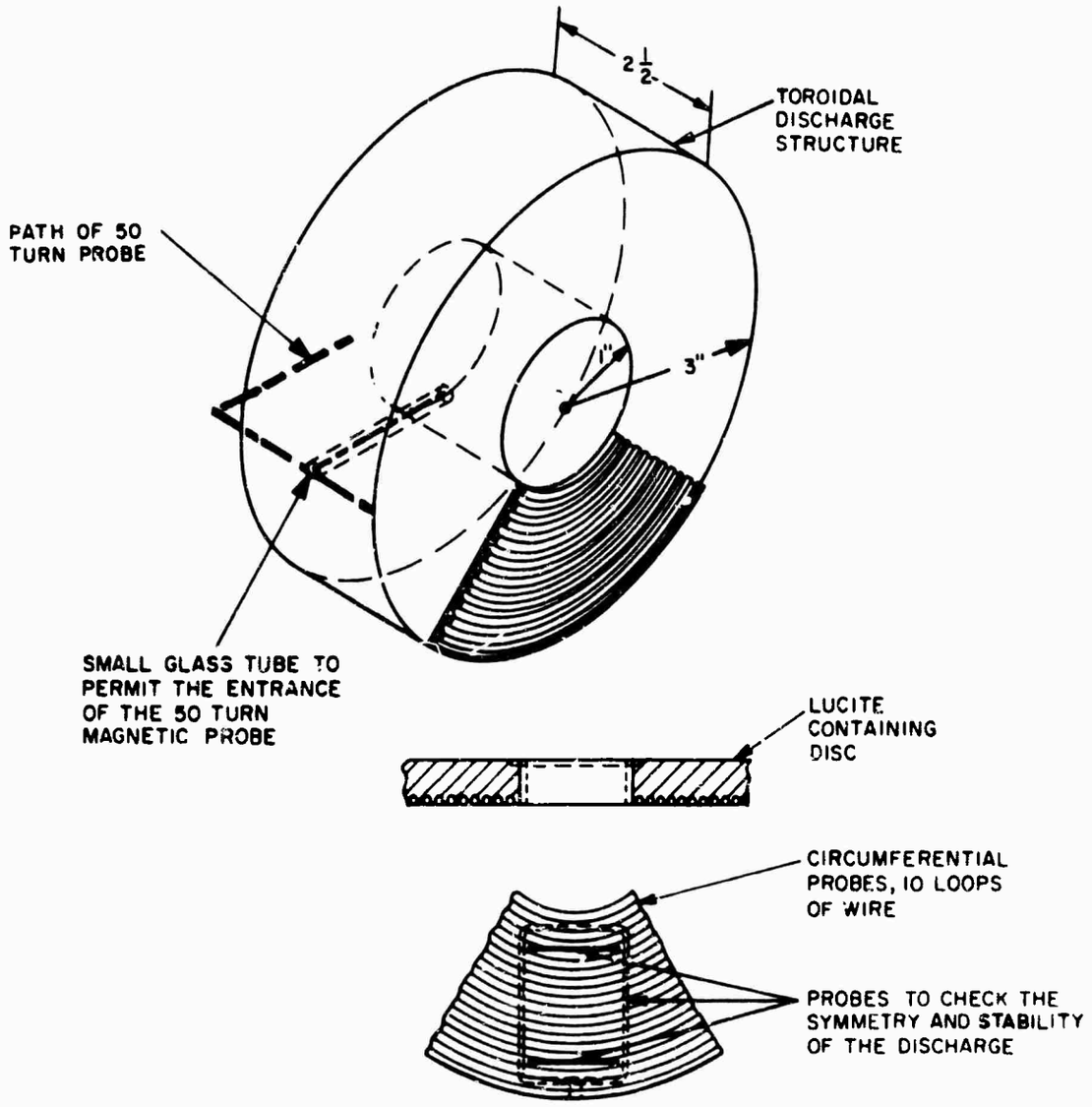

Stationary Magnetic Probes

Figure IV-1

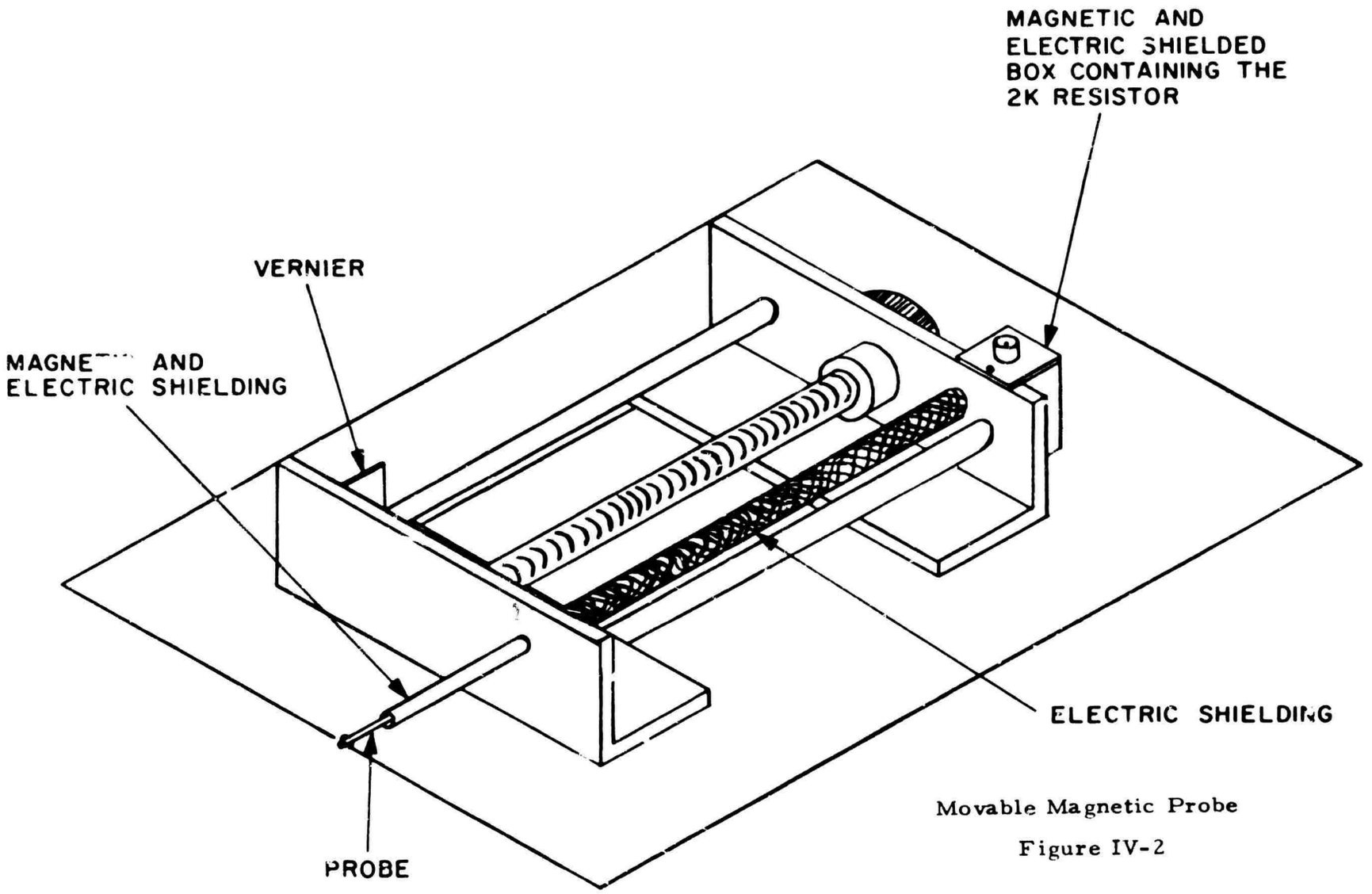

Movable Magnetic Probe

Figure IV-2

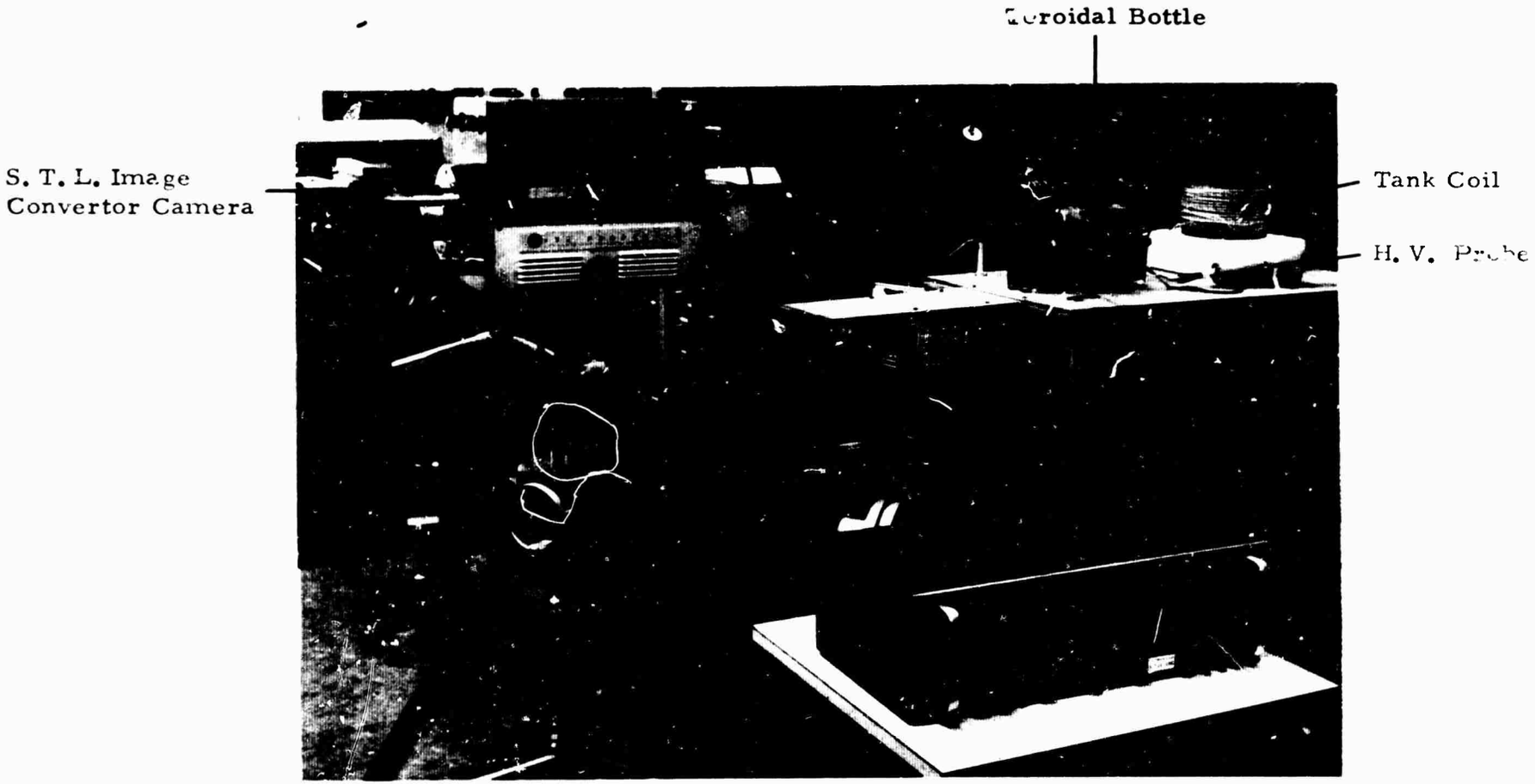

Framing Along Z axis

Figure IV-3

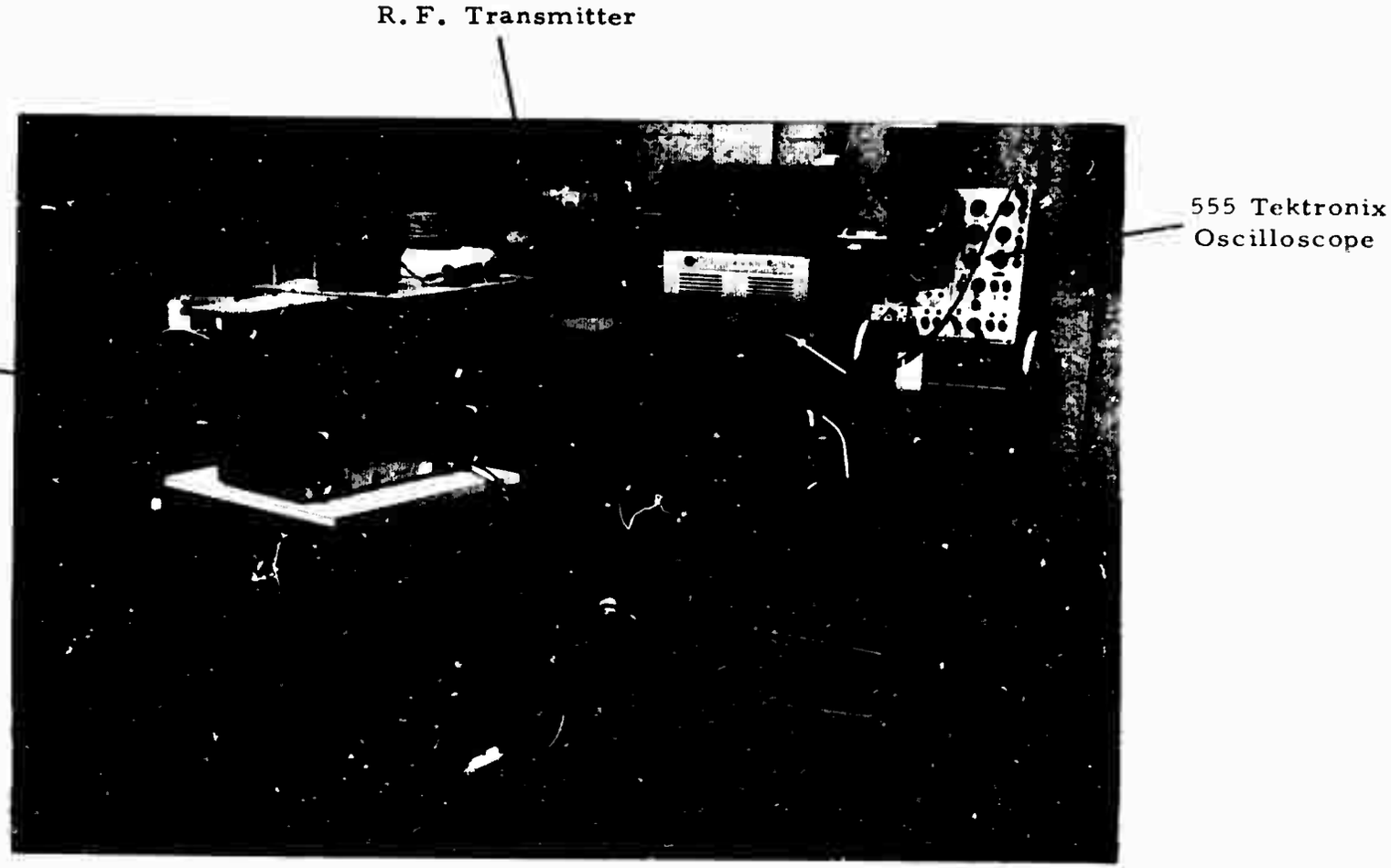

Framing Perpendicular to Z axis

Figure IV - 4

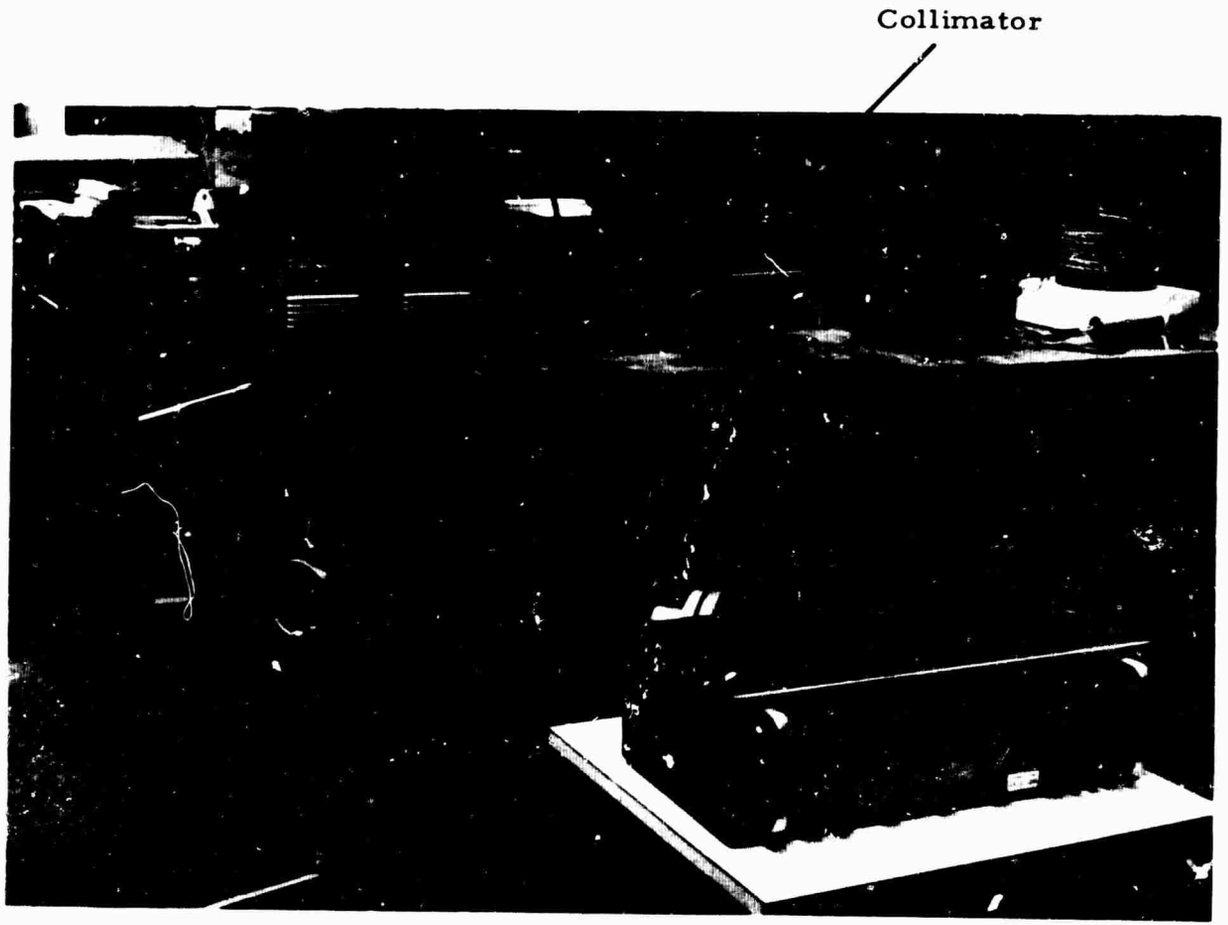

Streak Along Radial Axis

Figure IV - 5

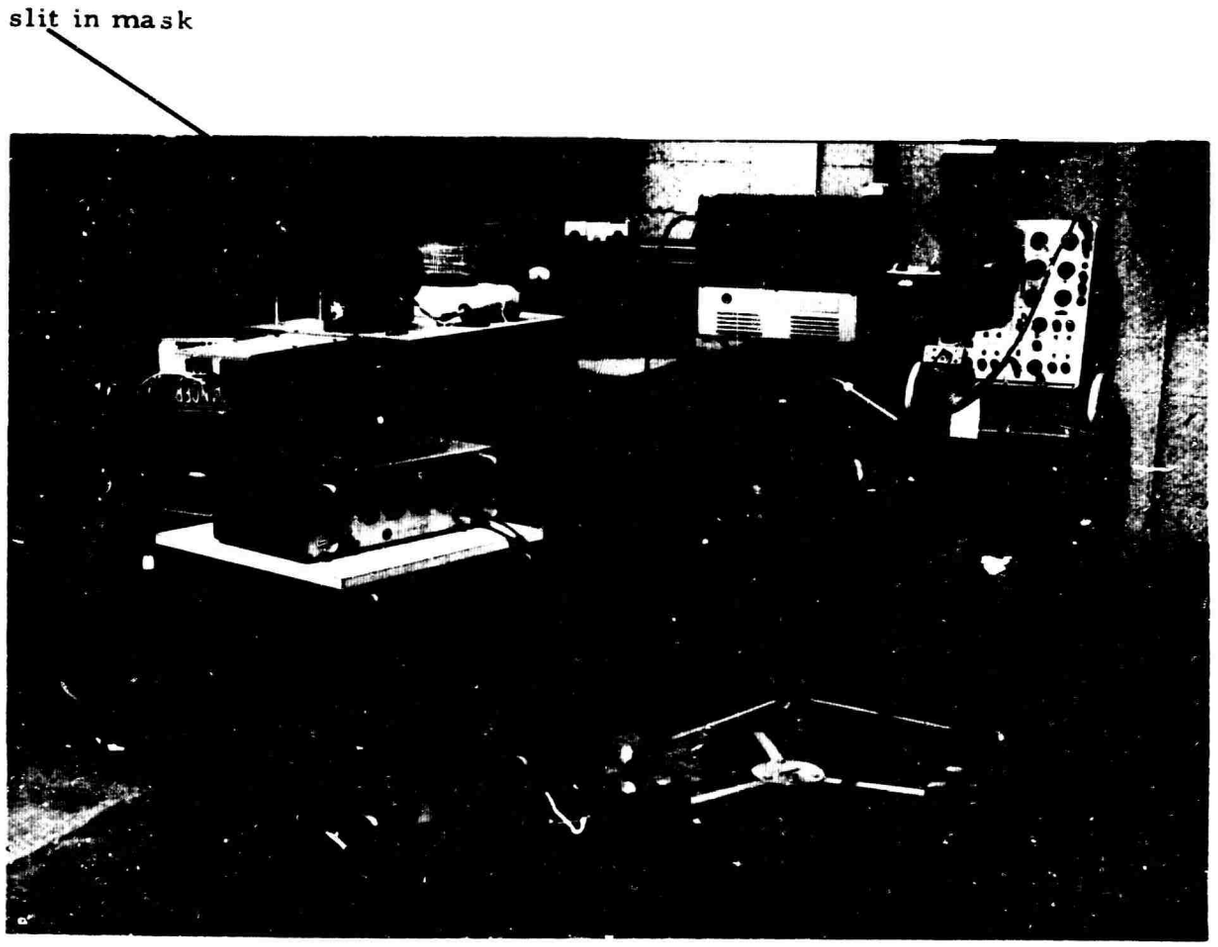

Streak Along Z axis

Figure IV - 6

Microdensitometer Setup

Figure IV - 7

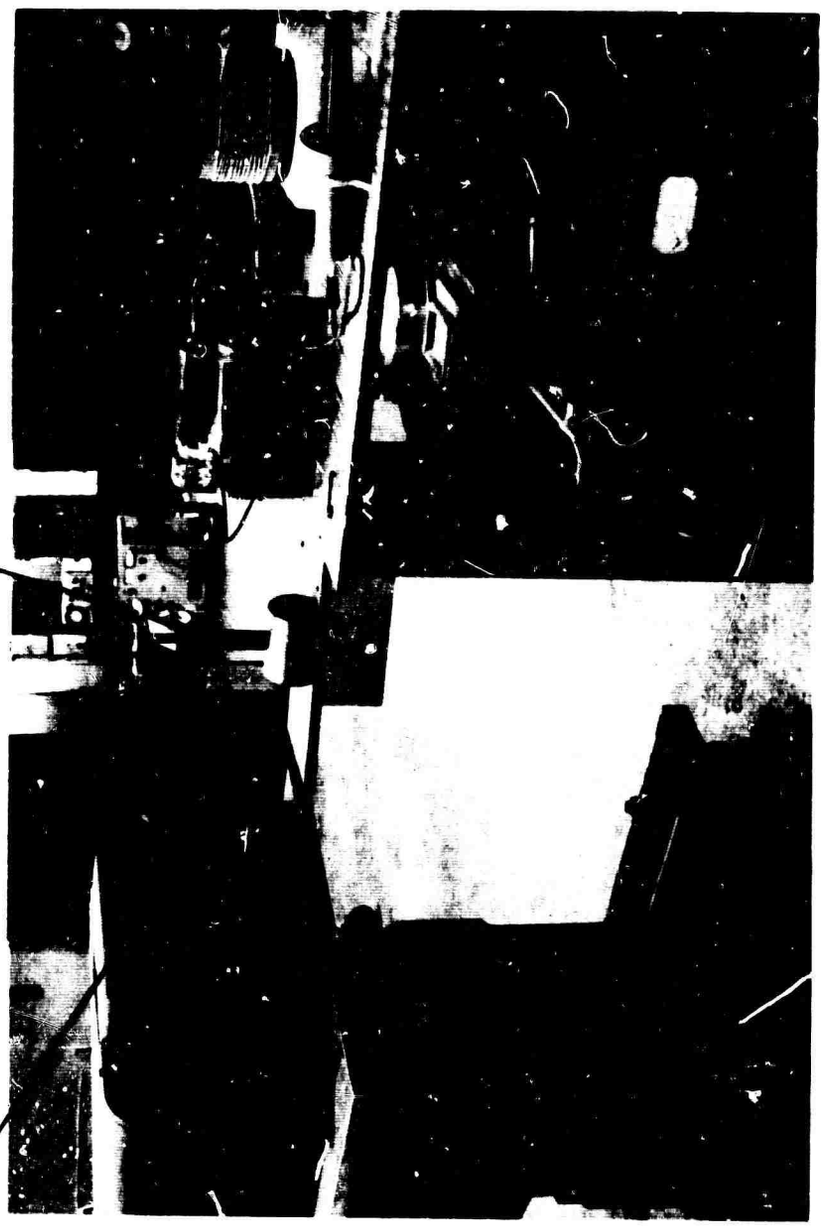

Spectrograph Setup

Figure IV - 8

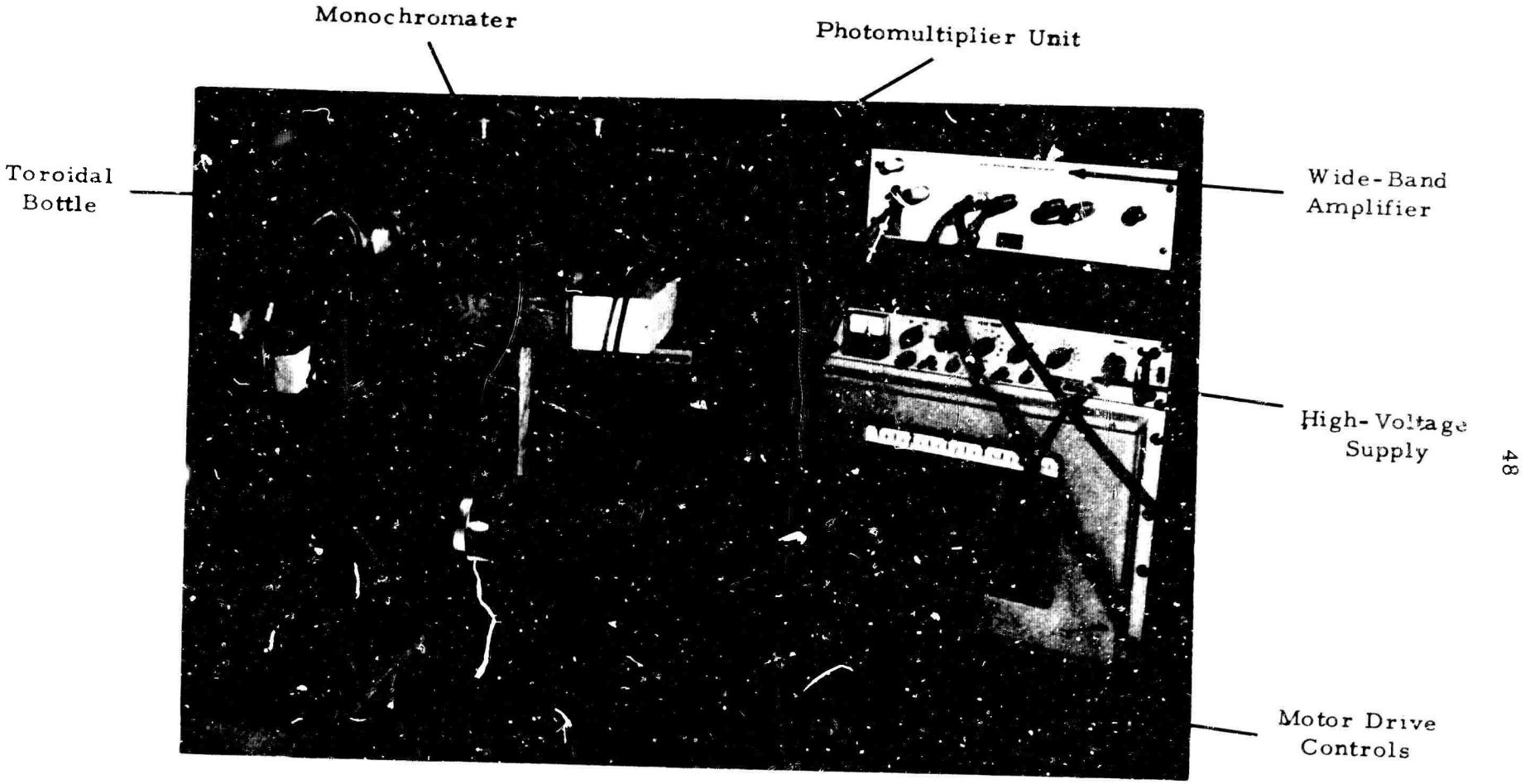

Monochromater Setup

Figure IV - 9

Type 151 Sampling Unit

Chart Recorder

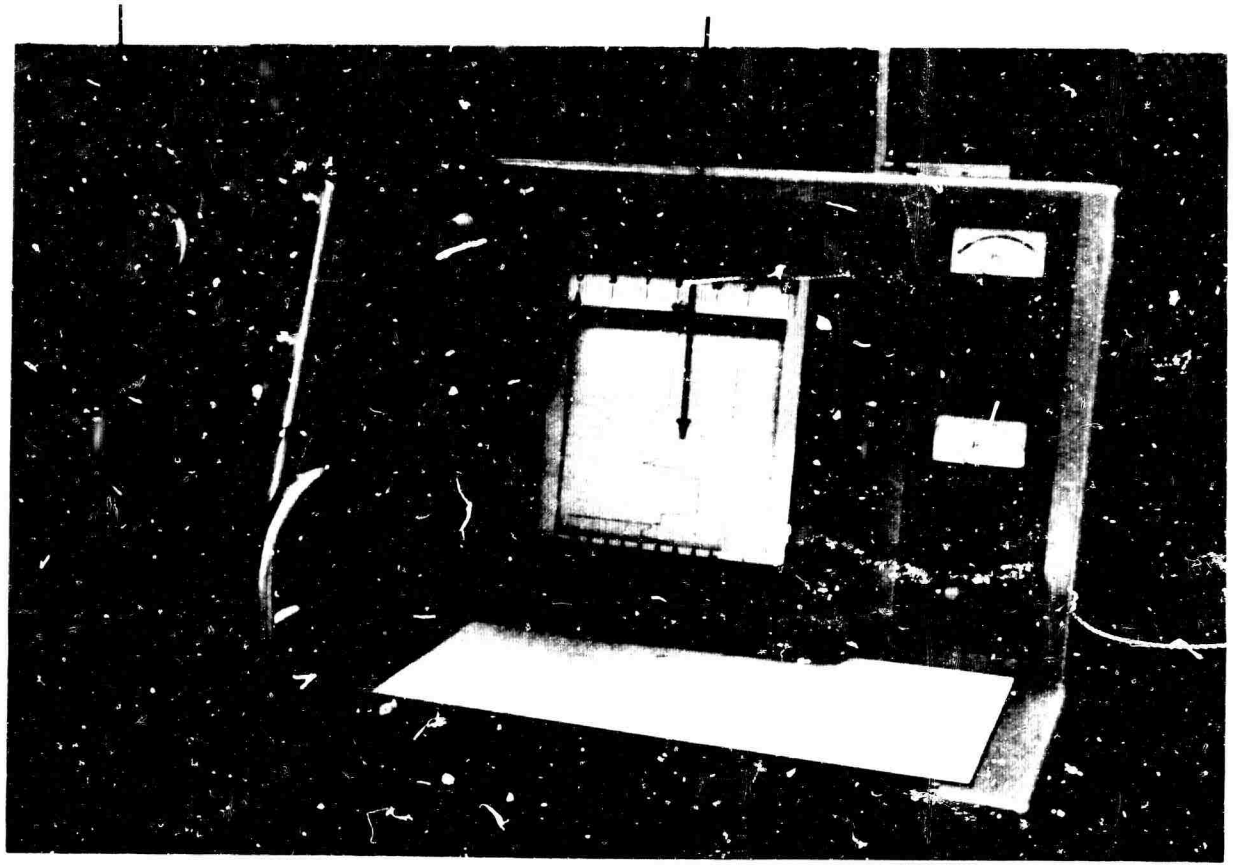

Monochromater Setup

Figure IV - 9 Cont'd

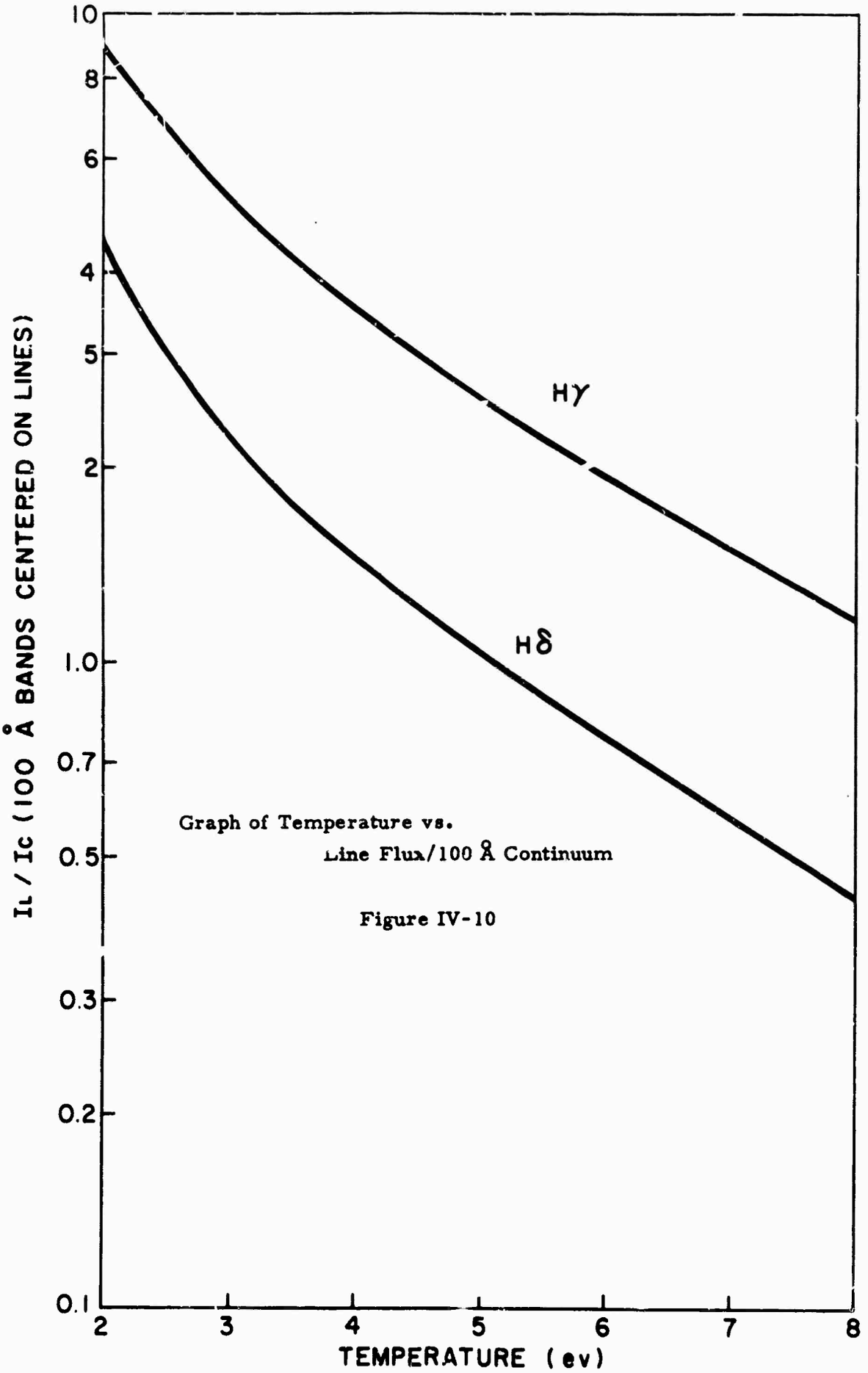

Graph of Temperature vs.
Line Flux/100 Å Continuum

Figure IV-10

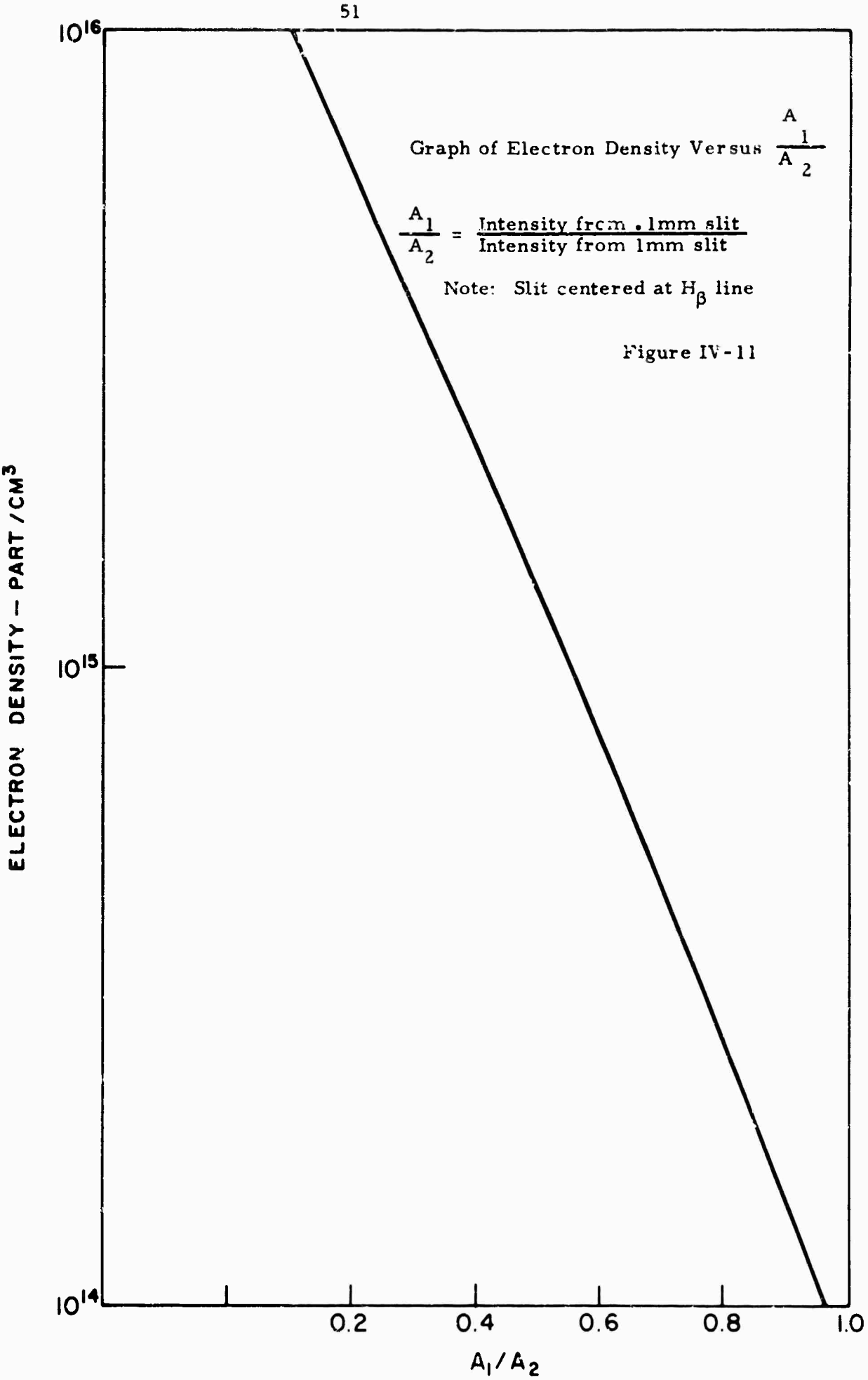

Graph of Electron Density Versus $\frac{A_1}{A_2}$

$\frac{A_1}{A_2} = \frac{\text{Intensity from .1mm slit}}{\text{Intensity from 1mm slit}}$

Note: Slit centered at H_β line

Figure IV-11

BLANK PAGE

CHAPTER V

EXPERIMENTAL FINDINGS

This chapter presents the results that were obtained by the instrumentation described in Chapter IV. First, the measurement of magnetic fields is given. Next the experimental results are presented for measurement of electron density and temperature. The following section gives the values of resistivity for various modulator voltages and plasma currents. The last two sections are concerned with the observation and measurement of growth rate for the Rayleigh-Taylor instability and the resistive instability.

A. Measurement of Magnetic Fields

Detailed measurements of the magnetic flux density were carried out on the narrow toroidal plasma bottle. The first measurements made on this type of plasma structure was done by H. Friedman,[16] who compared his data to a theoretical plasma model that consisted of a current sheet. Later, a more detailed study of the magnetic flux density was undertaken by J. Milleta[17]. He also compared the experimentally measured fields with a model that represented the current carrying plasma as being comprised of two rings. This model was a direct result of the examination of framing photographs such as those given in Figure V-29 which show the plasma structure in the narrow toroidal bottle being comprised of two rings or filaments.

The magnetic probes used were of two types, stationary and movable. The stationary probes were mounted on the side walls of the plasma bottle and the movable probes had the facility of measuring magnetic flux density both inside and outside the toroidal bottle. The probes were arranged so that all three components of magnetic field, Br, Bθ, and Bz could be

measured. The complete description of the magnetic probes and their position has been given in Chapter IV-C.

Shown in Figures V-1, 2, 3 are photographs of temporal variations of Br, Bθ, Bz respectively for different radial positions equidistant from the side walls of the toroidal bottle. Also shown for reference purposes is the primary current as a function of time. Detailed magnetic probe measurements were also made along the axial length of the outer circumference of the toroidal bottle.

These data for the three components of magnetic flux density are functions of time and space. To aid in the interpretation of this large amount of data, plots of flux lines were made at instants of time corresponding to one, two, three, and four microseconds after the beginning of the current pulse, The plots were made for a cross-section of the toroidal bottle, the r-z plane. Also shown in the plots, in out line form, is the perimeter of the bottle, and also, the magnetic flux density vectors that were calculated from the experimental data. The plots depicting lines of flux for various instants of time are shown in Figures V-4 through V-7 inclusive.

Examination of these figures reveals two separate flux linkages, which implies that the plasma structure consists of two current carrying rings. Moreover, the two flux patterns shown for each instant of time are not identical. This suggests that one plasma ring conducts more current than the other. This observation is also consistant with the fact that one current ring, the one with more flux linkages, has a greater outward radial motion. This motion can be related to the well known "magnetic piston" argument which stems from the $\underline{J} \times \underline{B}$ motor force. If the current in the ring is larger, then the $\underline{J} \times \underline{B}$ force increases, and the subsequent outward radial motion is faster.

Photographs also support the argument of separate filaments. In addition to Figure V-29 mentioned previously, another framing photograph that shows radial motion is given in Figure V-8 . In this figure, the camera is looking along the z axis through an observation window in a side wall of the toroidal bottle, The time sequence is given in the figure. Of particular interest are the photographs for instants of time at 1.0, 1.5, and 2.0 microseconds. Here two rings can be seen, one of them being at a smaller radial distance from the center of the toroidal bottle.

The current sheet model and the two ring model for the magnetic fields in the toroidal plasma discharge both neglect the curvature of the torodial structure and also assume that the radial dimension of the plasma is infinitesimally thin. A schematic of the theoretical models is given in Figure V-9. Solutions for the Br and Bz components of magnetic flux density using a current sheet model are given as:

$$Br = [\mu_o I(t)/2\pi d] \left\{ L_n [r^2 + (z+d/2)^2]/[r^2 + (z-d/2)^2] \right\} \qquad 5.1)$$

$$Bz = [-\mu_o I(t)/4\pi d] \left\{ \tan^{-1}[(z+d/2)/r] - \tan^{-1}[(z-d/2)/r] \right\} \qquad 5.2)$$

The total magnetic field is the superposition of the fields due to the plasma current sheet and the primary current flus their image fields, where it has been assumed that the magnetic transformer core is a semi-infinite magnetic wall. A sketch of this appears in the bottom portion of Figure V-9.

The same prescription is followed for the calculation of total magnetic flux density in the case of the two ring model. The equations for Br and Bz components are given below. The distance d′ represents the axial separation of the two rings. It is assumed that both rings conduct equal current.

$$Br = [\mu_o I(t)/4\pi] \left\{ (z-d'/2)/[r^2 + (z-d'/2)] + (z+d'/2)/[r^2 + (z+d'/2)] \right\} \qquad 5.3)$$

$$Bz = [-\mu_o I(t)/4\pi] \left\{ 1/[r^2 + (z-d'/2)^2] + 1/[r^2 + (z+d'/2)^2] \right\} \qquad 5.4)$$

The magnetic fields for both models are plotted for the following conditions :

modulator voltage ------ 12 kv

neutral gas pressure --- 500 microns Hq

plasma current ------- 3400 A; magnitude at 2 usec. after beginning of current pulse.

Figures V-10 and 11 show the Br and Bz components due to the models. Comparison with the flux plot for the time of two microseconds indicate that the actual field is not given in detail by either of the models. However, if the two ring model consisted of unequal currents in the rings, the difference between model and actual field distribution would be less.

Of more practical interest for the purposes of instability calculations is the value of the typical magnetic field , <B>, within the plasma. It was found that this magnetic flux density, <B>, expressed by

$$<B> = 10^4 u_o <I>/2L \text{ (gauss) where} \qquad 5.5)$$

L is the axial length of the plasma, matches the value of both model fields and the actual field associated with the portion of plasma in the center of the toroidal bottle.

The experiments on instabilities of the resistive type indicated their presence at times shortly before the peak of the current pulse, approximately two microseconds. At this time, the variation of magnetic flux density from outer plasma-vacuum to inner plasma-vacuum interface was 110 gauss to 360 gauss. This represents an average field of 235 gauss. For an L = 6 cm. and an $<I> = \frac{2}{\pi}$ Ipeak, where Ipeak = 3400A at two microseconds, we find that <B> is as follows :

$$<B> = 10^4 u_o \frac{<I>}{2L}$$

$$<B> = 226 \text{ gauss}$$

Calculation of the average model field at two microseconds yielded a value of 220 gauss.

Therefore, when magnetic flux density is required for instability calculations, the approximation expressed by equation 5.5) will be used.

B. Measurement of Electron Densities

Electron densities were measured in the toroidal plasma by observing the effect of Stark-broadening on the Hydrogen spectral lines in the Balmer Series. The theory of Inglis and Teller[18] was used to calculate den- from the experimental observation of line merging. Several line shapes were examined in detail, and comparison of these shapes with the theoretical ones presented by Griem[13] yield the electron density.

The first measurement of electron density employed the spectrograph set-up that is discussed in Chapter IV-F. In this measurement the density was not time resolved, since the shutter of the spectrograph remained open for approximately fifteen minutes.

A portion of the microdensitometered film appears in Figure V-12. Line merging was considered to be significant after the line labeled n = 10 because the wings of all succeeding lines overlap to a large extent. Using the formula given in equation4.2) of Chapter IV for density we have

$$N_e^{2/3} = \frac{1}{11.1\, n_m^5\, a_o^2}$$

where $n_m = 10$, and $a_o = .53 \times 10^{-8}$ cm. Solving, we have $N_e = 5.7 \times 10^{15}$ part/cm^3. This data was obtained with the modulator set at 10 kv and with a neutral gas pressure of 500 microns.

Later, a time resolved scan of the spectrum was achieved using the monochromater set-up as discussed in Chapter IV-G. The photomultiplier tube output of the monochromater was strobed or sampled at 4 microseconds from the beginning of the current pulse, while simultaneously, the monochromater grating was being rotated by the motor drive. The resultant

output is shown in Figure V-13, this figure of course, is only a portion of the total spectrum. The scale is 15.6 Å /inch and only the lines with principal quantum number n=6 through n=10 are shown. Of interest is that the line associated with n=10 is absolutely the last observable line; all succeeding lines are buried in the continuum. For n=10, we have again from the Inglis and Teller technique a density of 5.7×10^{15} part/cm^3. This value, however, is time resolved at 4 microseconds.

A more accurate determination of number density is to measure the half width of a Hydrogenic spectral line or to plot the profile itself, these measurements are then compared to the theory of Griem. The monochromater is adjusted so that it is set at the line core of H_β. Then the photomultiplier tube output is recorded with the exit slit set first at 0.1mm and then at 1.0mm. The ratio of outputs at these two slit openings represents a unique electron density. Such a curve is shown in Figure IV-11.

Data was taken for a range of neutral gas pressures and modulator voltages. The oscilloscope photographs or photomulitplier tube output show signal variation with time.

It was noticed that, continuum radiation was very large for the first microsecond, with its peak at about 1/2 microsecond. After one microsecond, continuum radiation was negligible when compared with the H_β light output. For times after one microsecond, therefore, continuum is neglected when computing density from the H_β profile. For shorter times, the continuum radiation must be subtracted from the H_β data.

Figure V-14 shows the following data: in photograph a are the primary current and core voltage as a function of time; photograph b shows photomultiplier tube output with narrow slit, and photograph c is taken with a wide-slit. This figure represents data from a torodial plasma driven at a modulator voltage of 12 kv and neutral gas pressure of 500 microns.

Graphs depicting the electron density as a function of modulator voltage and neutral gas pressure for instants of time corresponding to two and four microseconds after the beginning of the current pulse are shown in Figure V-15 to 18 inclusive.

These data represent the average electron density along the z axis. The computation of both spatially and temporally resolved electron densities is complicated since the plasma structure has motion and the electromagnetic fields associated with it are time-varying.

Inspection of Figures V-15 to 18 reveals that the trend is to increase electron density as voltage is increased. At 500 microns pressure, however, the density is fairly constant at about 6.5×10^{15} part/cm^3 regardless of voltage. Overall, there seems to be a general increase in electron density as time goes on. There is one exception, though, at 300 microns there is an anomaly between 12 and 14 kv for the density. At other pressures, the data seems more consistant.

One other independent check of number density was made. The line shapes and underlying continuum plots made for calculating temperature in the next section were used to measure the half widths of H_γ and H_δ. See Figures V-19 and 20. These scans were made in a manner similar to the scan shown in Figure V-13 except that the H_γ and H_δ scans are to a scale of 3.35 Å/inch on the chart. The half width of the spectral line is measured at 1/2 the peak line intensity, taking care to correct for the underlying continuum. Shown on the graphs are the "0" level, where monochromater shutter is closed, and the level of continuum under the line. This last level is a computed average taken from the far wings on both sides of the line. The calculated half width for H_γ and H_δ are 14.2 Å and 12 Å respectively.

The electron density is calculated using the following formula from Griem.[19]

$$N_e = C(N_e, T)\,\Delta\lambda_s^{3/2} \qquad 5.6)$$

where $\Delta\lambda_s$ = half width in angstroms

N_e = electron density in part/cm^3

$C(N_e, T)$ a coefficient that is only a weak function of density.

For H_γ, $C(N_e, T) \approx 3.61 \times 10^{14}$ and for H_δ we have $C(N_e, T) \approx 1.11 \times 10^{14}$

Therefore

$$N_e = 3.61 \times 10^{14} (14.2)^{3/2}$$

$$N_e = 1.9 \times 10^{16} \text{ part/cm}^3 \quad \text{from } H_\gamma$$

and

$$N_e = 1.11 \times 10^{14} (12)^{3/2}$$

or

$$N_e = 4.7 \times 10^{15} \text{ part/cm}^3 \quad \text{from } H_\delta$$

The scans from which these densities were calculated were done at a sampling time of 2.0 microseconds after the current pulse began. The modulator voltage was 10 kv and the neutral pressure was 500 microns. The electron density measured from H_β observations for these conditions was 6.7×10^{15} part/cm^3.

The densities computed from half widths of H_γ and H_δ are consistant with those obtained from profile analysis of H_β since the theory for Stark broadening of H_γ and H_δ is only accurate within 30% while that for H_β is known to be on the order of 5%. The merging of lines at essentially the same time yielded a Inglis - Teller calculation for electron density of 5.7×10^{15} part/cm^3.

Since there is agreement using independent checks, the measurements of electron density done in detail from observations of H_β should be reliable. One last check was made, however, this was a check to see if the plasma was optically thin. If this is not the case, then self absorption is taking place and the line profiles are altered. A correction must be then applied in order to calculate the correct electron density.

Instead of the usual technique of placing a mirror behind the plasma and then recording double the line intensity at the photomultiplier output for optical thinness, the following procedure was employed. A strobe lamp was placed behind the plasma bottle in such a way that the strobe lamp light output passed through the plasma and into the monochromater setup. The intensity of the strobe lamp was approximately the same as the H_β output of the plasma. The strobe lamp output for a 1.6 Å band centered at H_β was recorded separately and the H_β output of the plasma was recorded separately with the identical 1.6 Å band. Then, both sources were recorded simultaneously. This is shown as Figure V-21, the top photograph is H_β output, the middle is the plasma and strobe lamp both emitting light, and the bottom photograph is the strobe lamp output by itself. The signals shown in the top and bottom photographs when added together do result in the signal shown in the middle one. Therefore the plasma is optically thin for H_β.

C. Measurement of Temperature

A time resolved spectrogram of the Balmer spectral lines H_γ and H_δ and their surrounding continuum was made using a motor driven monochromater and sampling oscilloscope. The oscilloscope output was fed to a strip chart recorder. This experimental technique has been described in greater detail in Chapter IV-G.

The spectragrams of H_γ and H_δ are given in Figures V-19 and V-20 respectively. The wavelength scale is 3.35 Å/inch, and the spectrum was taken at two microseconds after the beginning of the current pulse. The original spectragrams consisted of more than 100 Å of continuum on either

side of the spectral line, making the plot several feet long. In order to present the data in this thesis, the line wings and outlying continuum were sliced off. However, the figures do shown the average value of continuum under the spectral line as calculated from the continuum magnitude 100 $\AA^{o}$ away from the line core. Also shown is the "zero" level; the level on the graph which corresponds to no light passing through the monochromater.

In Griem's book, "Plasma Spectroscopy", the relative line to continuum ratio is given on page 279 as the following equation :

$$\frac{I_L}{I_C} = \frac{3^{3/2}\pi^2(137a_o)^2 f g \exp\left[(E_H - E_L)/kT\right]}{2\lambda\Delta\lambda\, g_i \left[(g_{ff}/2)(kT/E_H)\exp(E_H/n'^2kT) + \sum_n (g_{fb}/n^3)\exp(E_H/n^2kT)\right]}$$

where

f = absorption oscillator strength of line

g = statistical weight of lower state

E_L = energy of lower state

E_H = ionization potential of Hydrogen

g_i = statistical weight of ion ground state

g_{ff} = free-free Gaunt factor

g_{fb} = free-bound Gaunt factor

Also n is summed from n = 3 to at least n = 6 for the Balmer series. Then n' = 7 is used, according to Griem[20]. The magnitude of I_L / I_C versus temperature for H_γ and H_δ were given as graphs in Figure IV-10 .

The spectrums shown in Figures V-19 and V-20 are linear plots. Therefore I_L/I_C is found by comparing areas under the curves. This is accomplished with a planimeter. First, the area under the curve extending $\pm$ 50$\AA^{o}$ from the spectral line core was measured. This represents $I_L + I_C$.

Next, areas that were 100Å wide and tangential to the first measured area were computed. These last areas were averaged and labeled as I_C. The sketch below shows the situat on.

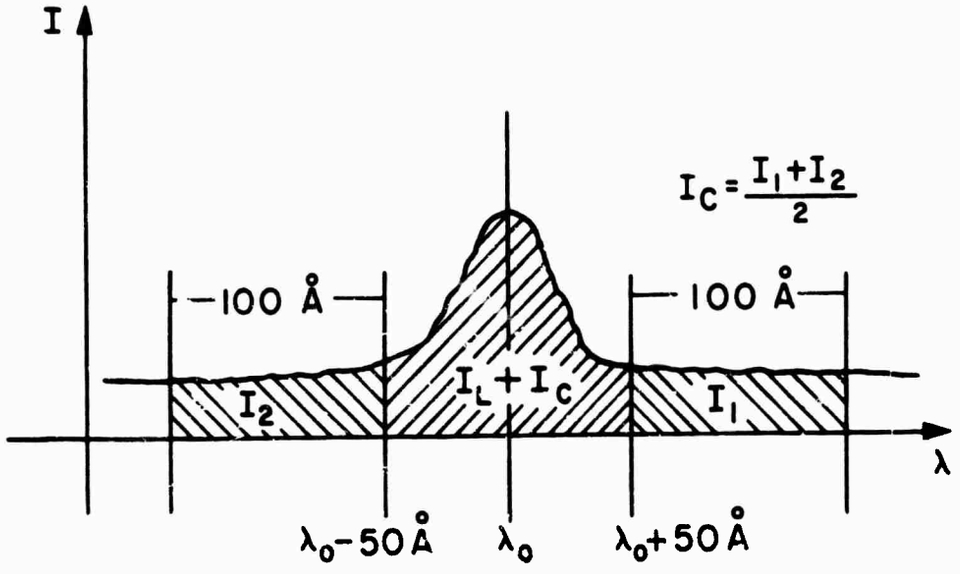

Application of the above procedure for the spectragrams of H_γ and H_δ yield I_L/I_C ratios of 1.38 and .363 respectively. Using Figure IV-10 we find a ratio of 1.38 for H_γ corresponds to a 7.5 ev electron temperature and .363 for the H_δ spectrum yields an 8.5 ev electron temperature. The agreement between the two calculations is approximately 12%.

Now we have to check to see if these temperatures are meaningful. First of all, are the measurements in error due to a failure to satisfy the assumption of local thermodynamic equilibrium, (LTE). Well according to Griem[21], if the plasma were time-independent and homogeneous, an electron density of

$$N_e \geq 7 \times 10^{18} \frac{1}{n^{17/2}} \left(\frac{kT}{E_H}\right)^{1/2} \quad \text{is required}$$

for a Hydrogen plasma so that LTE is satisfied to within 10%. For a temperature of 8ev., then the electron density must be more than 10^{13} part/cm^3 to insure LTE within 10%. Our densities are on the order of 5×10^{15} part/cm^3.

therefore the validity of the LTE assumption introduces negligible error for a plasma structure that is time-independent and homogeneous.

Our plasma may be considered to be transient and inhomogeneous. In that case more stringent requirements are set for the LTE assumption. Treating the transient case first, what we require is that the equilibrium time for satisfaction of LTE be about 10% of the plasma life time. In our case the plasma has a lifetime on the order of 10 microseconds, therefore we expect that the LTE equilibrium time must be less than 0.8 microseconds.

The following equation given by Griem[22] gives the equilibrium time for partial LTE, that is, for all principal quantum numbers above some n there can be total LTE.

$$\tau_n \approx \frac{4.5 \times 10^7}{n^4 N_e} \left(\frac{kT}{E_H} \right)^{1/2} \exp \left(\frac{2E_H}{n^3 kT} \right) \quad \text{sec}$$

Now for LTE in a homogeneous and stationary plasma at 8ev only an $N_e = 10^{13}$ was required. Substituting these values into the equation above for all $n \geq 5$, H_γ, H_δ, etc., we find that $\tau_n \approx \underline{5.7 \times 10^{-9} \text{ sec.}}$ The conclusion is that deviations from LTE between excited states is not serious.

Our plasma is also inhomogeneous. In addition to the previous requirements for LTE, we now must show that the gradient of electron temperature is small over distances that a particle can diffuse[23] in times of the order of 10^{-8} seconds as calculated in the previous section. For a temperature of 8ev the electron thermal velocity, $\bar{V}_e$ is

$$\bar{V}_e = \left(\frac{2kT}{m} \right)^{1/2}$$

and $\bar{V}_e = 1.68 \times 10^8$ cm/sec. Typical diffusion velocity in our plasma is 1×10^5 cm/sec. For a time interval of 10^{-8} seconds spatial motion due to temperature is on the order of 1cm., while that due to diffusion is 10^{-2}mm.

Since the magnitude of the temperature spatial gradient must be inversly proportional to the characteristic path length, it appears that the spatial requirement for LTE has been satisfied.

All in all, the experimental average electron temperature of 8ev. and the determination of electron number density $\approx 6 \times 10^{15}$ part/cm. from the previous section does not produce a paradox, or even a serious refutation of the LTE assumptions that are prescribed by Griem in order to generate theoretical working equations for calculation of temperature.

D. Determination of Resistivity

The magnitude of electrical resistivity associated with the plasma exerts a strong influence on the growth rate of the resistive instability, which has been observed in this experiment. The resistivity has been determined in two ways. First, the voltage-current measurements were used. The initial voltage across the modulator capacitors represents an electric energy source containing $\frac{1}{2} CV^2$ Joules, where C = modulator capacitance and V = initial voltage across the capacitor . All this energy is assumed to go into ohmic heating of the plasma and series resistor, R ext. The energy dissipated in the plasma is represented by an equivalent resistor, having the value $<R>$. Knowing the approximate geometry of the plasma, then the resistivity can be calculated, given $<R>$.

$$<\eta> = \frac{A<R>}{L} \qquad 5.7)$$

$<\eta>$ = equivalent resistivity.

$<R>$ = equivalent resistance .

L = mean circumference of plasma.

A = cross-sectional area of plasma.

The second method of determining resistivity stems from the temperature measurements made in the previous section. In this case, Spitzer[24] has

calculated an expression where $\eta \alpha T^{-3/2}$ (T is electron temperature) and the resistivity is only a weak function of electron density. His equation is given below.

$$\eta = \frac{5.21 \times 10^{-5} \, \mathrm{Ln}\Lambda}{T^{3/2}} \qquad 5.8)$$

$$\text{where} \quad \Lambda = 1.55 \times 10^{10} \, \frac{T^{3/2}}{N_e^{1/2}}$$

η = resistivity in ohm-meters

T = temperature in electron-volts

N_e = electron density in particles/cm^3.

When the experiment was being conducted, the core voltage and primary current signals were always displayed on a Tektronix 555 dual-beam oscilloscope. These displays were recorded on Polaroid 3000 ASA film for every modulator voltage setting and also for the various primary winding configurations. Typical voltage and current data are shown in Figure V-22. This figure shows data at modulator settings of 8, 10, 12, and 14 kilovolts. The neutral gas pressure of the Hydrogen was 500 microns and the inner primary winding had a uniform structure so that the current carrying plasma sheet in the toroidal bottle broke up into two filaments.

As mentioned previously, to calculate resistivity from data represented by Figure V-22 we equate electric energy of the modulator capacitor to ohmic heating. This relation is given in the equation below.

$$\frac{1}{2} CV^2 = (\langle R \rangle + R_{ext}) \int_0^T I^2(t)\, dt \qquad 5.9)$$

C = modulator capacitor

V = peak modulator charging voltage

$\langle R \rangle$ = average plasma resistance

R_{ext} = external modulator charging resistor

I(t) = plasma current as function of time, t.

The value of C is .0334 uf and of R ext is 11.5 ohms. However when R ext is reflected from the primary side of the transformer to the secondary side, the plasma region, then we have an effective R ext of $\frac{11.5}{n^2}$ or .068 ohns, where n represents a transformer turns ratio of n = 13. The term I(t) is the efective plasma current, which is n times the primary current. It was observed that I(t) is very nearly equal to $I_o \sin \omega t$ for $0 < \omega t < \pi$ according to the experimental data. Substituting the approximate form of I(t) into equation 5.9) and integrating, we find the following expression for $<R>$.

$$<R> = \frac{\omega}{\pi} C \left(\frac{V}{I_o}\right)^2 - R\,ext \qquad 5.10)$$

Application of equation 5.7) results in an expression for the resistivity.

$$<\eta> = \frac{A}{L}\left[\frac{\omega C}{\pi}\left(\frac{V}{I_o}\right)^2 - R\,ext\right]$$

or

$$<\eta> = \frac{A}{L}\left[\frac{C}{T}\left(\frac{V}{I_o}\right)^2 - R\,ext\right] \qquad 5.11)$$

where $A \approx 10^{-3}\ m^2$

$L \approx 3 \times 10^{-1}\ m$

T = length of current pulse in seconds of time .

The graph shown in Figure V-23 illustrates the behavior of V versus I_o for different modulator voltages and primary winding configurations. Examination of the graph indicated that the ratio, V/I_o, decreases for increasing V. According to equation 5.11), we come to the conclusion that $<\eta>$, the resistivity, decreases as V is made larger. Offsetting this relationship, however, is the dependence of T upon the modulator photographs. Inspection of Figure V-22 reveals that T decreases for increasing V.

In any case, $<\eta>$ was calculated from equation 5.11) for various V/I_o ratios and their corresponding T values. The results are shown in Figure V-24 where V is the ordinate and $<\eta>$ is the abscissa. An independent check for these values of $<\eta>$ can be made by using the measured values

of temperature and electron density given in sections C and B of this chapter respectively. These data can be used in Spitzer's formula, equation 5.8), in order to calculate $<\eta>$. With a modulator voltage of 12 kv and neutral gas pressure of 500 microns, the electron density was found to be 6.7×10^{15} part/cm^3 and the temperature due to line-continuum ratios for H_γ and H_δ was calculated as 7.5 and 8.5 electron volts respectively.

The resistivity according to the above data was found to be the following.

$$<\eta>\Big|_{H_\gamma} = 2.2 \times 10^{-5} \text{ ohm-meters}$$

$$<\eta>\Big|_{H_\delta} = 1.8 \times 10^{-5} \text{ ohm-meters}$$

These values are plotted on Figure V-24 for comparison purposes. The difference between the average resistivities calculated by the two techniques is less than 20%. Inclusion of inductive effects for equation 5.9) would decrease the calculated resistivity in the direction of that determined from temperature-density measurements. The additional complexity for a little better agreement did not appear justified at this time however.

E. Observation of Rayleigh-Taylor Instabilities

In this section, photographs are presented that indicate the onset of a Rayleigh-Taylor instability. The neutral gas pressure of the Hydrogen gas in the toroid was 50 microns Hg. The photographs were taken in the framing mode with the camera looking into the side-wall of the toroid along the major axis.

To correlate the experimental observations with the theory presented in Chapter II, the observed wavelength is compared with the predicted wavelength. The predicted wavelength depends on the plasma acceleration and the viscosity of the plasma. Viscosity depends on the ion density and temperture. Since the system is in LTE, we can substitute both the electron

density and temperature. This data was presented in sections B and C of this chapter. The plasma acceleration has been measured experimentally and compared favorably to a snowplow model by K. Stuart[25]. Both rectangular and cylindrical geometries were used as theoretical models and it was found that the difference in their solutions was insignificant. The following is a derivation of the snowplow model for both the rectangular and cylindrical geometries.

The following equation is for a snowplow model having rectangular geometry. A sketch of the geometry is shown below

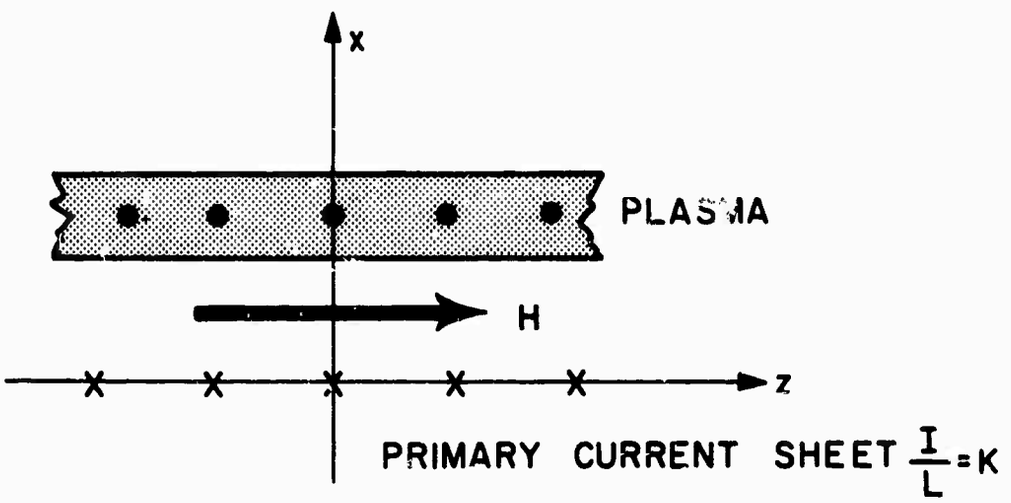

The model assumes that all plasma is swept up by a "magnetic piston" and is confined to a small region immediately ahead of this piston.

$$\frac{\mu_o H^2}{2} = \frac{d}{dt}\left(M\frac{dx}{dt}\right) \qquad 5.12)$$

where $H = K$

$$M = (m_c + m_i)\, n_o x = \rho_o x$$

Substituting, we have the following,

$$\frac{\mu_o K^2}{2\rho_o} = \frac{d}{dt}\left(x\frac{dx}{dt}\right) \qquad 5.13)$$

or

$$\frac{u_o}{\rho_o} \int_o^t d\tau \int_o^\tau K^2(\xi)\, d\xi = x^2 \qquad 5.14)$$

with the initial condition $x\Big|_{t_o} = 0$

Now since the discharge current is very close to a sine wave for the first half period the assumption is made that

$$K(t) = K_o \sin \omega t = \frac{I_o}{L} \sin \omega t \qquad 5.15)$$

Substituting equation 5.15) into equation 5.14) the solution shown below results

$$x = \left[\frac{u_o K_o^2}{8\omega^2 \rho_o} \left(2\omega^2 t^2 + \cos 2\omega t - 1 \right) \right]^{1/2} \qquad 5.16)$$

The experimental parameters of $K_o = 10^5 \text{ A/m}$, $\rho_o = 1.67 \times 10^{-5} \text{ kg/m}^3$, and $\omega = 10^6 \text{ r/s}$ were substituted into equation 5.16) in order to obtain the curve for the rectangular model shown in Figure V-25.

The cylindrical model is discussed next. Shown below is a sketch of the plasma configuration.

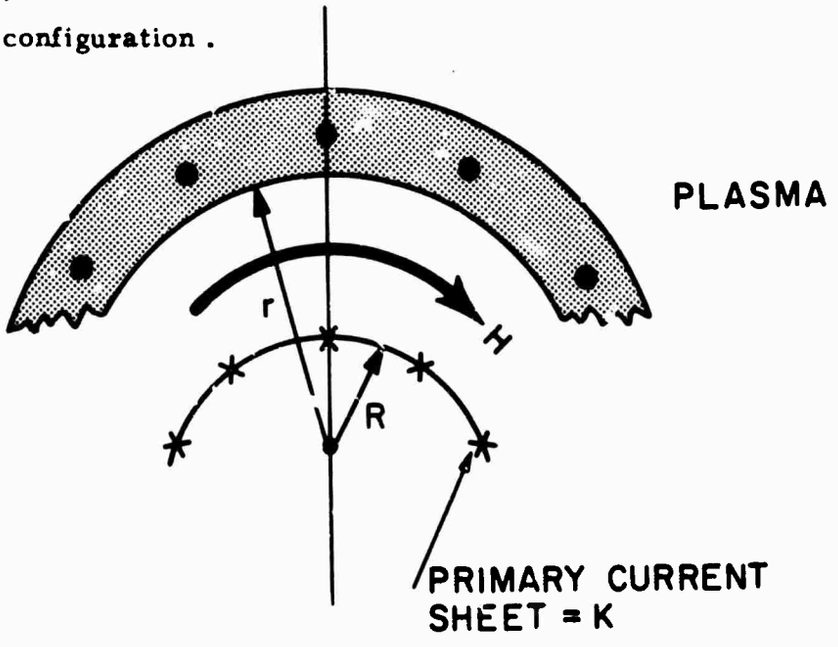

The following is the snowplow equation for the cylindrical case.

$$2\pi r \frac{\mu_o H^2}{2} = \frac{d}{dt}\left(M \frac{dr}{dt} \right) \qquad 5.17)$$

where $H = K$

$$M = \rho_o \pi (r^2 - R^2)$$

Equation 5.17) then becomes,

$$\frac{\mu_o K^2}{\rho_o} = \frac{d}{dt}\left(\frac{r^2 - R^2}{r} \frac{dr}{dt} \right) \qquad 5.18)$$

The corresponding integral equation with initial condition of $r\Big|_{t=o} = R$ is given below as

$$\frac{\mu_o}{\rho_o} \int_o^t d\tau \int_o^\tau K^2(\xi)\, d\xi = \int_R^r \left(y - \frac{R^2}{y} \right) dy \qquad 5.19)$$

By letting $K(t) = K_o \sin \omega t$ as done in the rectangular model, equation 5.19) can be integrated into the following form.

$$\frac{\left(\frac{r}{R}\right)^2 - 1}{2} - \mathrm{Ln}\left(\frac{r}{R}\right) = \frac{\mu_o K^2}{8\omega^2 \rho_o R^2} \left(2\omega^2 t^2 + \cos 2\omega t - 1 \right) \qquad 5.20)$$

Since this is a transcendental equation, the left and right hand sides of equation 5.20) is set equal to some function, F.

i.e.,

$$F = \frac{\left(\frac{r}{R}\right)^2 - 1}{2} - \mathrm{Ln}\,(r/R)$$

$$F = \frac{\mu_o K_o^2}{8\omega^2 \rho_o R^2} \left(2\omega^2 t^2 + \cos 2\omega t - 1 \right)$$

where $K_o = 10^5 A/m$, $\omega = 10^6 r/s$, $\rho_o = 1.67 \times 10^{-5} Kg/m^3$

and $R = 2.5cm.$

These two parametric equations are plotted in Figure V-26. Then for the same value of F, the corresponding r/R and t can be found. These values are plotted in Figure V-25 and form the locus of equation 5.20) which is the cylindrical solution to the snowplow model.

Figure V-27 shows a streak photograph of the plasma from which the experimental parameters used above were taken. The ordinate of the picture is radial distance and the abscissa is a time base. The inside edge of the plasma has been plotted on Figure V-25 to show correspondence with the rectangular and cylindrical models.

The conclusions derived from Figure V-25 are two fold. First, the difference between the rectangular and cylindrical solutions are insignificant. Therefore use of the rectangular geometry for the toroid is justified. This is the geometry used in Chapter II for the derivation of the instabilities. Second, the data taken from the streak photograph fit the model very well, and so the experimental plasma must be undergoing good snow plowing. For early times, when the Rayleigh-Taylor instability is developing, the radial trajectory is essentially quadratic. The acceleration, G, in this region is about $G \approx 2 \times 10^{10} m/s^2$.

The sequence of framing photographs shown in Figure V-28 show the onset of Rayleigh-Taylor instabilities as evidenced by the scalloped appearence of the inner edge of the plasma in the second and third photos. The exposure time for each photo was 50 nano seconds and the time interval between photos was 500 nano seconds . Examination of these photos indicate a wavelength of about $\lambda \approx 1cm.$ with a growth rate for the instability less than 0.5 microseconds.

We can use Marshall's[26] expression for viscosity which is :

$$\nu = \frac{1.89 \times 10^{15} \; T_i^{5/2}}{n_i \; \mathrm{Ln}\Lambda}$$

where ν = viscosity

$T_i = T_e$ = temperature in electron volts

$n_i = n_e$ = density in particles/cm^3 .

Substituting $T_i \approx 8$ ev. and $n_i \approx 5 \times 10^{15}$ part./cm^3 yields $\nu \approx 8$. Using equation 2.40) from Chapter II for the predicted minimum wavelength due to viscosity damped Rayleigh-Taylor instabilities we can compare with the observed wavelength.

$$\lambda \min = 2\pi G^{-1/3} \nu^{2/3} \text{ where } \nu \approx 8, \; G \approx 2 \times 10^{10} .$$

Solving the above equation we get that

$$\lambda \min = .93 \text{ cm} .$$

This is in good agreement with a value of 1 cm. found in the experiment.

F. Observation of Resistive Instabilities

Initially, experimental investigation of the toroidal plasma discharge was directed towards the radial motion. These first experiments were performed on the narrow bottle and the plasma was considered to be uniform in the axial direction in order to simplify the construction of a theoretical model. The validity of the assumption mentioned above was checked by taking framing pictures of the plasma in the r - z plane.

These photographs shown in Figure V-29 show a time sequence of 0.5 microsecond intervals. It is obvious that there are two filaments and their separation increases as time progresses. The dark vertical bars appearing in the photographs are the individual wires making up the outer winding on the toroidal bottle. The modulator voltage was 6kv and gas pressure was 500 microns; the same values used when taking magnetic probe measurements in Chapter V-A . Comparison of magnetic flux mappings for various times

presented in Chapter V-A with the framing photographs of plasma luminosity prove that the luminosity coincides with the location of the plasma current filaments.

The breakup of plasma into separate rings and the axial behavior, in general, was believed to be a type of resistive instability. In order to examine this phenomena in greater detail two major modifications were made. First, the theory of resistive instabilities assumes a uniform sheet of plasma in the presence of both a perturbing magnetic field and either a uniform conductivity or a spatially varying conductivity across the thickness of the plasma sheet. It is desirable to have an experimental plasma that is initially uniform in keeping with the theoretical model. However, it was noticed that the photographs in Figure V-29 did not really appear to have a uniform configuration at the beginning of the time sequence. This problem was solved by the introduction of r.f. preionization as discussed in Chapter III. The preionization of the toroidal plasma results in an axially uniform plasma. Second, only two rings were observed when conducting experiments on the narrow toroidal bottle and it was thought desirable[27] to excite more than two rings in any way possible so that the data might be more comprehensive. To this end a second bottle was constructed that was twice the width of the narrow bottle, the maximum width of the second bottle being determined by the dimensions of the transformer core. Also it was found that inserting in the annulus of the toroidal bottle a primary winding with spatial periodicity, the number of plasma rings that developed was a function of that periodicity. (The details of primary winding construction are given in Chapter III). It was found that if the primary winding is divided into n identical coils placed in succession along the axis, then the plasma would split into n+1 separate rings of filaments.

Experiments conducted on this second bottle were performed at modulator voltages ranging from 8kv to 20kv but only data from 8kv to 14kv was compiled since higher modulator voltages resulted in electrical noise

so large that the data was deemed unreliable. Neutral gas pressure was varied between 1 torr and 100 microns. The manifistation of resistive instabilities as filament formation was evident from 1 torr to about 300 microns. Below 300 microns radial motion becomes dominent and at about 150-100 microns evidence of Rayleigh-Taylor instabilities appear.

The data that follows consists of photographs depicting development of either two, three, or five filaments from a plasma that is initally axially uniform. The modulator voltage was varied between 6kv and 14kv, and the neutral gas pressure was 0.5 torr (500 microns).

The first set of data are framing photographs of a plasma developing into two filaments; this is shown as Figure V-30. Photographs showing three and five filament development are given in Figure V-31 and Figure V-32 respectively. Modulator voltage was 12kv for the plasma photographs just mentioned. Photographs were taken at other modulator voltages also.

Of prime interest is the quantitative determination of growth rate for the instability that has been photographed. To accomplish this aim a model has been devised that related the growth rate to the separation between the filaments that were observed on the framing photographs.

First of all, the theory predicted an exponential growth rate, $e^{\omega t}$ with $\omega > 0$, for the instability. Also there is a characteristic wavelength associated with the instability. Using the above information the plasma current is assumed to have the following form.

$$I(z,t) = I_o - i_o(e^{\omega t} - 1) \cos kz \qquad 5.21)$$

where I_o is tha plasma current in the absence of any perturbation, i_o is the perturbation current, and k is the wavenumber of the instability.

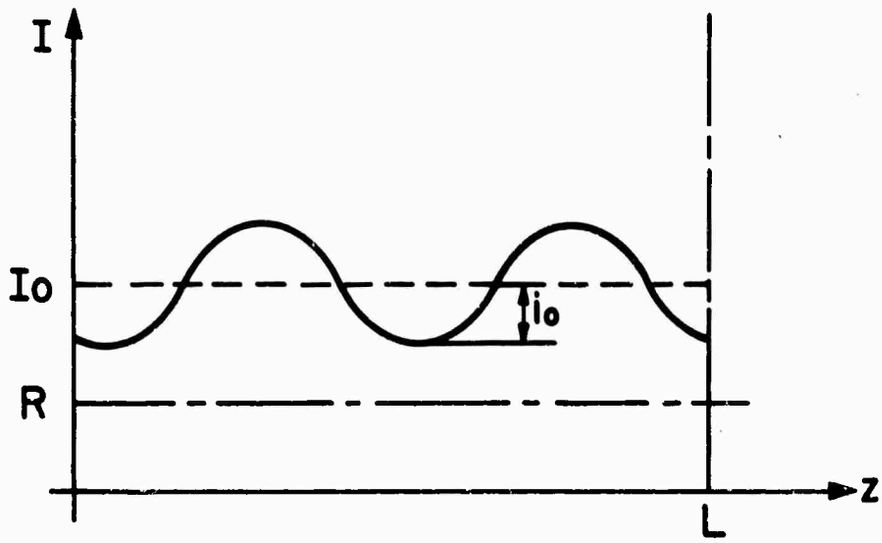

Now let the light intensity emitted by the plasma be proportional to I^2 where

$$I^2(z,t) = I_o^2 \left[1 - 2 \frac{i_o}{I_o} \left(e^{\omega t} - 1 \right) \cos kz + \left(\frac{i_o}{I_o} \right)^2 \left(e^{\omega t} - 1 \right)^2 \cos^2 kz \right] \qquad 5.22)$$

Let ξ be the position of $I^2(\xi, t) = R^2$ where R^2 is a constant and it denotes the threshold light intensity which exposes the film. In other words, the dark area separating the filaments on the photograph was the result of light intensity $< R^2$. In addition we define a function, F, with the following property:

$$F(z,t) = I^2 - R^2 \qquad 5.23)$$

where $F(\xi, t) \equiv 0$

Note: from the curve given above, ξ is defined only if $R \geq I_o - i_o (e^{\omega t} - 1)$.

Using the chain rule we have

$$\frac{dF}{dz} = \frac{\partial F}{\partial z} + \frac{\partial F}{\partial t} \frac{dt}{dz} \qquad 5.24)$$

where

$$\frac{1}{I_o^2} \frac{\partial F}{\partial z} = 2k \frac{i_o}{I_o} \left(e^{\omega t} - 1 \right) \sin kz \left[1 - \frac{i_o}{I_o} \left(e^{\omega t} - 1 \right) \cos kz \right] \qquad 5.25)$$

and

$$\frac{1}{I_o^2}\frac{\partial F}{\partial t} = -2\omega \frac{i_o}{I_o} e^{\omega t} \cos kz \left[1-\left(\frac{i_o}{I_o}\right)^2 \left(e^{\omega t}-1\right)\cos kz\right] \qquad 5.26)$$

Now $$\lim_{z\to\xi} \frac{dF}{dz} = 0 \quad \text{since } F(\xi, t) \equiv 0 .$$

Therefore $$\lim_{z\to\xi} \frac{dz}{dt} = \lim_{z\to\xi} - \frac{\partial F/\partial t}{\partial F/\partial z}$$

or $$\frac{d\xi}{dt} = \dot{\xi} = \frac{2\omega \frac{i_o}{I_o} e^{\omega t} \cos k\xi}{2k \frac{i_o}{I_o} (e^{\omega t}-1) \sin k\xi} \qquad 5.27)$$

and finally $$\dot{\xi} = \frac{\omega}{k} \cdot \frac{\cot k\xi}{(1-e^{-\omega t})} \qquad 5.28)$$

We can integrate equation 5.28) to get $\xi = \xi(t)$.

$$\int_{\xi_o}^{\xi} \tan k\eta \, d\eta = \frac{\omega}{k} \int_{to}^{t} \frac{d\tau}{1-e^{-\omega t}} \qquad 5.29)$$

Equation 5.29) integrates to the expression given below.

$$\ln \frac{\cos k\xi}{\cos k\xi_o} = \left[-\omega t - \ln(1-e^{-\omega t})\right] - \left[-\omega t_o - \ln(1-e^{-\omega t_o})\right] \qquad 5.30)$$

If t_o is the minimum time for ξ to be realizable, then we know $\cos k\xi_o = 1$ since it corresponds to $R = I_o - i_o(e^{\omega t_o}-1)$

$$\therefore \quad \ln \cos k\xi = -\omega(t-t_o) - \ln \frac{1-e^{-\omega t}}{1-e^{-\omega t_o}} \qquad 5.31)$$

This can be written as

$$\cos k\xi = \frac{I_o - R}{i_o(e^{\omega t}-1)} \quad \text{where} \quad e^{\omega t_o}-1 = \frac{I_o - R}{i_o}$$

or $$\xi = \frac{1}{k} \cos^{-1}\left[\frac{I_o - R}{i_o(e^{\omega t}-1)}\right] \quad \text{for} \quad t \geq t_o \qquad 5.32)$$

For the purposes of the experiment, we examine the photographs and determine ξ_1 and ξ_2 at times t_1 and t_2 respectively. A more useable form of equation 5.32), then, is a difference formula that yields ω, the growth rate.

$$\therefore \quad e^{\omega t_{1,2}} = \frac{I_o - R}{i_o} \quad \frac{1}{\cos k\xi_{1,2}} + 1$$

or $$\omega t_{1,2} = \ln\left[1 + \frac{I_o - R}{i_o} \quad \frac{1}{\cos k\xi_{1,2}}\right] \qquad 5.33)$$

we know $I_o >> R$, $I_o > i_o$ and therefore $\frac{I_o - R}{i_o} > 1$

Also $$\frac{1}{\cos k\xi_{1,2}} > 1 ,$$

So $$\omega t_{1,2} \approx \ln\left[\frac{I_o - R}{i_o} \quad \frac{1}{\cos k\xi_{1,2}}\right]$$

and $$\omega \approx \frac{1}{t_2 - t_1} \ln \frac{\cos k\xi_1}{\cos k\xi_2} \qquad 5.34)$$

The equation above is then used for calculating growth rate from the values of ξ and t measured on the framing photographs. The time interval between framing photographs is 0.5 microseconds, so $t_2 - t_1$ will always be some integer multiple of that time. The values of ξ are read from the photograph using a 7 eye loop that incorporates a scale marked off in 0.1 millimeter divisions. The width of the bottle is 12 centimeters and the image on the photograph is 28 millimeters, therefore all readings taken with the eye loop should be multiplied by $^{120}/_{28}$ or 4.3 times. The following table, Table I, lists the values of ξ and t measured from photographs taken of the different filament configurations for various modulator voltages.

Table I

Two Filaments ($k = .5 cm^{-1}$)

kv	ξ_1(cm)	ξ_2(cm)	ΔT(usec)	$\omega \times 10^{-5} (sec^{-1})$
8	1.25	1.75	.5	4.8
10	1.75	2.25	1.0	3.8
12	1.5	2.25	1.0	5.3
14	1.0	2.0	1.0	4.8

Three Filaments ($k = 1.045 cm^{-1}$)

kv	ξ_1(mm)	ξ_2(mm)	ΔT(usec)	$\omega \times 10^{-5} (sec^{-1})$
8	7.53	9.67	.5	5.2
10	4.1	6.45	.5	2.7
12	4.3	6.45	.5	2.8
14	5.37	7.5	.5	3.6

Five Filaments ($k = 1.6 cm^{-1}$)

kv	ξ_1(mm)	ξ_2(mm)	ΔT(usec)	$\omega \times 10^{-5} (sec^{-1})$
8	5.62	7.5	.5	1.08
10	3.75	5.62	.5	5.7
12	5.62	7.5	1.0	5.4
14	3.35	5.62	.5	6.1

Another method for obtaining the growth rate of the instability is to take streak photographs of the plasma instead of framing photographs. Then, a microdensitometer scan of the streak photograph yields the variation of light intensity generated by the plasma directly. This method is discussed in Chapter IV-E.

Streak photographs of two, three, and five filament configurations were obtained for various modulator voltages. Examples of such photographs are given in Figures V-33, V-34, and V-35 for two, three, and five filaments respectively. The modulator voltage in these last three figures was set at 8kv and then 10kv for each of the figures.

Shown in Figure V-36 is a calibration photograph of light intensity obtained with a photodiode for the five filament case. Simultaneously a streak photograph was taken. The microdensitometer trace for this last photograph is shown in Figure V-37 and finally Figure V-38 provides the calibration curve that is used to translate succeeding microdensitometer scans of streak photographs to equivalent intensity plots. Separate calibration curves are made for each filament configuration and in particular for each experimental run to insure that variations in exposure time, development time of film, etc. do not influence the data.

A typical data reduction procedure proceeds as follows. First the streak photograph is marked at known times along its time base. Then scans are made at these times across the axis of the image. Typical scans of a five filament streak photograph for a modulator voltage of 12kv are shown in Figures V-39 to 41 inclusive and represent scans one microsecond apart. Attention is now fixed on one of the filaments and its peak percentage of transmission and minimum value of percentage transmission between two filaments are recorded for each microdensitometer scan. These values are then converted to relative light intensity via the calibration curve. Next the ratio of peak intensity to minimum intensity is formed. A ratio equal to one,

of course, indicates growth has not yet begun. Ratios greater than one are the result of an instability growing. Table II below illustrates a typical calculation.

Table II

Five Filaments At 12kv

% Trans.

Time(us)	1	2	3
peak	3.6	2.0	2.6
min	3.8	2.2	3.2

Rel. Ampl.

Time(us)	1	2	3
peak	2.37	~1.4	3.8
min	3.8	~1.4	2.75

Time(us)	1	2	3
ratio	1.065	~1.0	1.38

Now to find the growth rate, which is supposedly exponential, the ratio of the numbers in the last row of the table above is taken for the times of two and three microseconds. Then $1.38 = e^{\omega t}$ where t is one microsecond. Solving. the growth rate must be $\omega = 3.17 \times 10^{5}$ sec.$^{-1}$. This prescription is followed for reducing the streak photographs for every filament configuration and impressed modulator voltage. A summary of such calculations is given in Table III as a listing of growth rate for different combinations.

Table III

Growth Rate Determined From Streak Pictures

Modulator Voltage (kv)	Two Fil. $\omega \times 10^{-5}$	Three Fil. $\omega \times 10^{-5}$	Five Fil. $\omega \times 10^{-5}$
8	1.54	1.1	1.1
9	1.55	1.07	1.7
10	1.33	0.99	1.95
11	1.35	0.95	2.5
12	1.3	0.96	3.17
13	1.75	1.1	2.51
14	1.6	0.98	2.87

In order to correlate the observed growth rates of the instability with the theoretical behavior of resistive instabilities a graph is plotted from the experimental data. The graph is a plot of p versus S where:

$$p = \omega \tau_R$$

$$S = \tau_R / \tau_H$$

and

$$\tau_R = \frac{\mu_o a^2}{\langle \eta \rangle}$$

$$\tau_H = \frac{a(\mu_o \langle \rho \rangle)^{1/2}}{\langle B \rangle}$$

Values of ω as determined from framing and streak photographs are given in Tables I and III respectively. The resistive diffusion time, τ_R, is calculated for a plasma width of $a \approx 2$ centimeters and various $\langle \eta \rangle$ that were determined in section D of this chapter for different modulator voltages and current configurations. Refer to Figure V-24. The parameter $\langle \rho \rangle = m_i \langle n \rangle$, where m_i is the Hydrogen ion mass, has been evaluated in Chapter V-B for $\langle \eta \rangle$ at a time of two microseconds. Since this is approximately the same

instant of time that μ was evaluated, calculations of $<p>$ are acceptable. Values of $<\eta>$ are selected from the curve for 500 microns pressure. Magnetic flux density, $<B>$, is calculated from equation 5.5) of section A ir this chapter. For convienience, it is repeated below.

$$<B> = \mu_o \frac{<I>}{2L} \quad \text{Weber/m}^2$$

where $<I> = \frac{2}{\pi} I_{peak}$

L = equivalent axial length of plasma

Table IV gives a tabulation of all the parameters mentioned above together with the calculation of τ_R, τ_H, S, and p for a plasma with two filaments being generated. Similar information is given by Tables V and VI for the three and five filament case respectively.

Mod. Voltage (kv)	Peak Current (ka)	$\langle r_i \rangle \times 10^5$	$\langle \eta \rangle \times 10^{-15}$	$\tau_R \times 10^6$	$\tau_H \times 10^6$	S	Normalized Framing p	Growth Rate Streak p
8	2.8	4.7	5.2	10.7	2.88	3.8	5.1	1.65
9	3.1	4.1	6.0	12.2	2.84	4.3		1.9
10	3.6	3.5	6.7	14.3	2.55	5.6	5.4	1.9
11	4.1	2.9	7.3	17.3	2.33	7.4		2.35
12	4.4	2.6	7.7	19.3	2.24	8.6	10.2	2.5
13	4.7	2.35	7.5	21.3	2.1	10.2		3.7
14	5.2	2.1	7.2	23.9	1.83	13.1	11.2	4.0

Table IV

Two Filaments

Mod. Voltage (kv)	Peak Current (ka)	$\langle\eta\rangle \times 10^{5}$	$\langle\eta\rangle \times 10^{-15}$	$\tau_R \times 10^{6}$	$\tau_H \times 10^{6}$	S	Normalized Growth Rate Framing p	Streak p
8	2.8	4.6	5.2	10.9	2.88	3.8	5.6	1.2
9	3.0	4.1	6.0	12.2	2.94	4.2		1.3
10	3.7	3.45	6.7	14.6	2.48	5.9	3.9	1.45
11	4.2	2.8	7.3	17.9	2.27	7.9		1.7
12	4.5	2.55	7.7	19.7	2.19	9.0	5.5	1.9
13	4.85	2.25	7.5	22.3	2.03	11.0		2.5
14	5.3	2.05	7.2	24.5	1.8	13.6	8.8	2.4

Table V

Three Filaments

Mod. Voltage (kv)	Peak Current (ka)	$\langle\eta\rangle \times 10^{5}$	$\langle\eta\rangle \times 10^{-15}$	$\tau_R \times 10^{6}$	$\tau_H \times 10^{6}$	S	Normalized Framing p	Growth Rate Streak p
8	2.8	4.7	5.2	10.7	2.88	3.8	1.15	1.2
9	3.15	4.05	6.0	12.4	2.8	4.4		2.1
10	3.75	3.4	6.7	14.8	2.44	6.1	8.4	2.9
11	4.25	2.8	7.3	17.9	2.24	8.0		4.5
12	4.6	2.5	7.7	20.0	2.14	9.3	10.8	6.3
13	4.85	2.25	7.5	22.3	2.03	11.0		5.6
14	5.45	2.0	7.2	25.1	1.75	14.3	15.3	7.2

Table VI

Five Filaments

We now have p versus S for all the filament configurations and these data are plotted in the graph shown in Figure V-42. The data taken from framing photographs are plotted as curves distinct from those reduced from streak photographs since the method of analysis was different for the two types of photos. For comparison purposes, a plot of $p = S^{2/5}$ is included. This corresponds to the case of $\alpha = 1$. Also included is a curve calculated by J. Wesson[28] using a digital computer. He set $\alpha = 1$ and did a numerical analysis, making no approximations for solving the basic set of equations derived by F. K. R. The asymptotic solution found by F. K. R. was, of course, $p \sim \alpha^{\pm 2/5} S^{2/5}$ for the rippling and tearing modes.

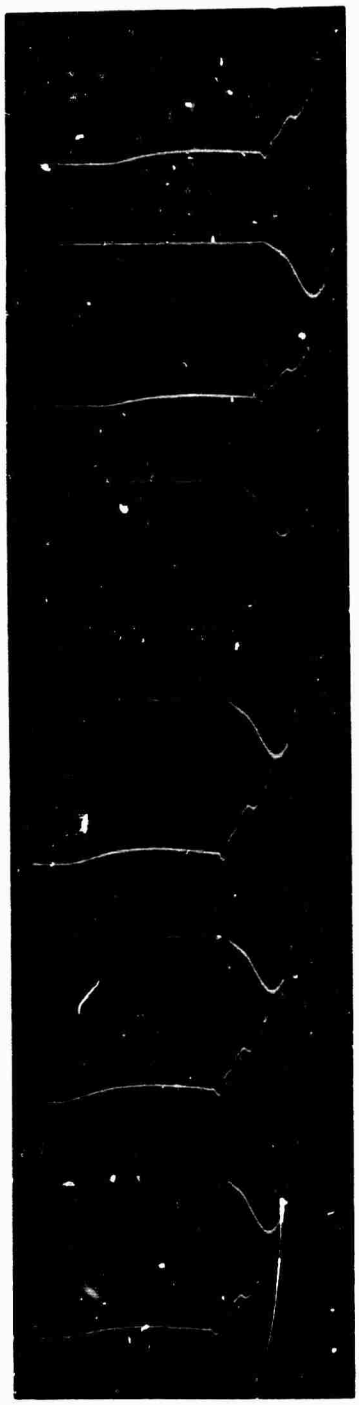

A.

B. Field - 136 gauss/box
radius 3.656 cm.

A.

B. Field - 136 gauss/box
radius 4.156 cm.

A.

B. Field - 136 gauss/box
radius 4.656 cm.

A.

B. Field - 68 gauss/box
radius 5.156 cm.

A.

B. Field - 68 gauss/box
radius 5.656 cm.

A.

B. Field - 68 gauss/box
radius 6.156 cm.

time scale - 2usec./box

A. Primary current 145 amps./box

B_r Magnetic Probe - Center of Discharge

Figure V-1

A.

B. Field - 68 gauss/box
radius 6.656 cm.

A.

B. Field - 34 gauss/box
radius 7.156 cm.

A.

B. Field - 34 gauss/box
radius 7.5 cm.

time scale - 2 usec./box
A. Primary current 145 amps./box

Figure V-1 Continued

A.

B. Field - 32 gauss/box
radius 3.656 cm.

A.

B. Field - 32 gauss/box
radius 4.156 cm.

A.

B. Field - 32 gauss/box
radius 4.656 cm.

A.

B. Field - 32 gauss/box
radius 5.156 cm.

A.

B. Field - 32 gauss/box
radius 5.656 cm.

A.

B. Field - 32 gauss/box
radius 6.156 cm.

time scale - 2 μsec./box A. Primary current 145 amps./box

B_θ Magnetic Probe - Center of Discharge

Figure V-2

A.

B. Field - 16 gauss/box
radius 6.656 cm.

A.

B. Field - 16 gauss/box
radius 7.156 cm.

A.

B. Field - 8 gauss/box
radius 7.5 cm.

time scale - 2 usec./box
A. Primary current 145 amps./box

Figure V-2 Continued

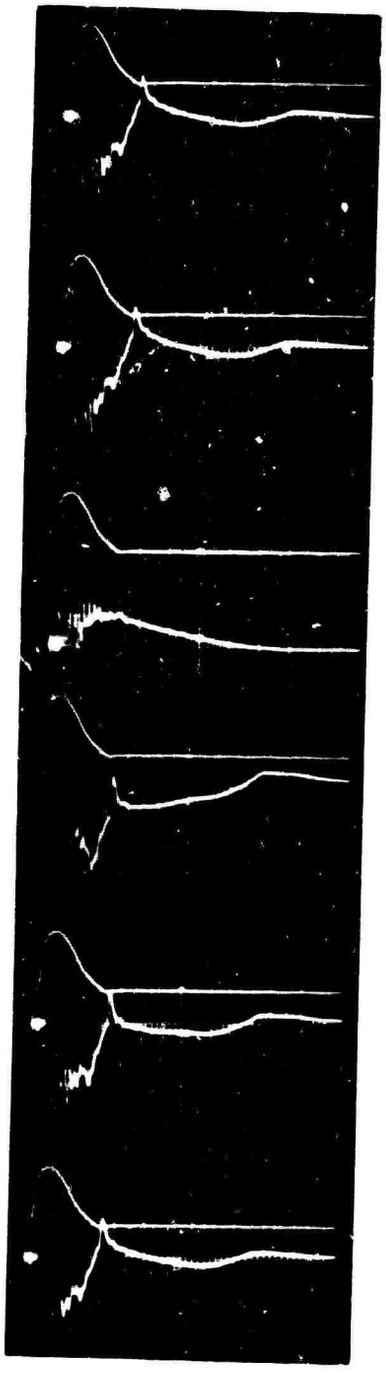

A.

B. Field - 32 gauss/box
radius 3.656 cm.

A.

B. Field - 16 gauss/box
radius 4.156 cm.

A.

B. Field - 8 gauss/box
radius 4.656 cm.

A.

B. Field - 8 gauss/box
radius 5.156 cm.

A.

B. Field - 8 gauss/box
radius 5.656 cm.

A.

B. Field - 8 gauss/box
radius 6.156 cm.

time scale - 2 usec./box A. Primary current 145 amps./box

B_z Magnetic Probe - Center of Discharge

Figure V-3

A.

B. Field - 8 gauss/box
radius 6.656 cm.

A.

B. Field - 8 gauss/box
radius 7.156 cm.

A.

B. Field - 8 gauss/box
radius 7.5 cm.

time scale - 2 usec./box
A. Primary current 145 amps./box

Figure V - 3 Continued

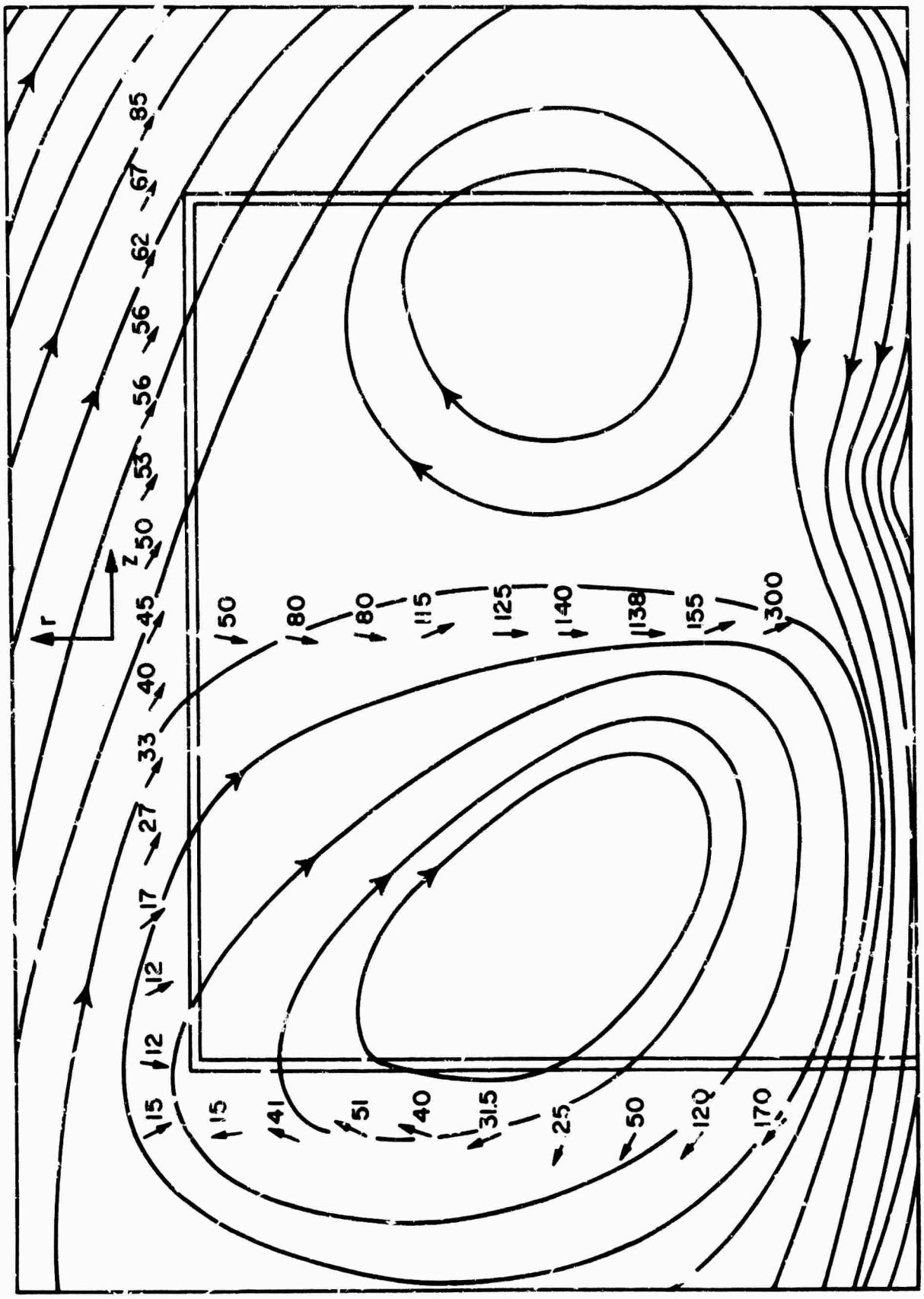

Magnetic Flux Plot - Time One Microsecond

Figure V-4

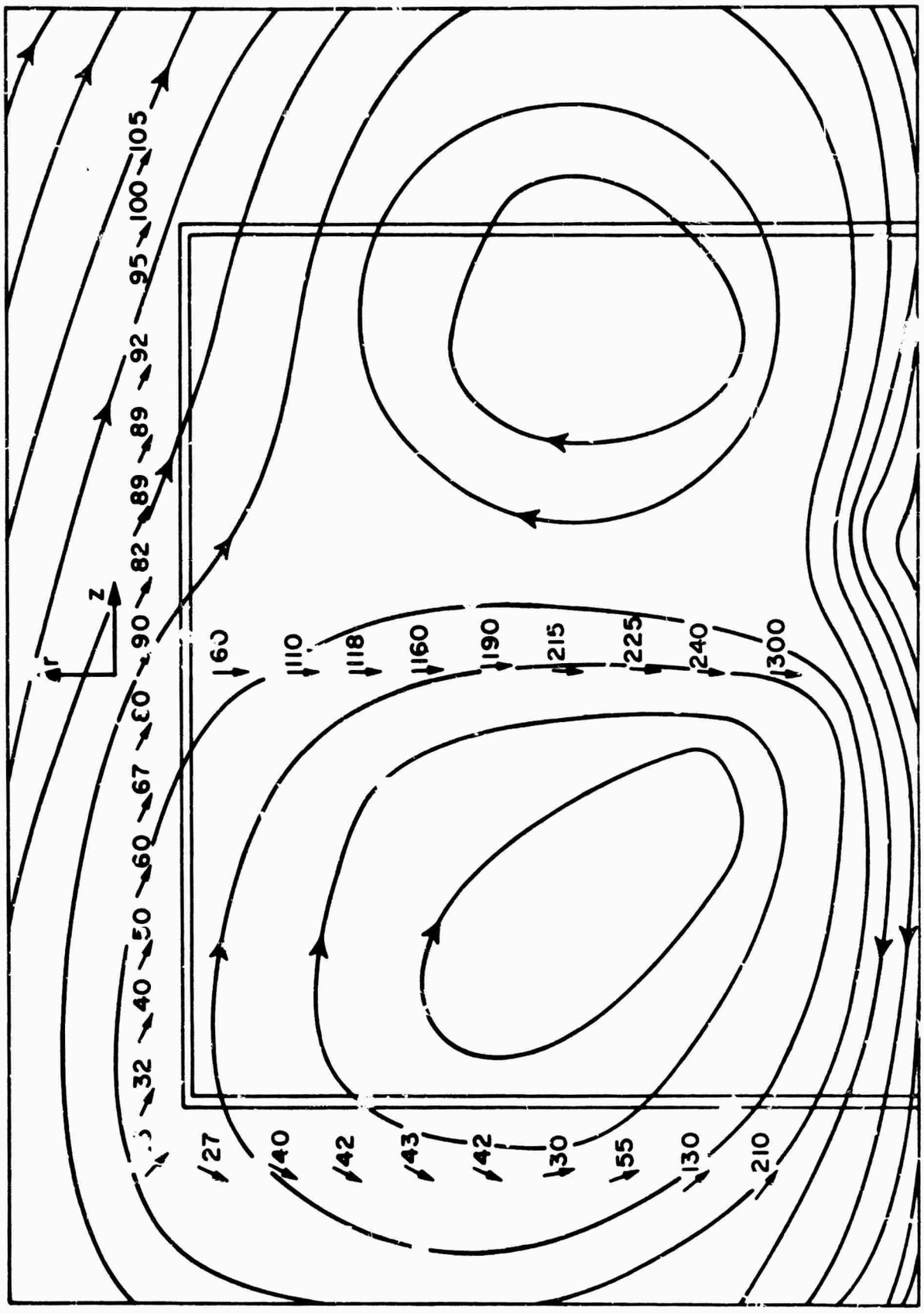

Magnetic Flux Plot - Time Two Microseconds

Figure V-5

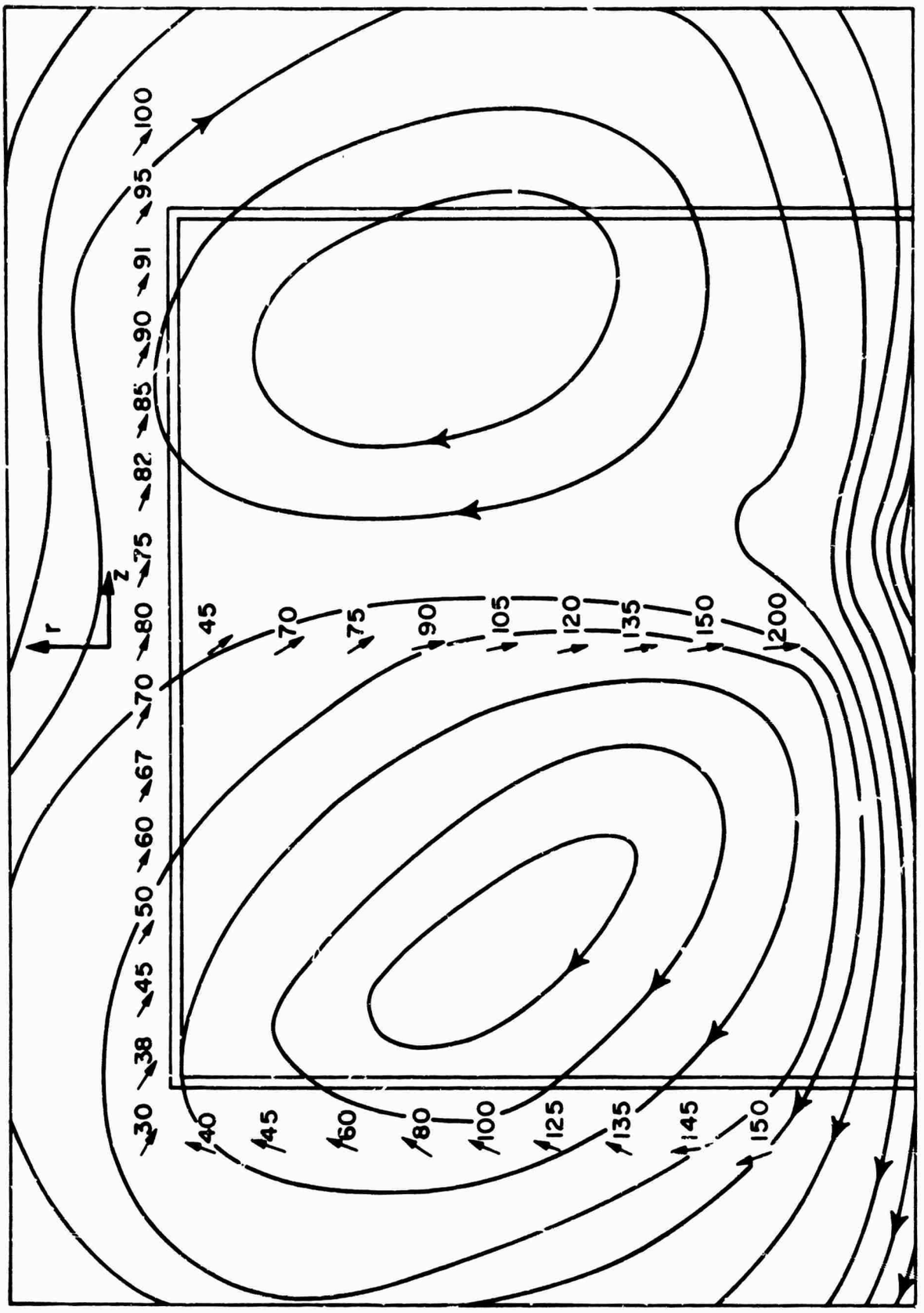

Magnetic Flux Plot - Time Three Microseconds

Figure V-6

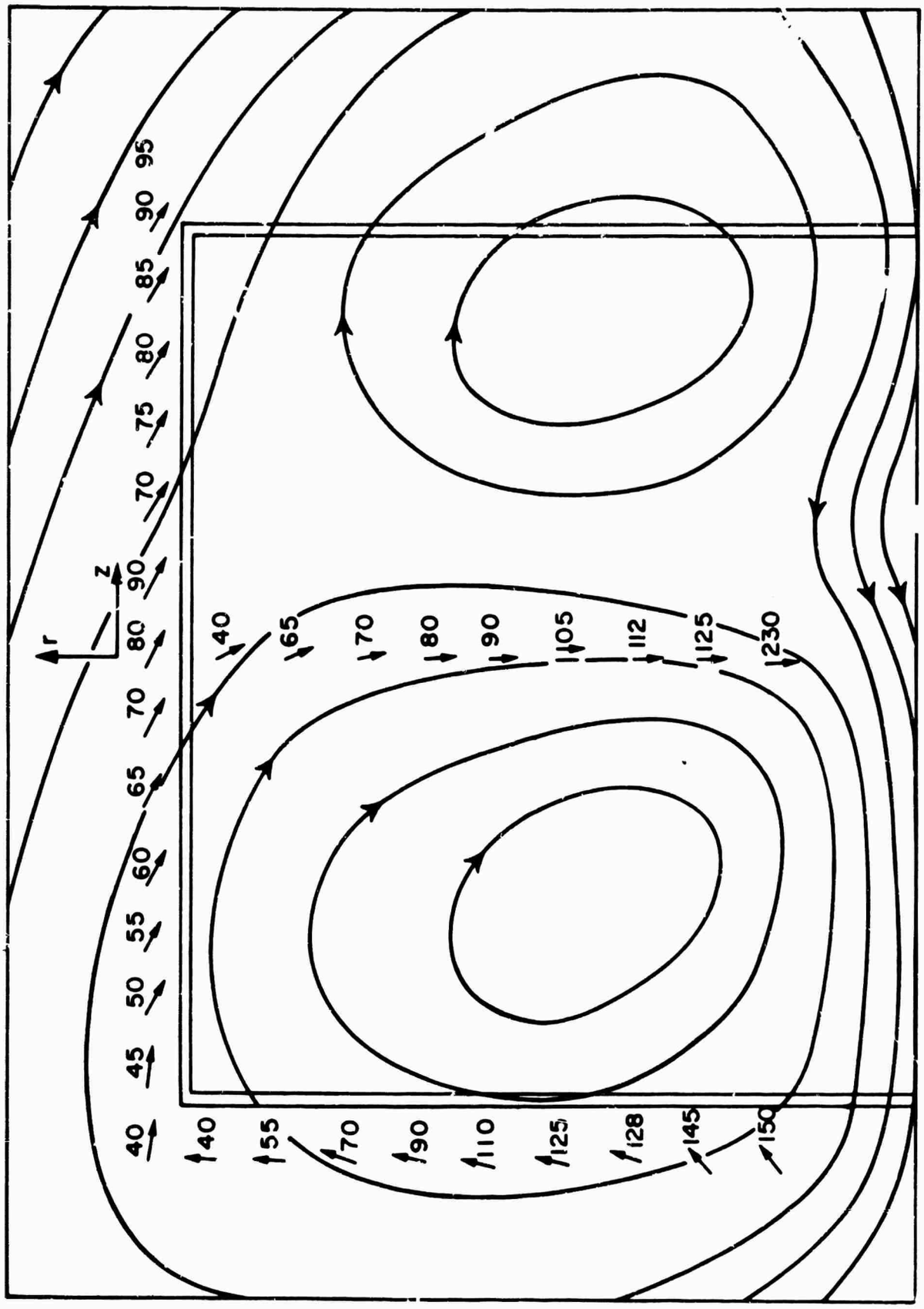

Magnetic Flux Plot - Time Four Microseconds

Figure V-7

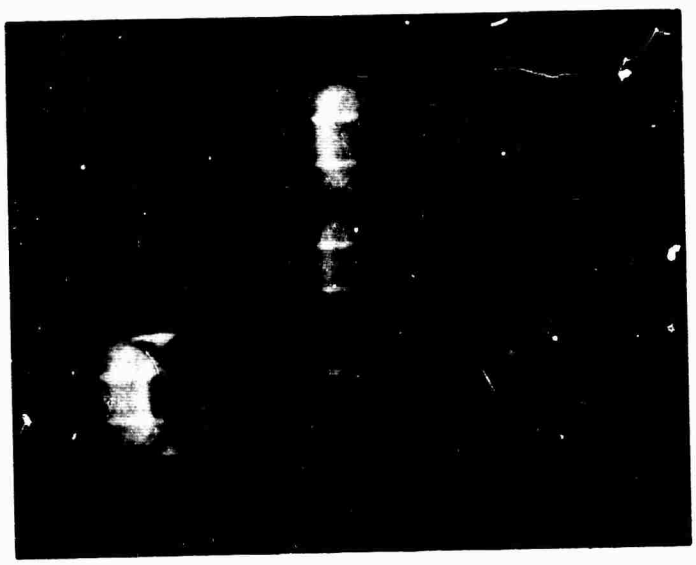

Time In Microseconds

0.0	1.5	3.0
0.5	2.0	3.5
1.0	2.5	4.0

Framing Photograph of Radial Motion

Figure V - 8

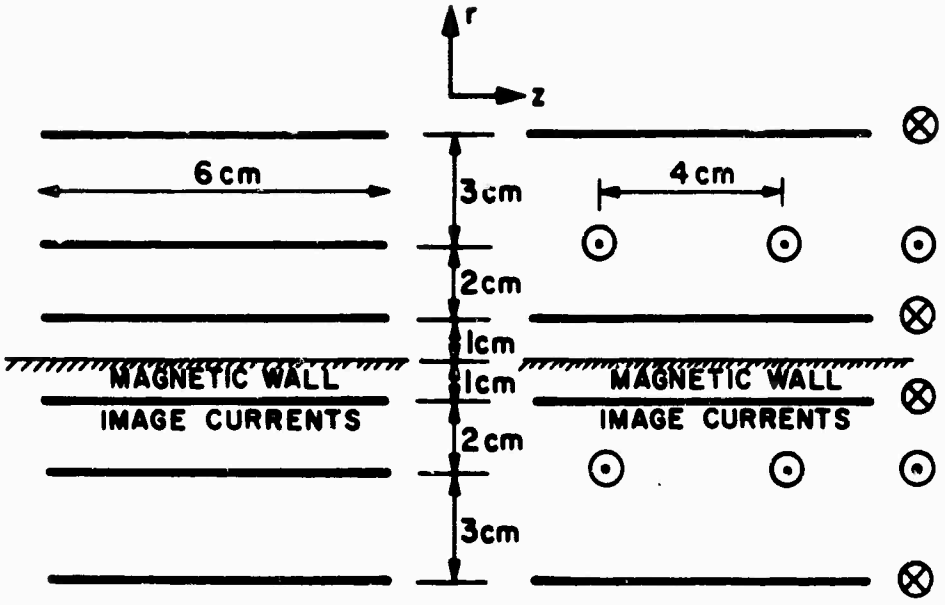

a. SHEET MODEL

b. DUAL-RING MODEL

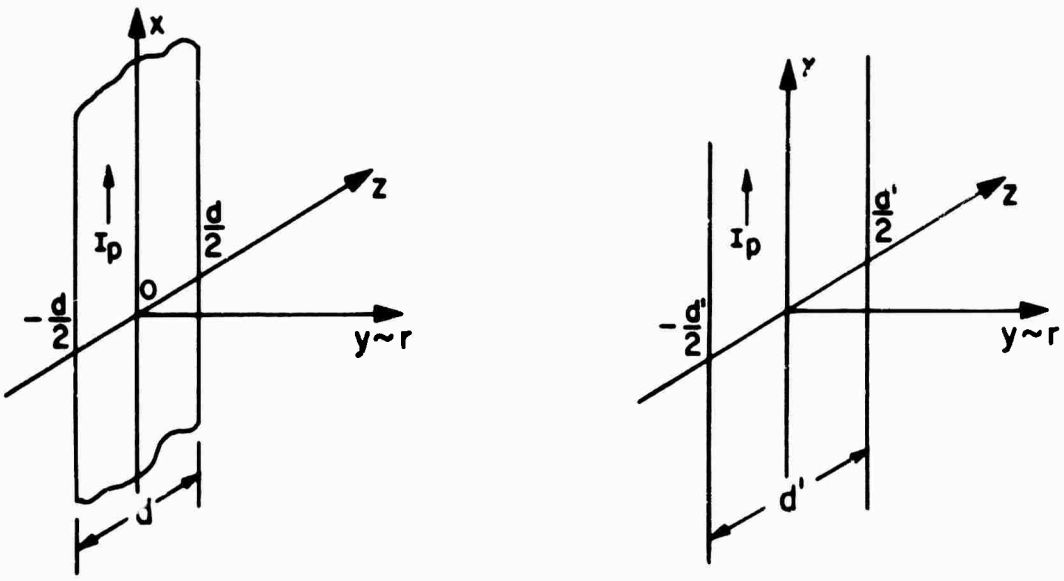

Theoretical Models of Current Distribution

Figure V-9

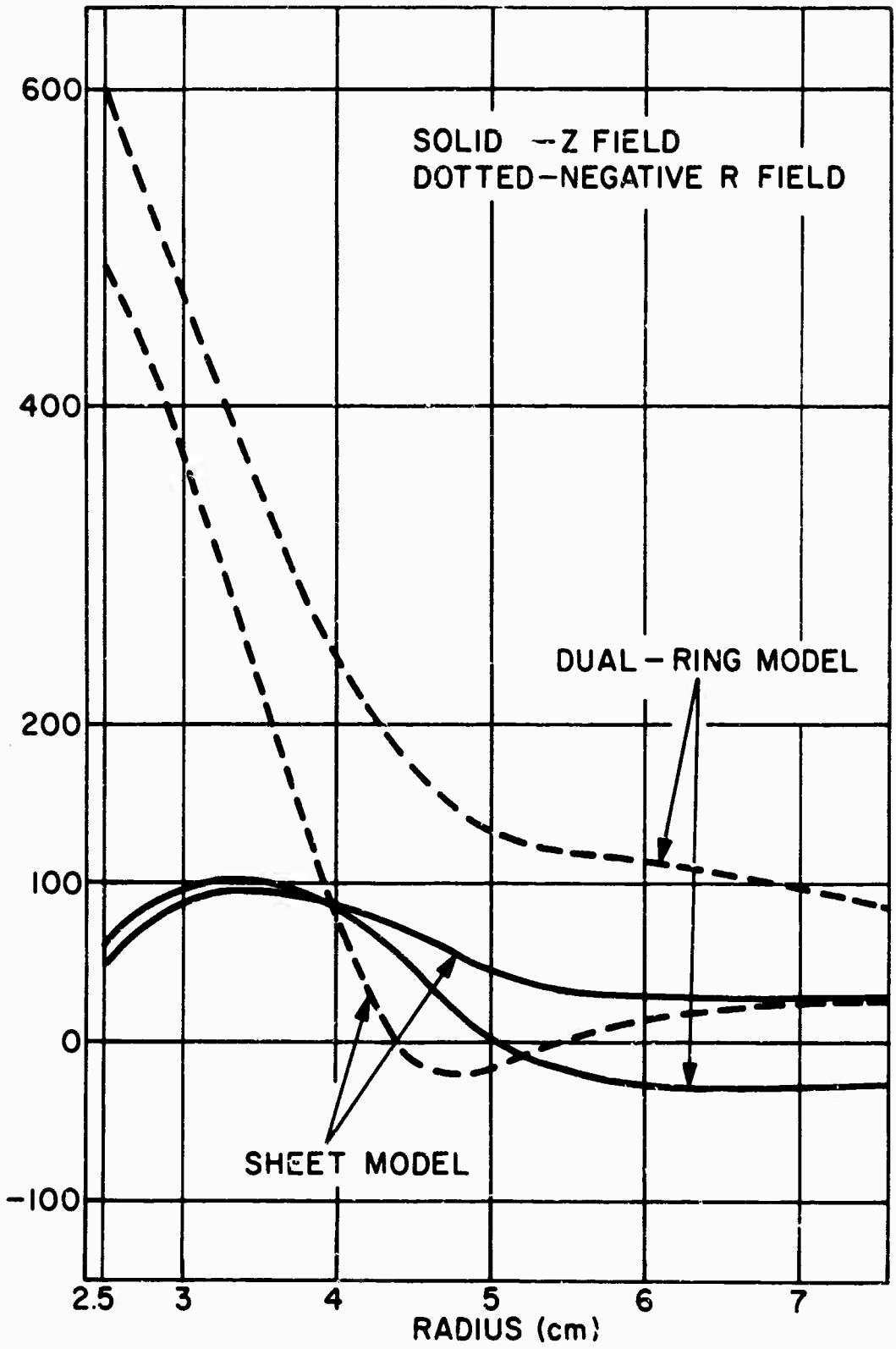

Model Fields (Side Wall)

Figure V-10

Model Fields for B_z (Center of Discharge)

Figure V-11

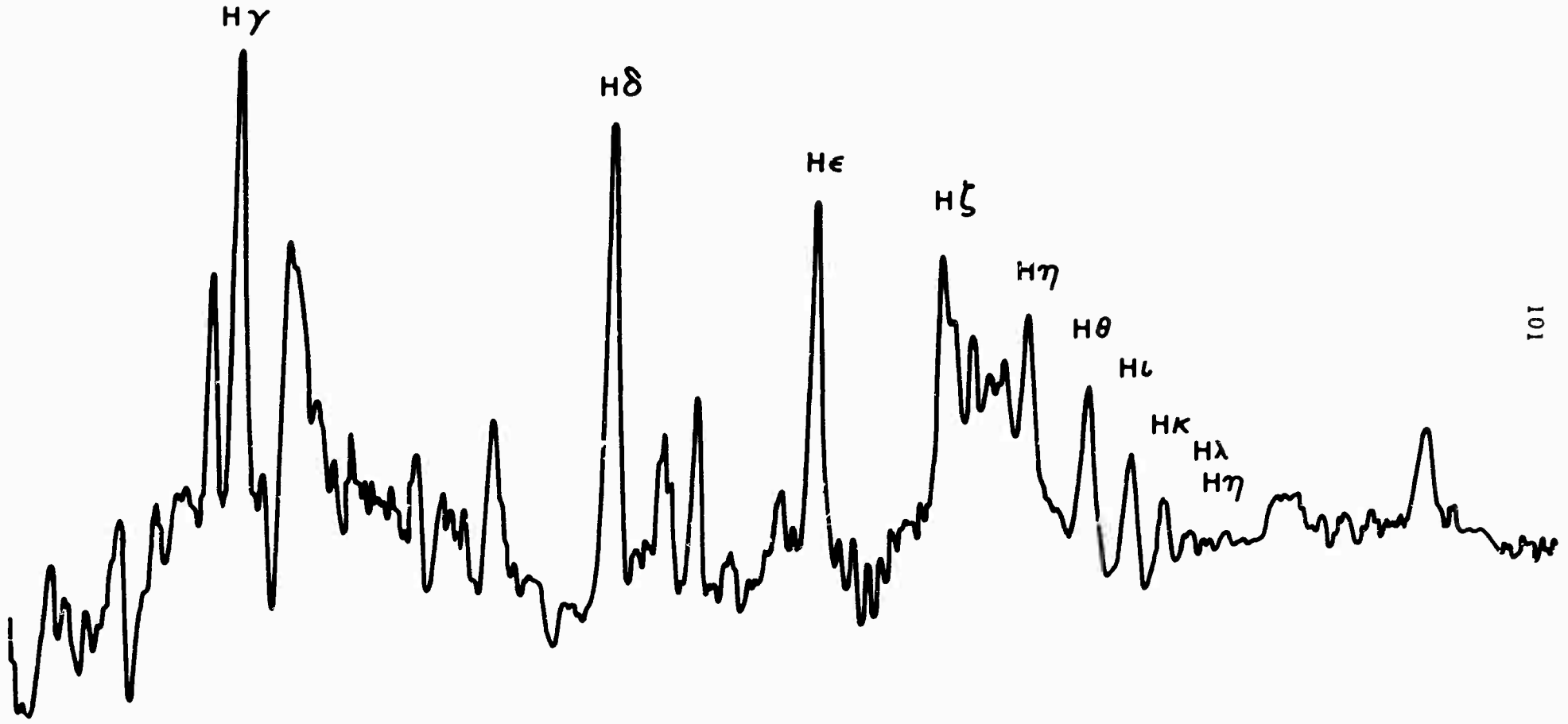

Microdensitomer Scan of Film
Figure V-12

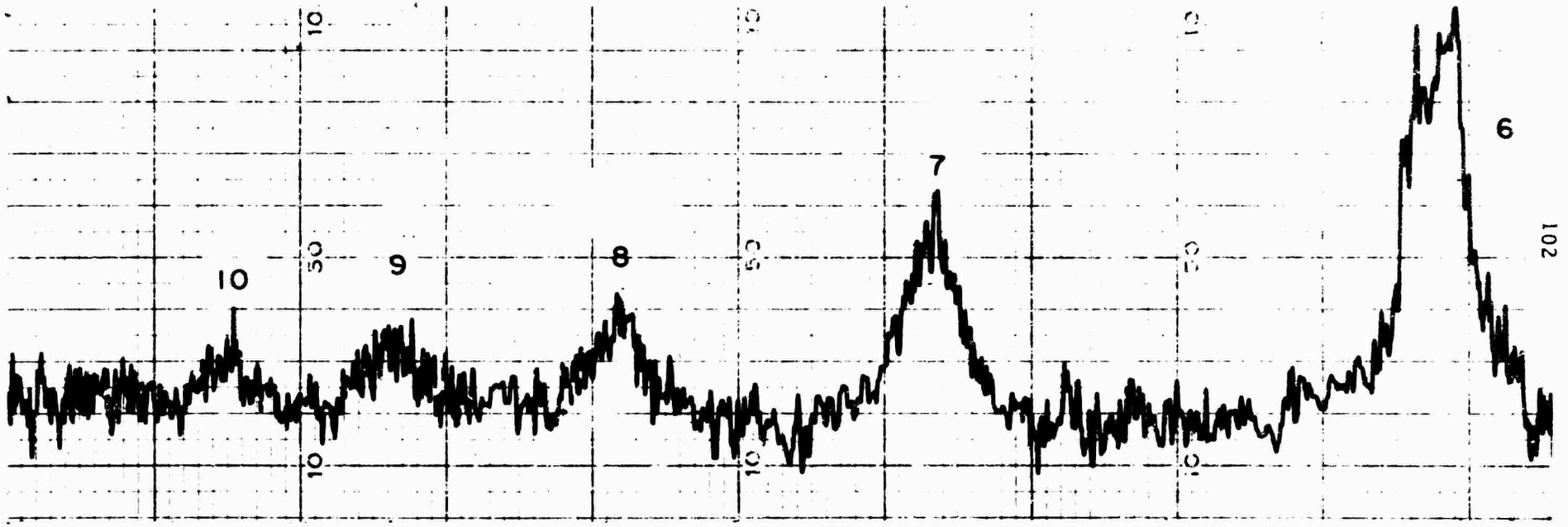

MONOCHROMATER SCAN TIME — 4 MICRO SEC.

Figure V-13

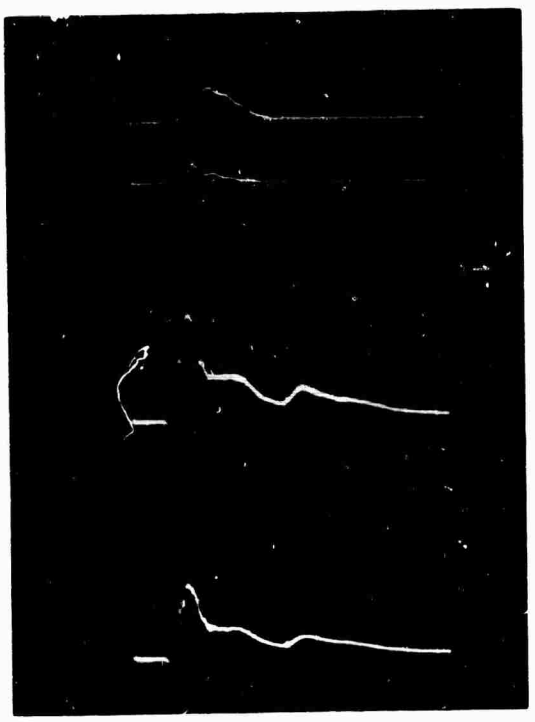

current - 4KA/box
voltage - 1KV/box
time - 1 usec./box

narrow slit
ampl. 0.5V/box
time 2 usec./box

wide slit
ampl. 5V/box
time 2 usec./box

Photomultiplier Tube Output Voltages

Figure V-14

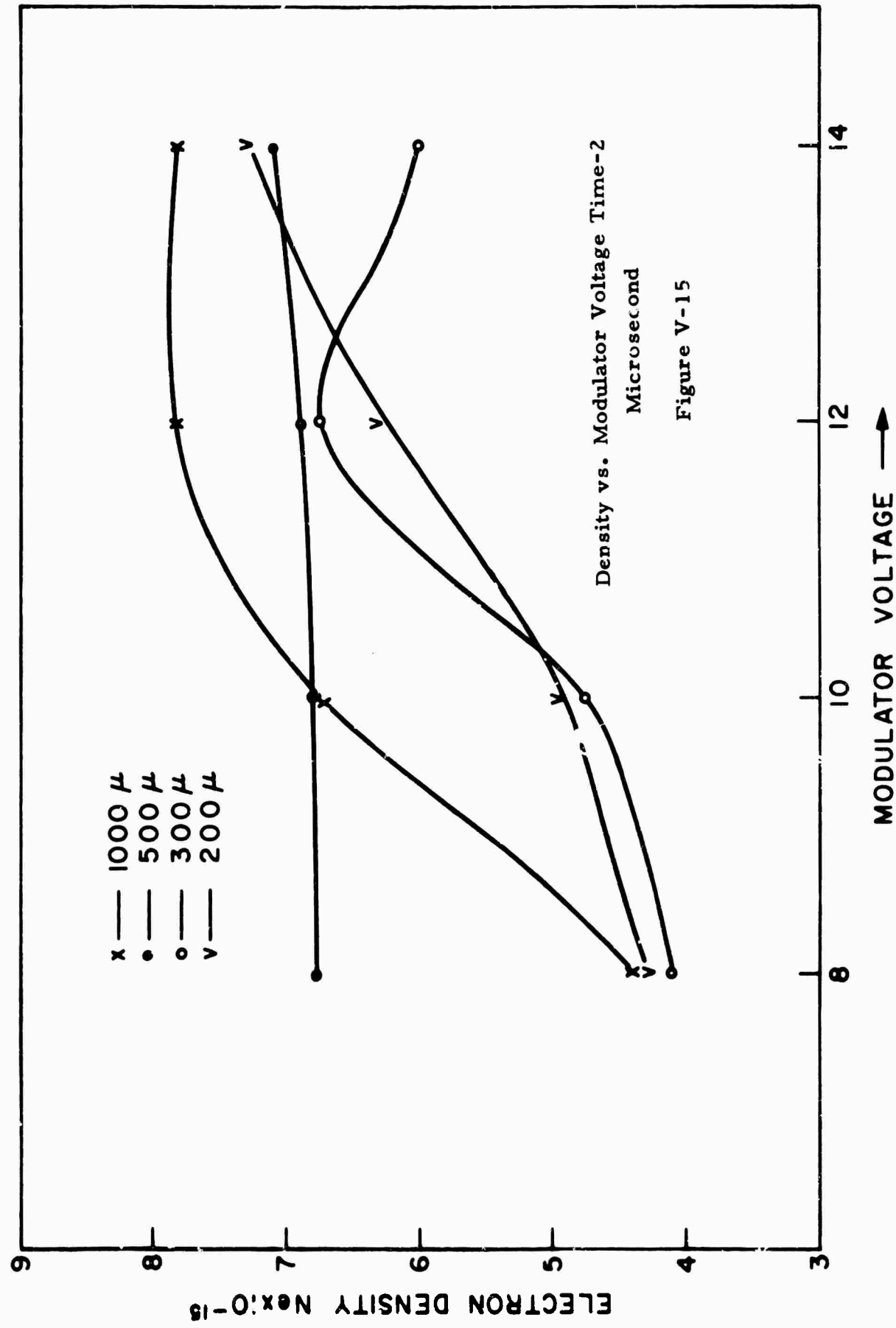

Density vs. Modulator Voltage Time-2 Microsecond

Figure V-15

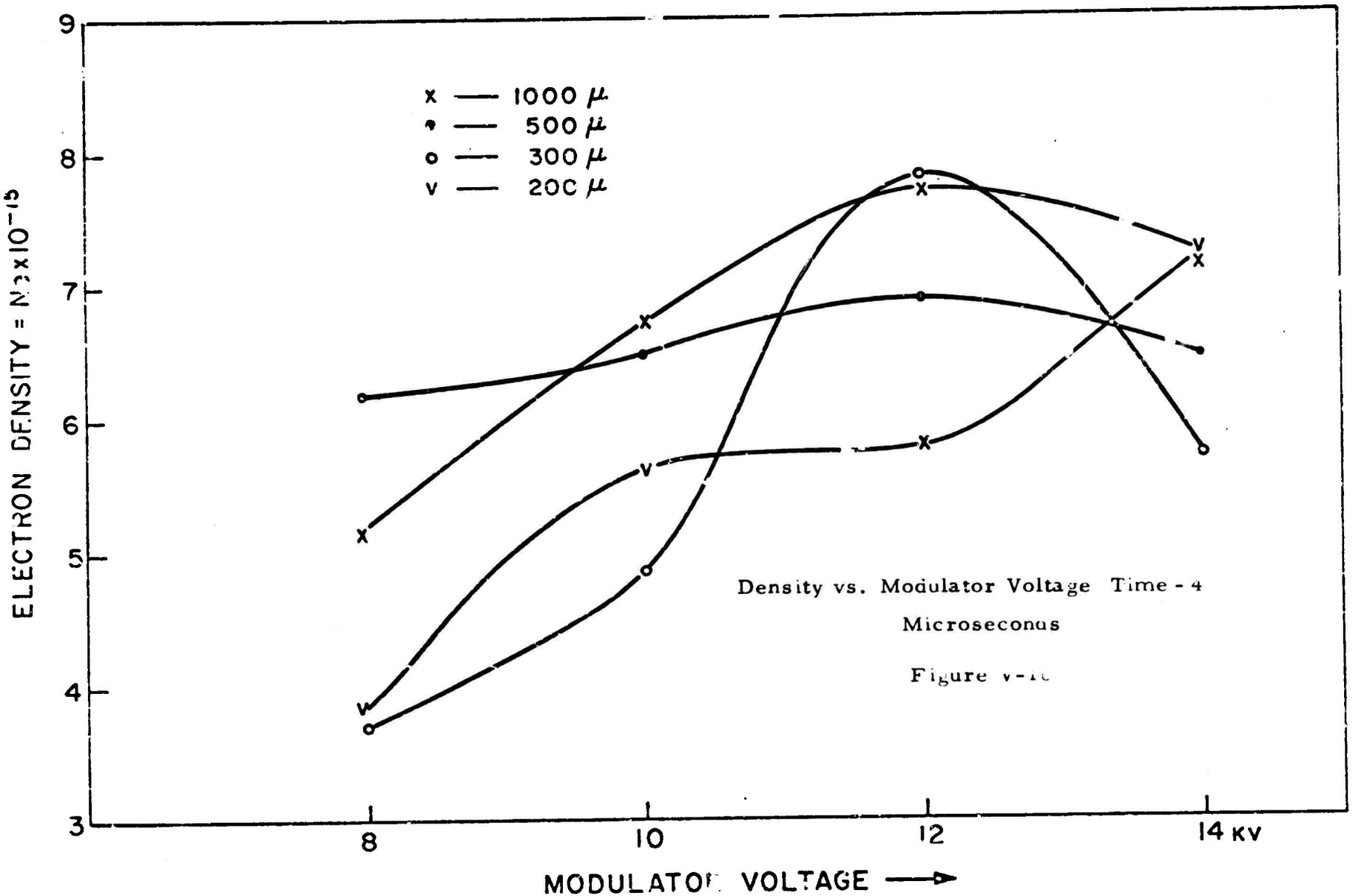

Density vs. Modulator Voltage Time - 4 Microseconds

Figure V-1C

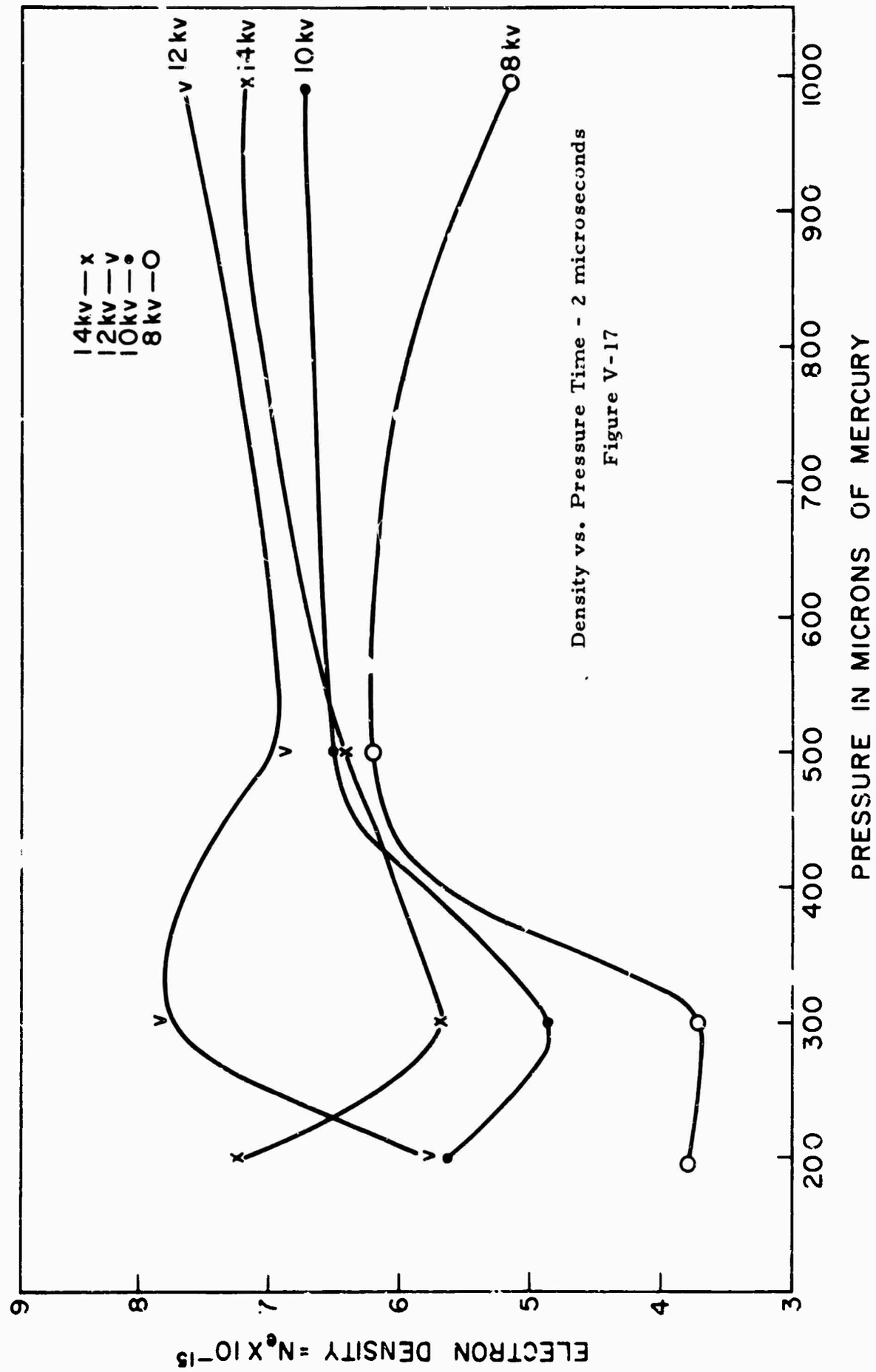

Density vs. Pressure Time - 2 microseconds
Figure V-17

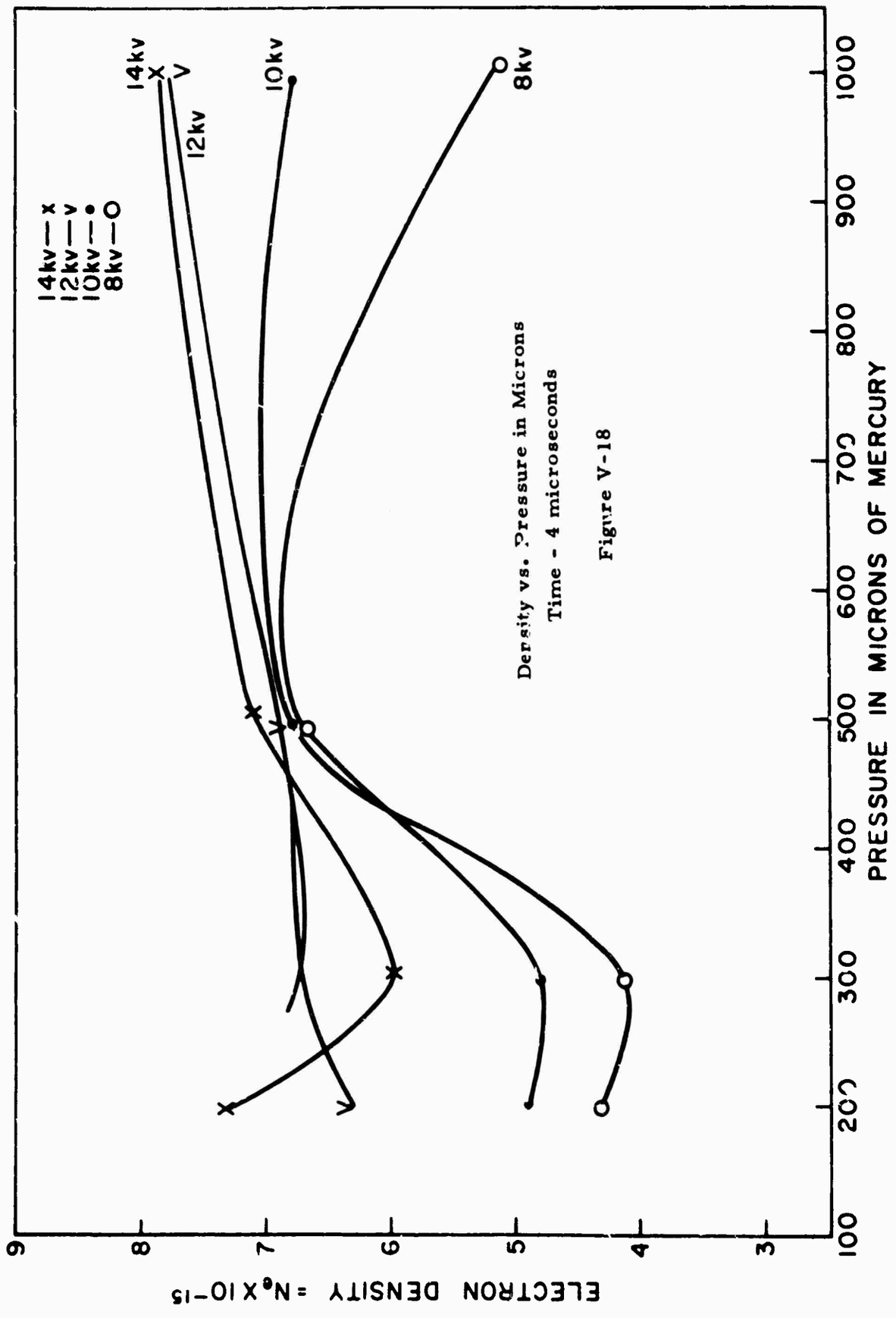

Density vs. Pressure in Microns
Time - 4 microseconds

Figure V-18

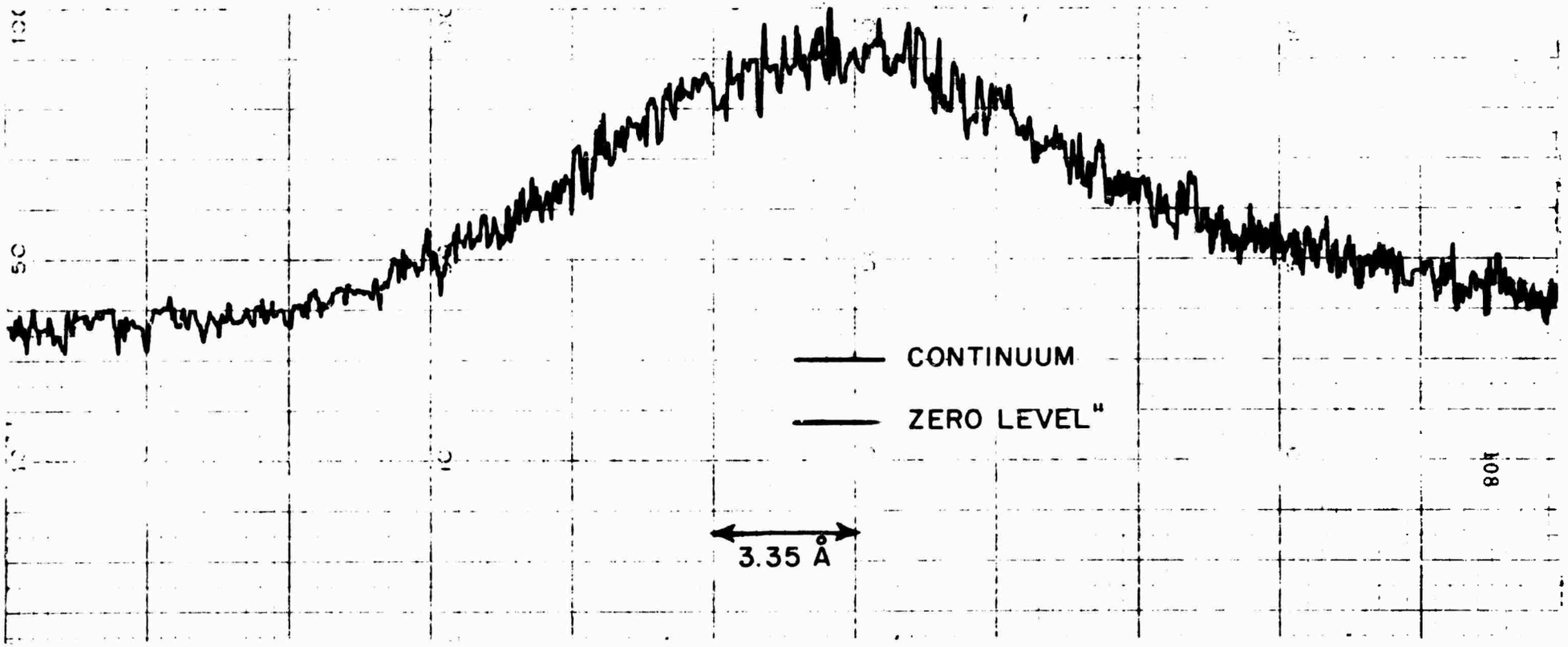

MONOCHROMATER SCAN OF H_γ AT TIME = 2 MICRO SEC

Figure V-19

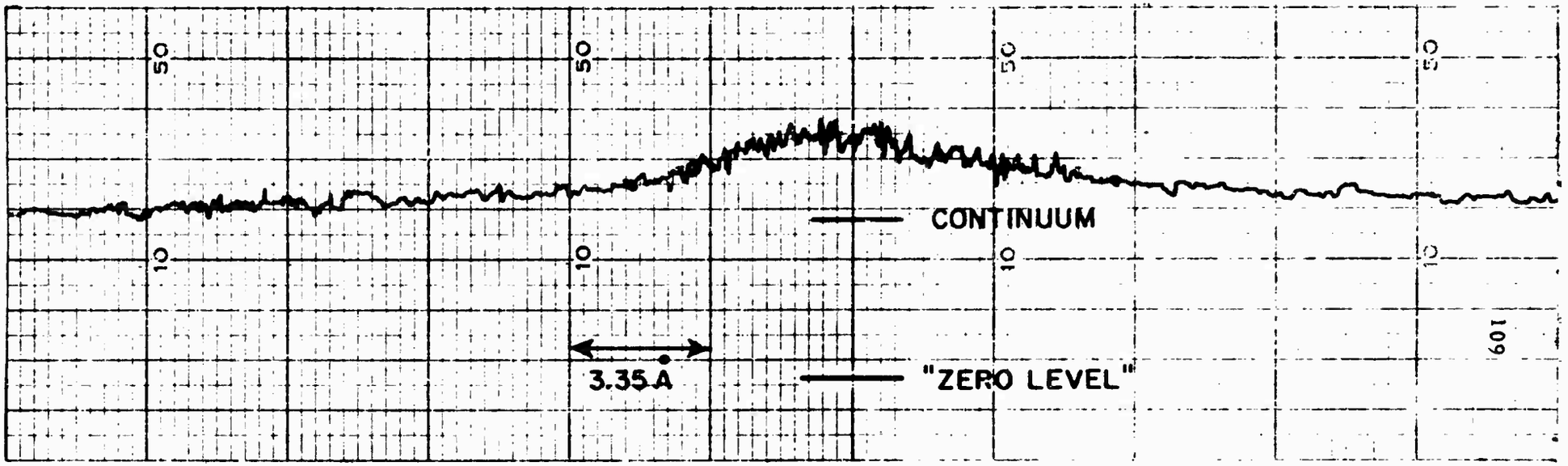

MONOCHROMATER SCAN OF H_β TIME = 2 MICRO SEC.

Figure V-20

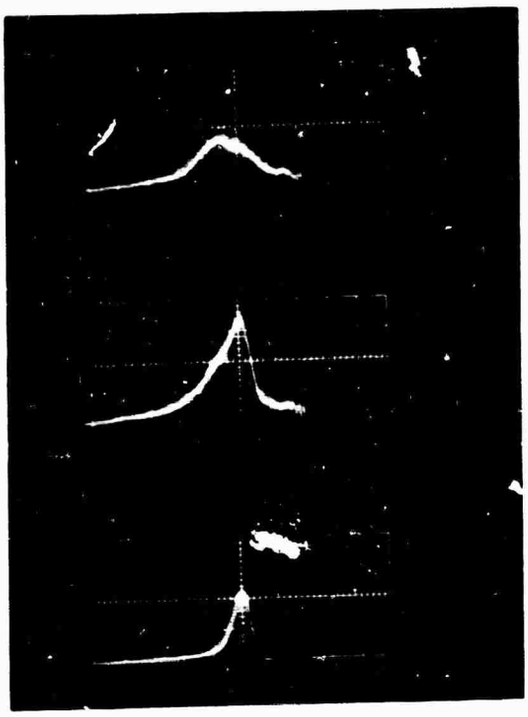

H_β light from plasma

1.6 Å band

both plasma and strobe light radiating

strobe light output -

1.6 Å band centered at H_β

Measurement of Self Absorption

Figure V - 21

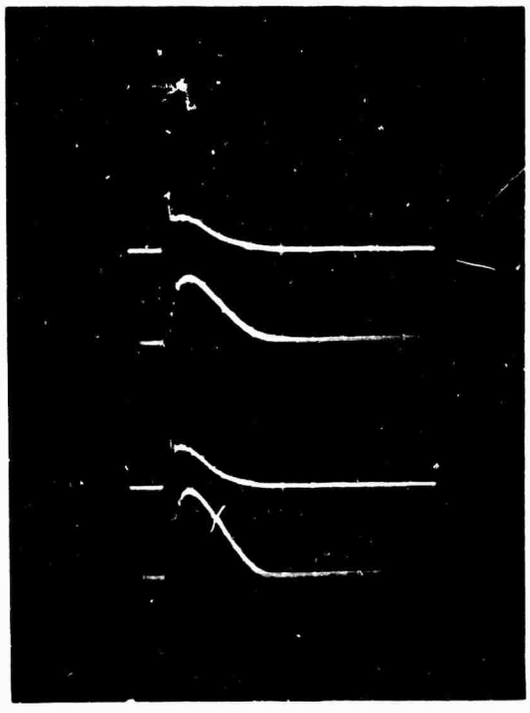

modulator voltage

8 KV

10 KV

Top Trace - core voltage - 200 V/cm

Bottom Trace - plasma current - 1250 A/cm

Time scale - 2 microseconds/cm

Voltage - Current Relationship

Figure V - 22

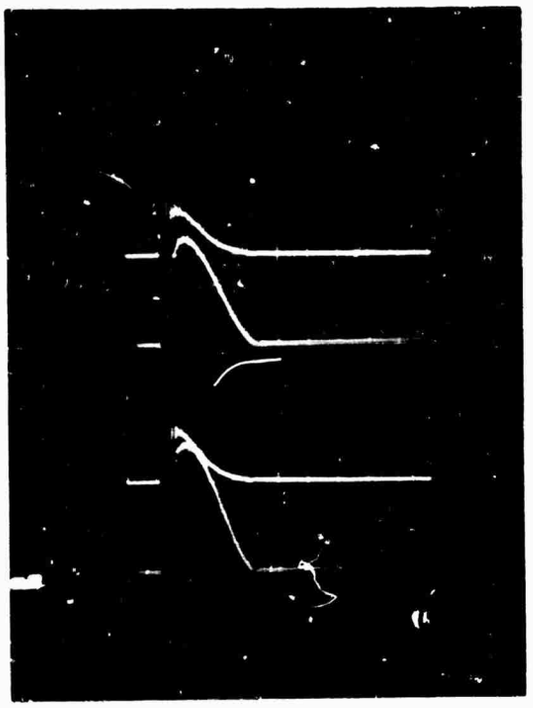

modulator voltage

12 KV

14 KV

Top Trace - core voltage - 200V/cm.

Bottom Trace - plasma current - 1250A/cm.

Time scale - 2 microseconds/cm.

Figure V-22 Continued

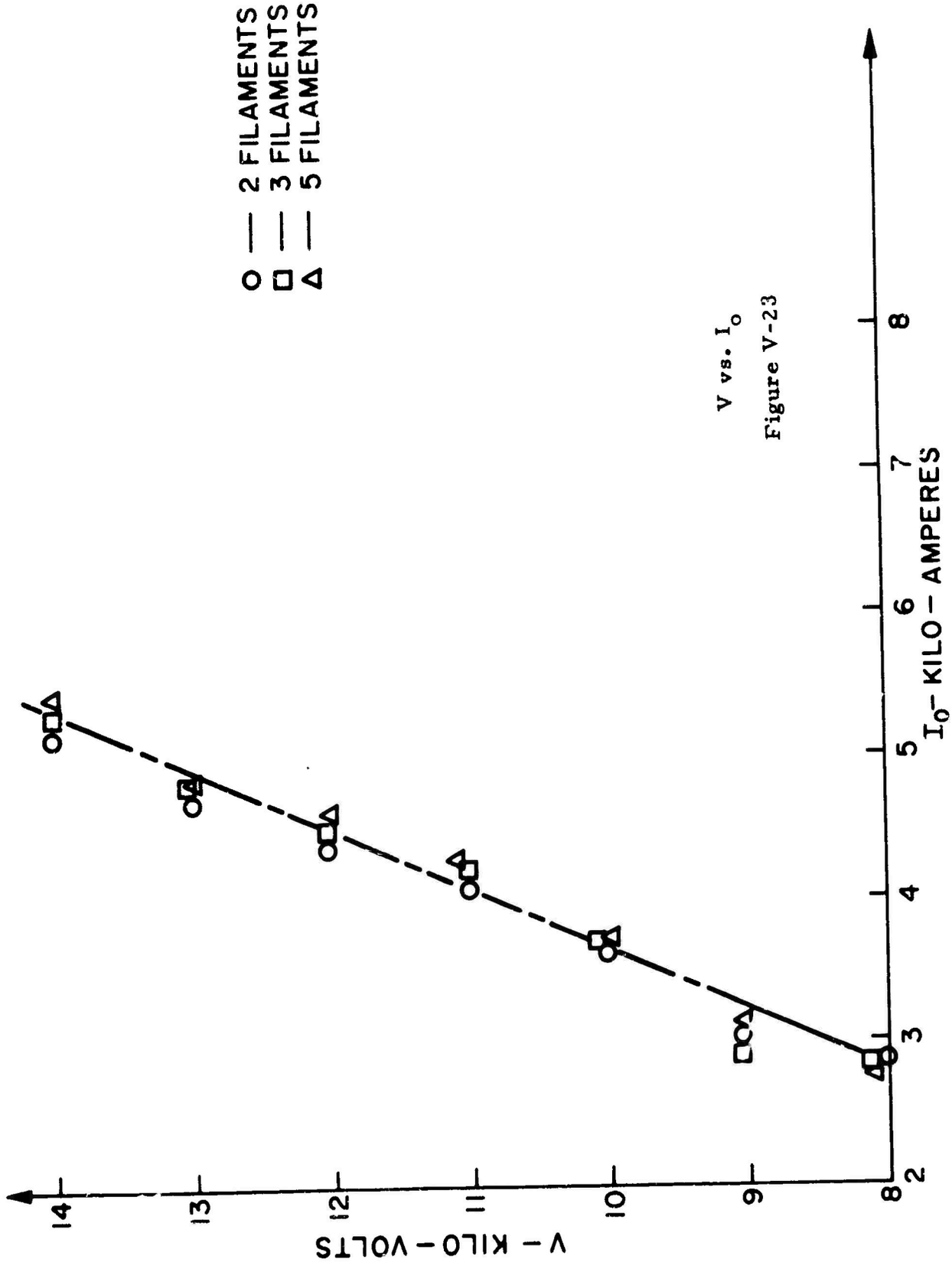

V vs. I_o

Figure V-23

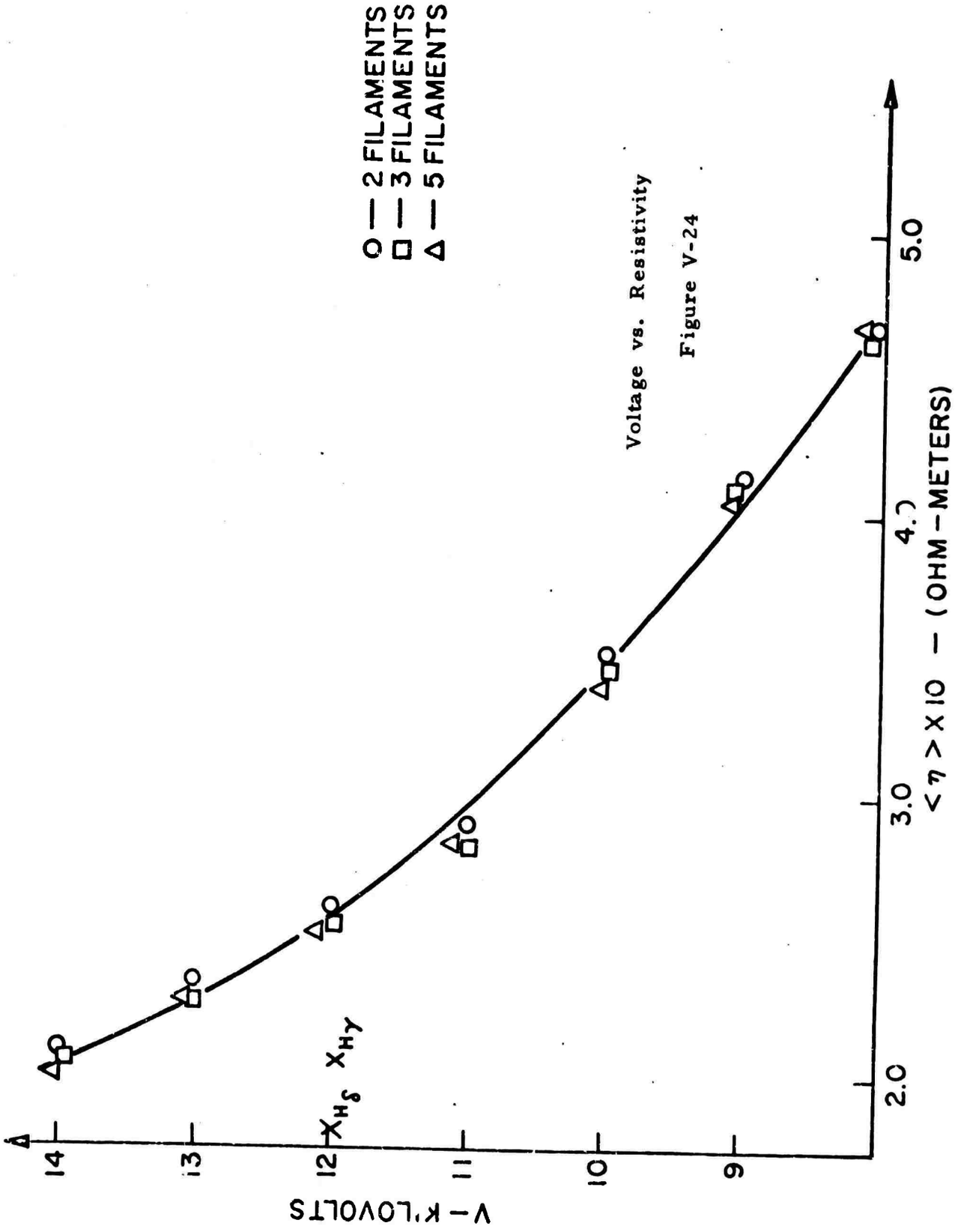

Voltage vs. Resistivity

Figure V-24

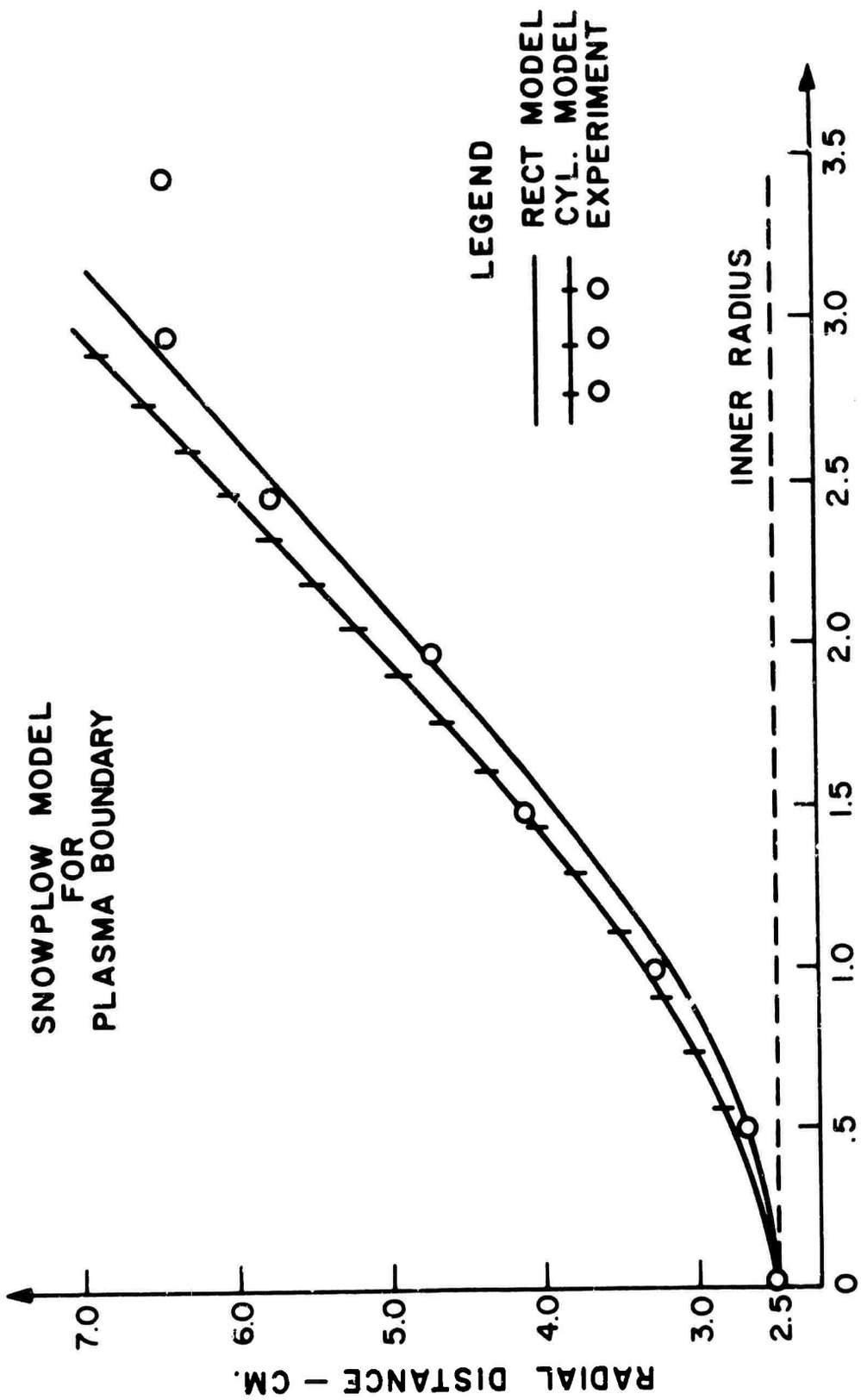
SNOWPLOW MODEL
FOR
PLASMA BOUNDARY
LEGEND
RECT MODEL
CYL. MODEL
EXPERIMENT
INNER RADIUS
RADIAL DISTANCE – CM.
TIME MICROSECONDS
7.0
6.0
5.0
4.0
3.0
2.5
0
.5
1.0
1.5
2.0
2.5
3.0
3.5

Figure V-25

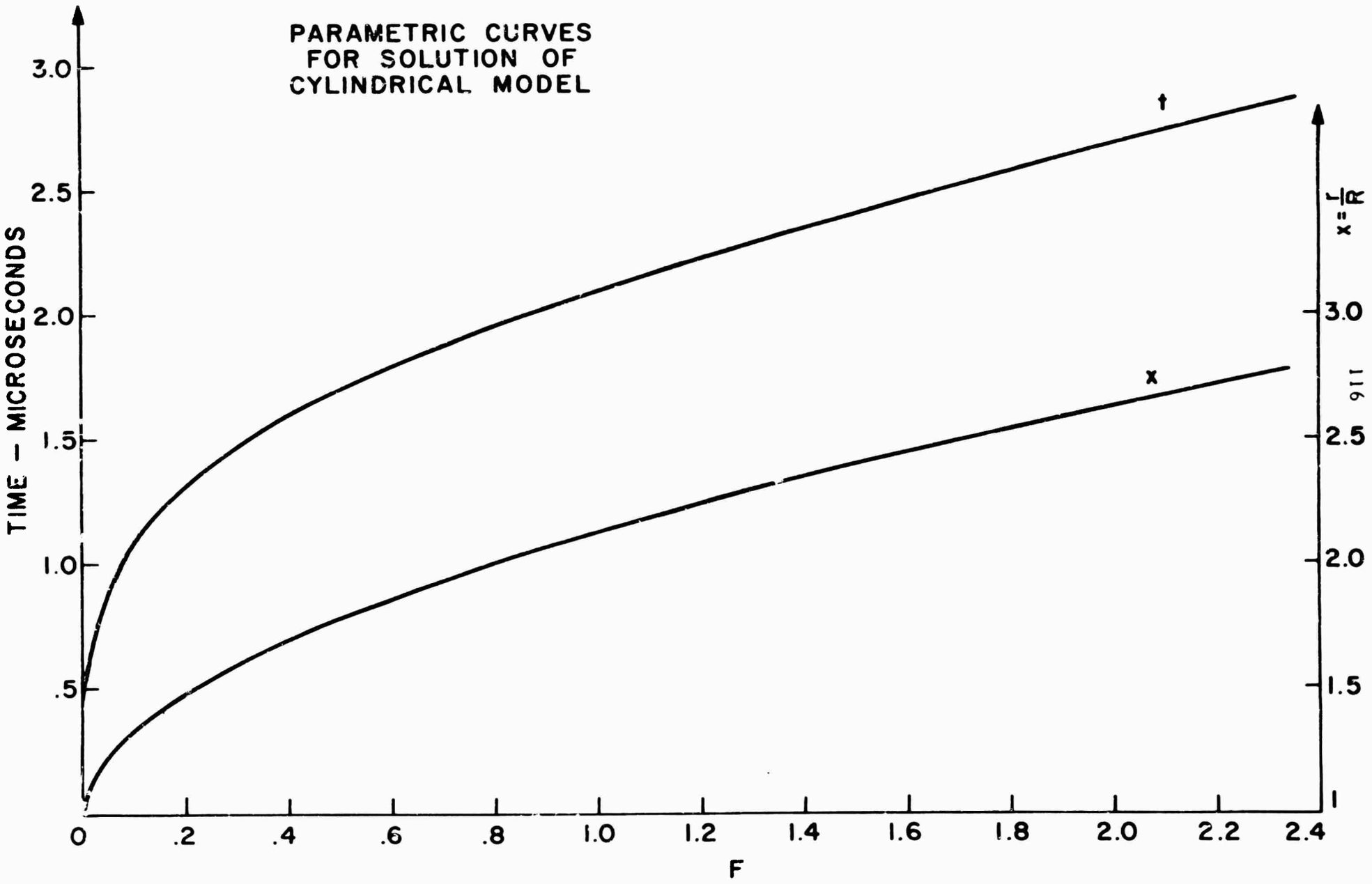
PARAMETRIC CURVES
FOR SOLUTION OF
CYLINDRICAL MODEL
TIME – MICROSECONDS
3.0
2.5
2.0
1.5
1.0
.5
t
x
x = r/R
3.0
2.5
2.0
1.5
1
0
.2
.4
.6
.8
1.0
1.2
1.4
1.6
1.8
2.0
2.2
2.4
F
911

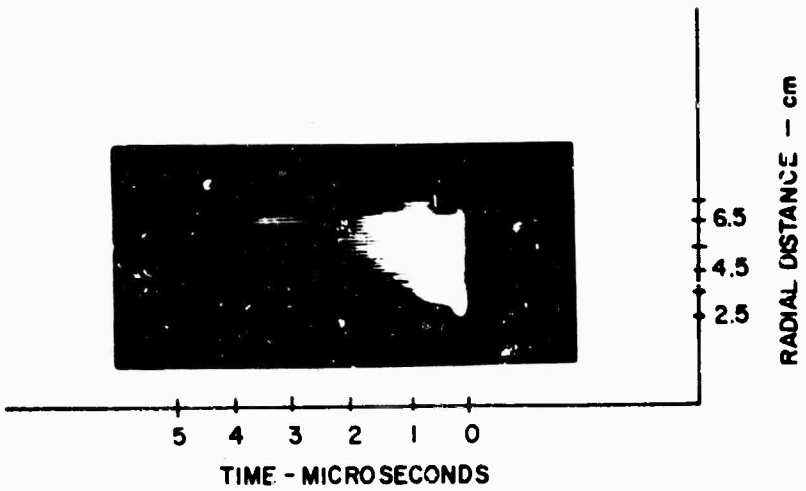

Streak Photograph of Radial Motion

Figure V - 27

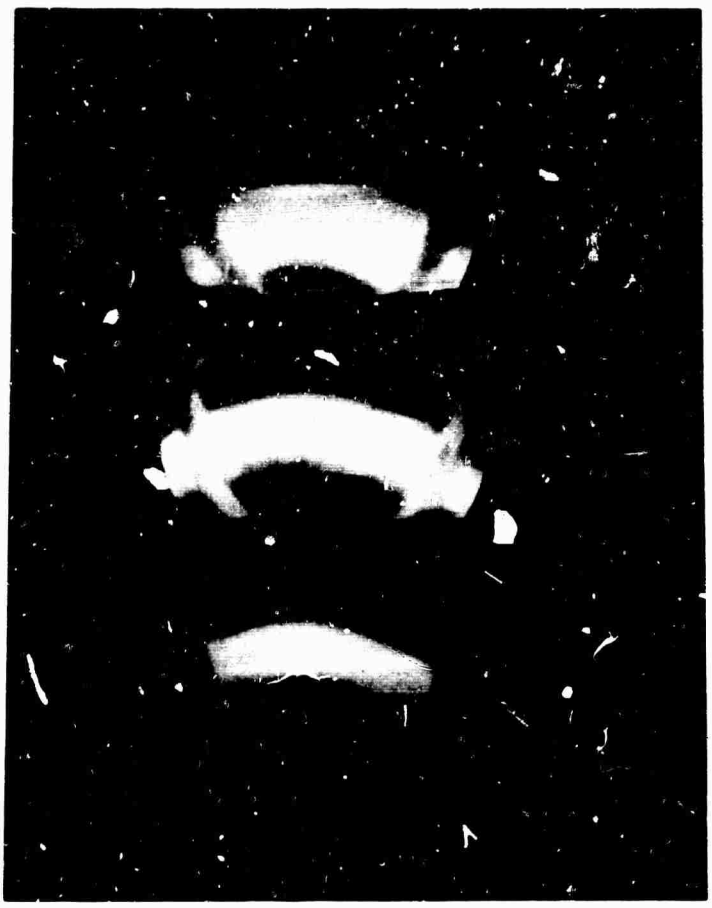

Framing Photographs of
Rayleigh-Taylor Instability

Figure V - 28

outer radius

inner radius

outer radius

inner radius

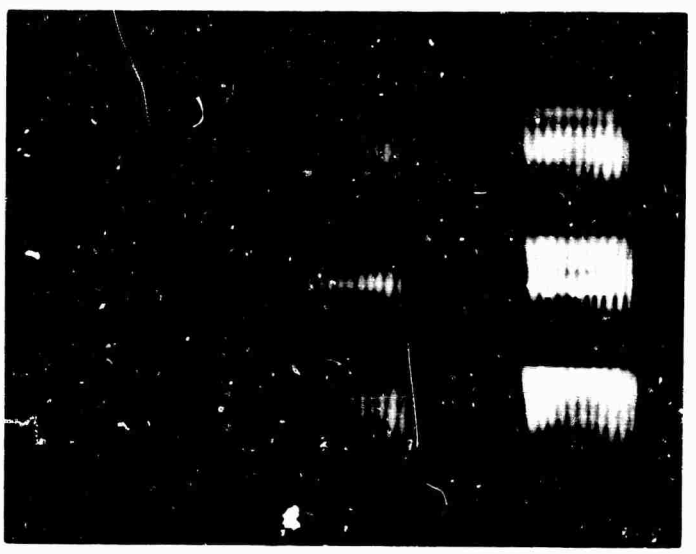

outer radius

inner radius

0.2	1.7	3.2
0.7	2.2	3.7
1.2	2.7	4.2

Time Sequence in Microseconds

Narrow Bottle with Outside Winding
(12KV with 500μ pressure)

Figure V-29

outer radius

inner radius

0.0	1.5	3.0
0.5	2.0	3.5
1.0	2.5	4.0

Time Sequence in Microseconds

Two Filament Configuration

Figure V - 30

outer radius

inner radius

0.0	1.5	3.0
0.5	2.0	3.5
1.0	2.5	4.0

Time Sequence in Microseconds

Three Filament Configuration

Figure V - 31

outer radius

inner radius

0.0	1.5	3.0
0.5	2.0	3.5
1.0	2.5	4.0

Time Sequence in Microseconds

Five Filament Configuration

Figure V - 32

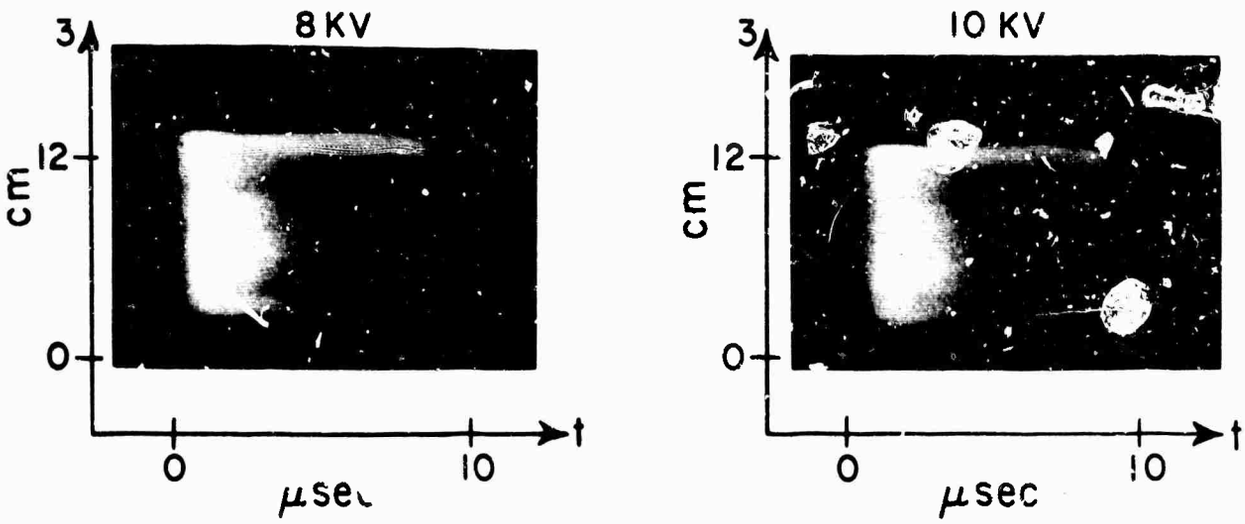

Two Filament Streak Photographs

Figure V - 33

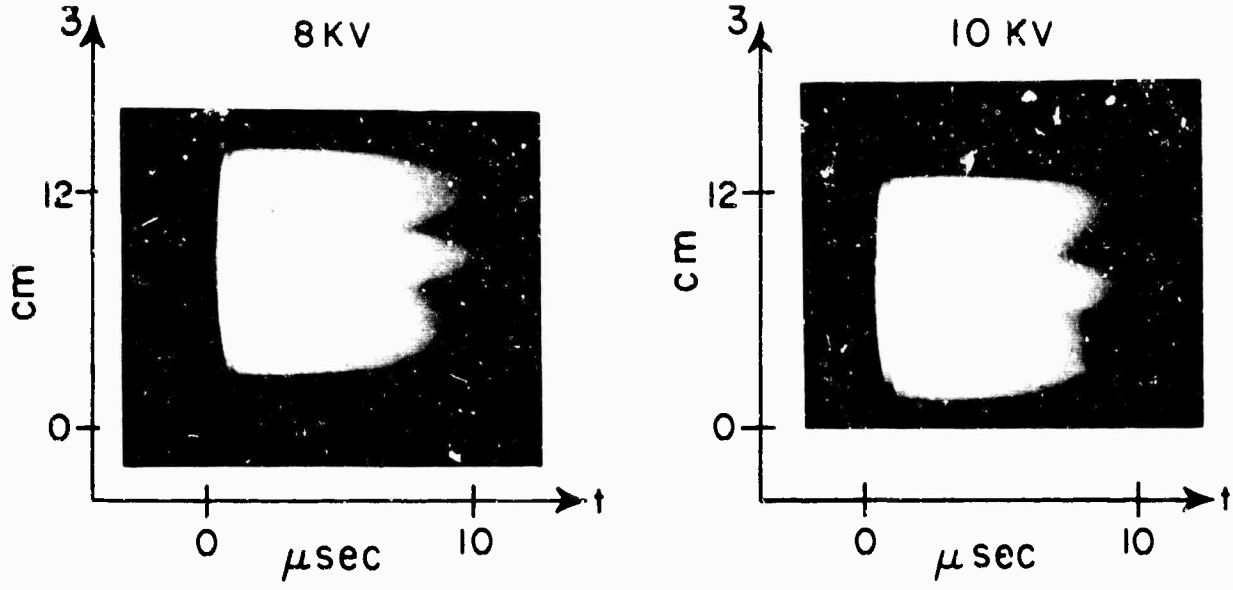

Three Filament Streak Photographs

Figure V - 34

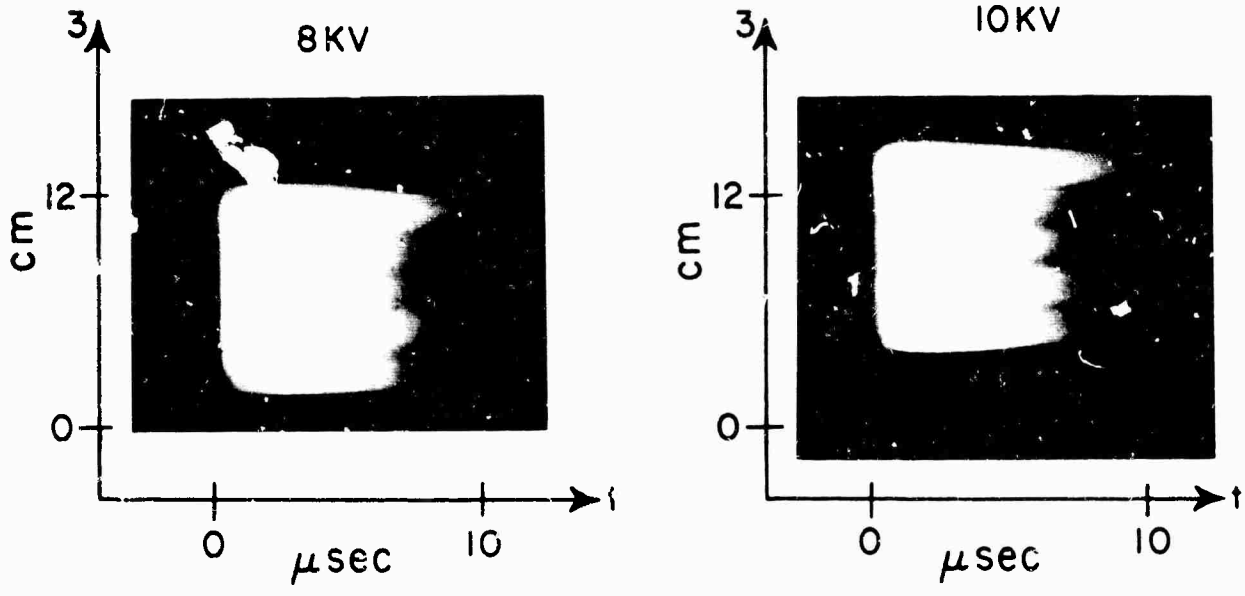

Five Filament Streak Photographs

Figure V - 35

Top Trace:
photodiode output

Bottom Trace:
primary current 150A/box

Time scale 2usec./box

Light Intensity via Photodiode Output

Figure V-36

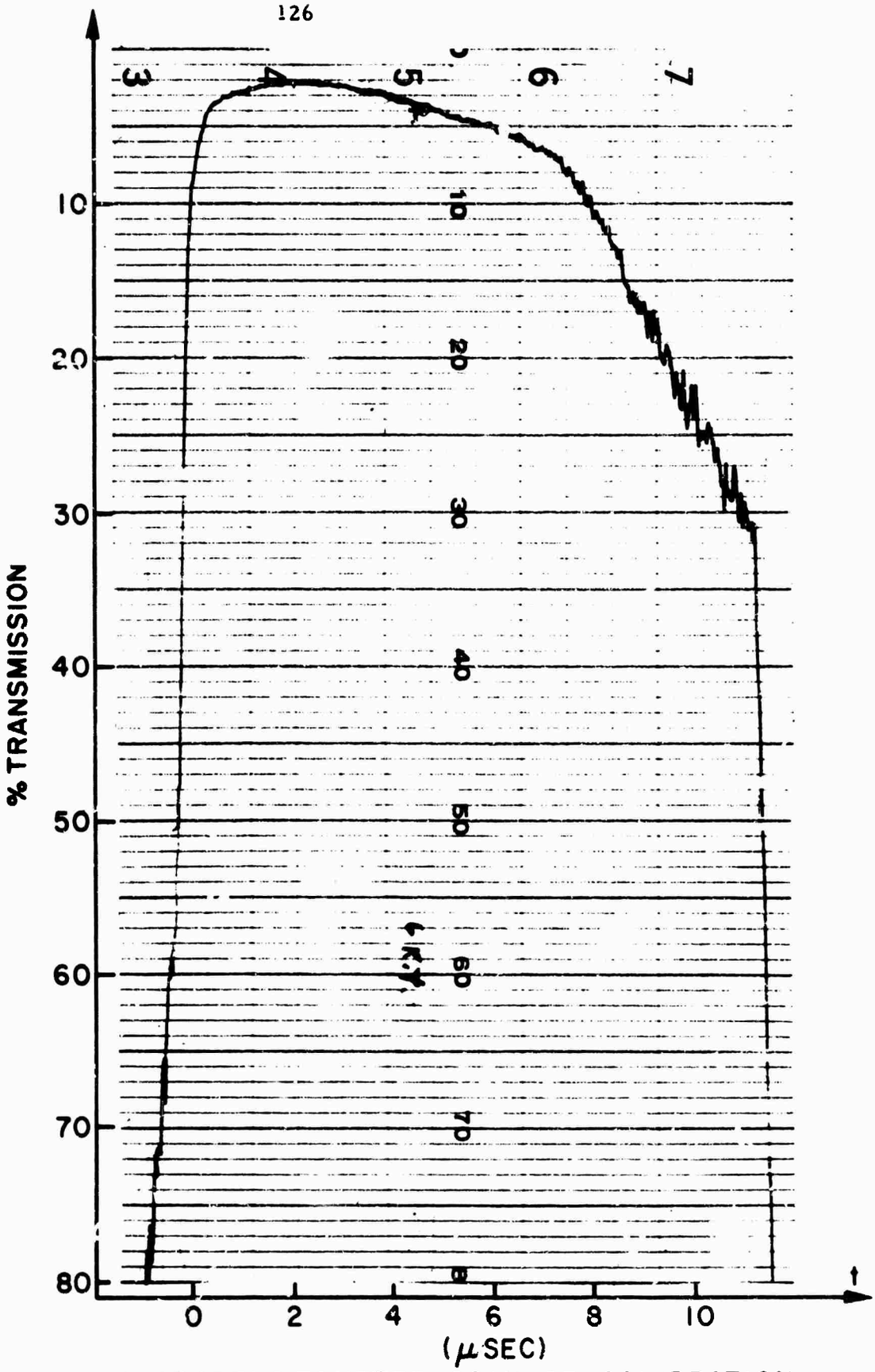

MICRODENSITOMETER SCAN OF CALIBRATION FOR FIVE FILAMENT PLASMA

Figure V-37

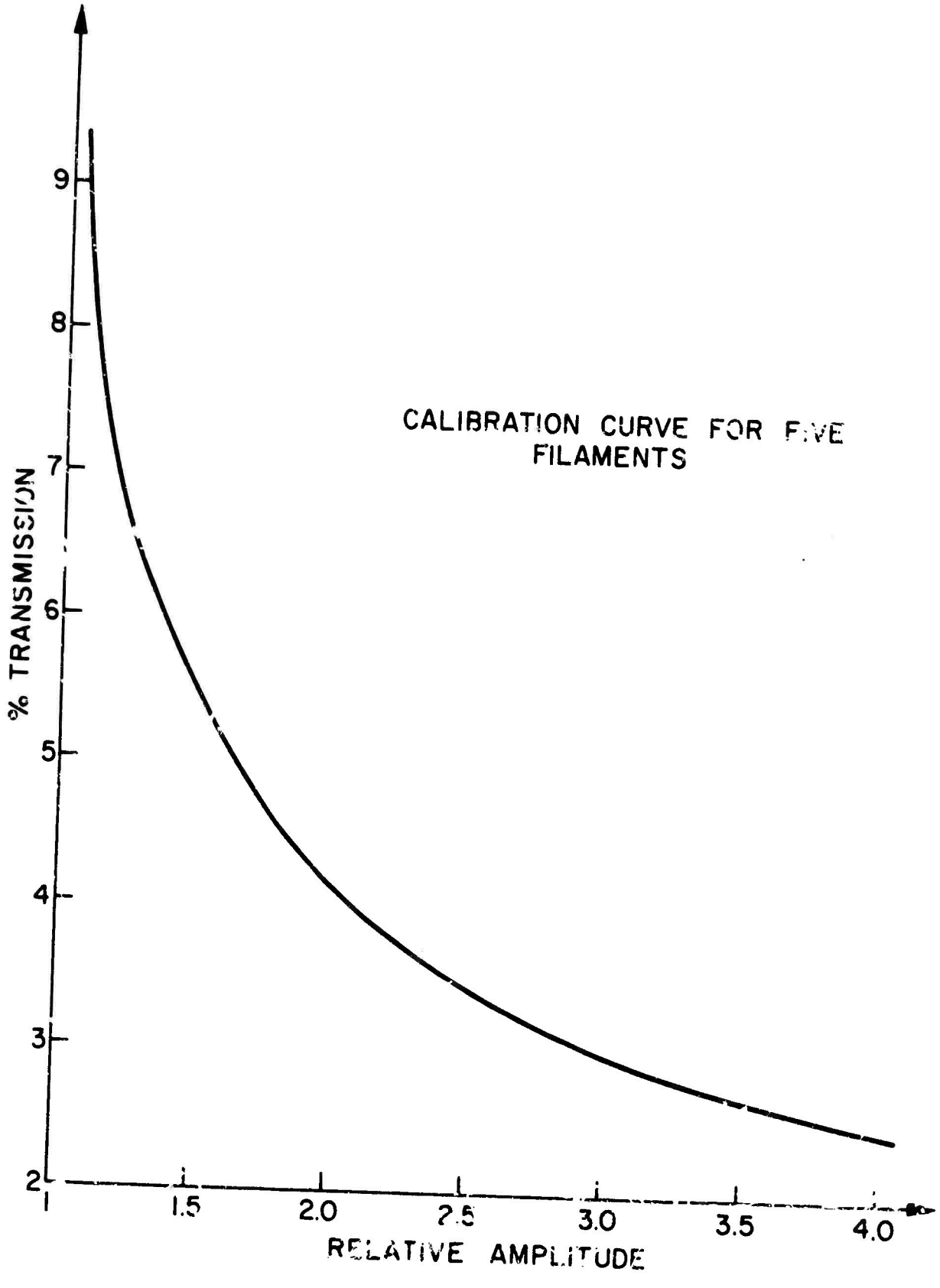
CALIBRATION CURVE FOR FIVE FILAMENTS
% TRANSMISSION
9
8
7
6
5
4
3
2
1.5
2.0
2.5
3.0
3.5
4.0
RELATIVE AMPLITUDE

Figure V-23

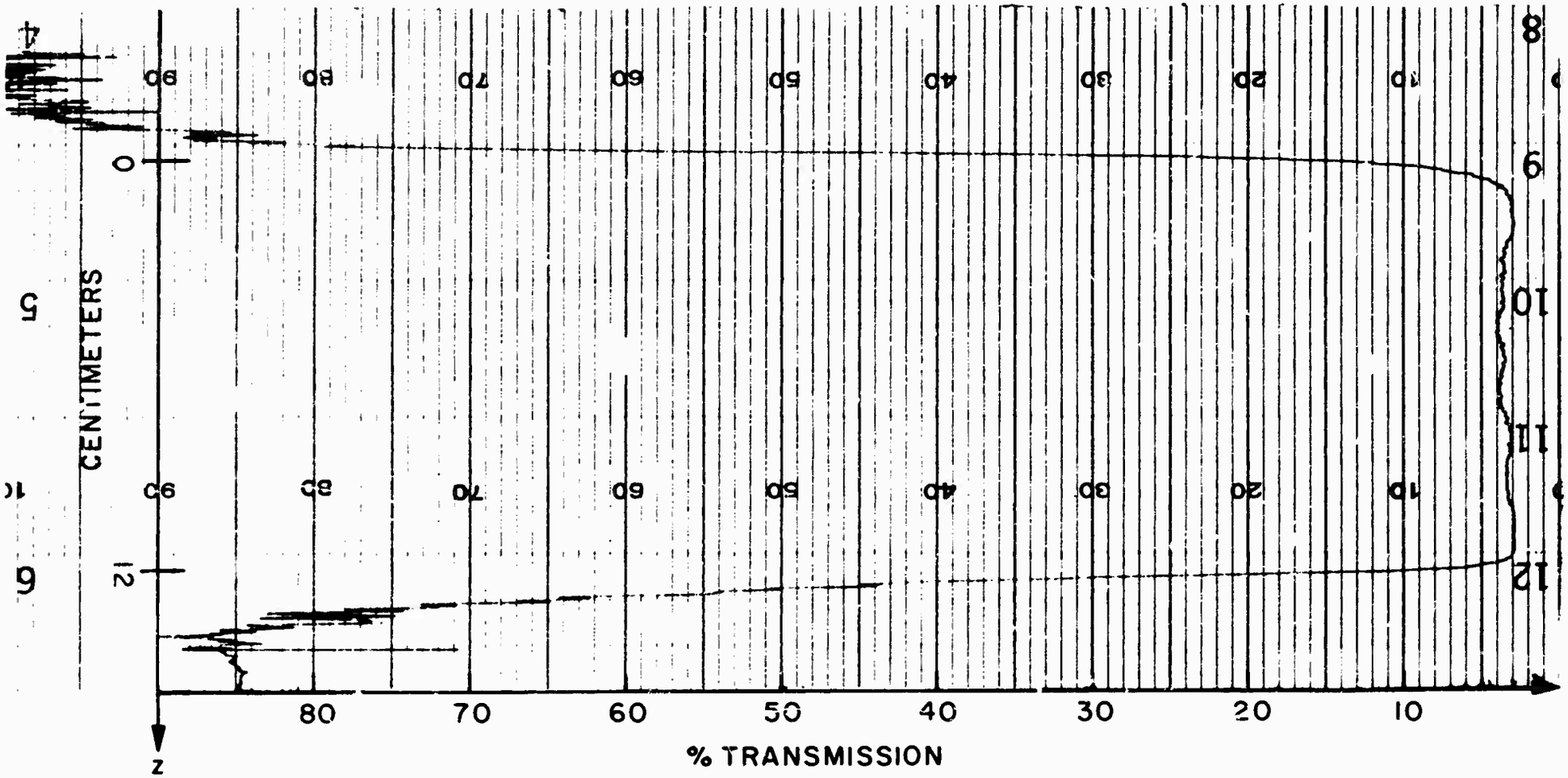

MICRODENSITOMETER SCAN – 1 μ SEC

Figure V-39

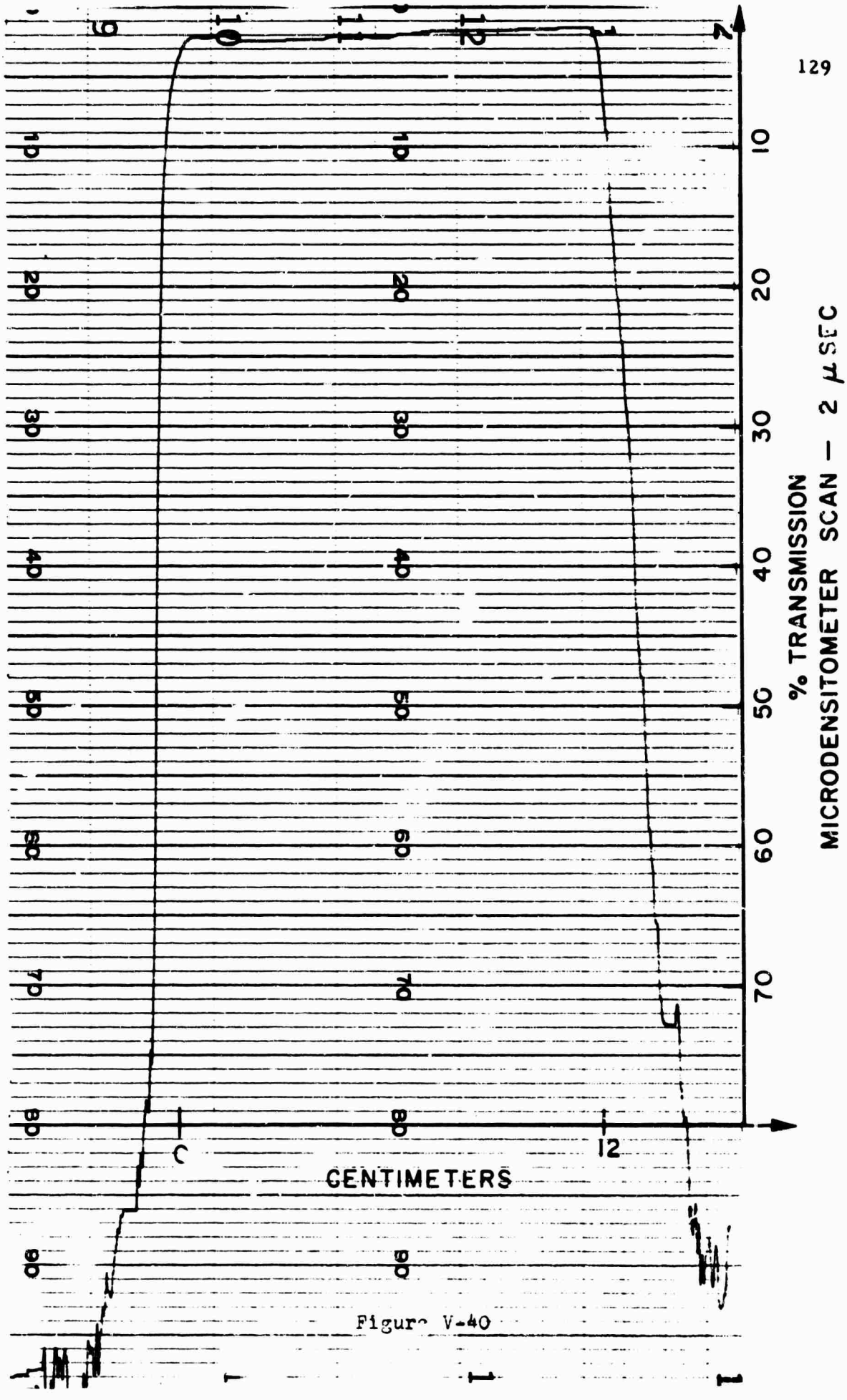
% TRANSMISSION
MICRODENSITOMETER SCAN — 2 μ SEC
10
20
30
40
50
60
70
C
12
CENTIMETERS

Figure V-40

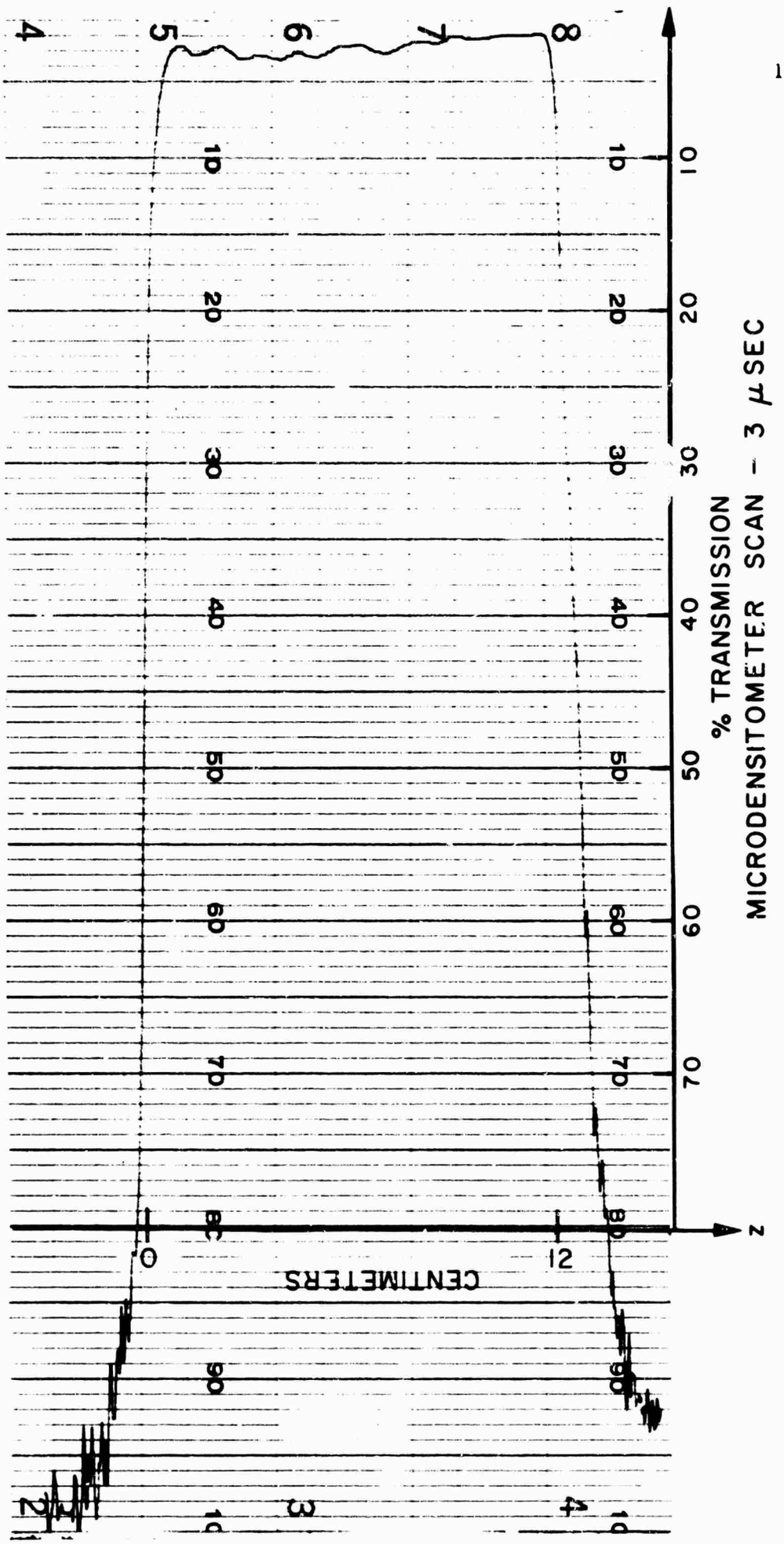
MICRODENSITOMETER SCAN - 3 μSEC
% TRANSMISSION
CENTIMETERS
0
12
z

Figure V-4.

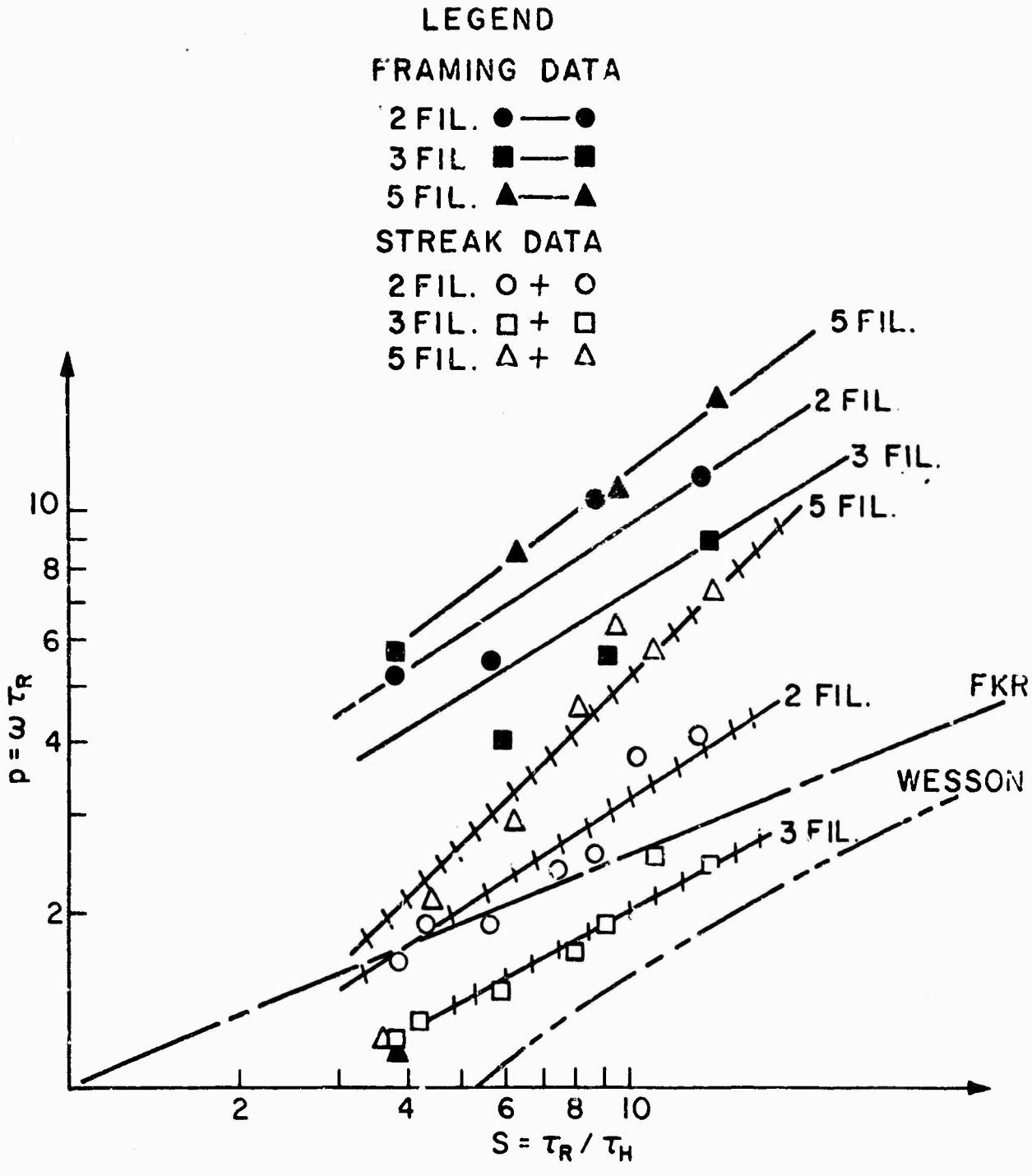
LEGEND
FRAMING DATA
2 FIL.
3 FIL
5 FIL.
STREAK DATA
2 FIL. O + O
3 FIL. □ + □
5 FIL. Δ + Δ
5 FIL.
2 FIL.
3 FIL.
5 FIL.
2 FIL.
FKR
WESSON
3 FIL.
p = ω τR
S = τR / τH
2
4
6
8
10

Figure V- 42

CHAPTER VI

CONCLUSIONS

In this experiment on a Hydrogen toroidal plasma two types of instabilities were investigated.

1. A Rayleigh-Taylor instability was found at neutral gas pressures of about 50 microns of Hg. At this pressure there was significant radial acceleration of the plasma, $G \approx 2 \times 10^{10} m/s^2$, and the instabilities were observed with an S. T. L. image convertor camera looking in the r - ϕ plane .

2. Resistive instabilities were observed in the r - z plane as evidenced by an axially uniform plasma breaking up into a set of filaments. This type of instability was found for neutral pressures above 250 microns Hg and detailed measurements were undertaken at a pressure of 500 microns Hg.

In order to make quantative measurements of the instabilities, a number of plasma parameters were measured. In short, magnetic field, electron density and temperature, induced voltage, plasma current, resistivity, viscosity, and the instablilty growth rate were found.

The magnetic field was measured both inside and outside the plasma bottle. Comparison was made to theoretical models with moderate success. In any event the prediction for average magnetic field linking the plasma agreed with measured values to an error of about 5% . Electron density was measured using the Inglis-Teller method, line half-width relations utilizing H_γ and H_δ, and a sampling of the line profile for H_β . All the techniques yielded electron density values ranging from $4.7 \times 10^{15\#}/cc$ to $6.7 \times 10^{15\#}/cc$ if the H_γ measurement is neglected (this gave $N_e \sim 1.9 \times 10^{16\#}/cc$) .

Resistivity was calculated from V-I probe measurements and also from temperature measurements. Under the same operating conditions, these two techniques yielded values of resistivity within 20% .

Photographs taken of Rayleigh-Taylor instabilities resulted in a wavelength of 1cm. compared to a prediction of 0.93cm. which is about 10% in error. This value represents good agreement, when one consideres that an idealized linear model was used to predict phenomena in an inherently non-linear media, i.e. plasma. Coupled to the study of Rayleigh-Taylor Instabilities was the study of radial motion. This resulted in the verification of a rectangular snowplow model for the radial trajectory of the plasma found by experiment.

Observations of growth behavior of resistive instabilities were two fold. One set of growth rate data and macroscopic behavior was compiled from analysis of framing photographs. A more complete set of data was reduced from quantitative streak photography using a microdensitometer. Resistive instabilities with different wavenumbers were excited by changing the spatial-periodicity of the primary windings. The graph shown in Figure V-42 shows all data: growth rate as determined by framing and streak pictures for the two, three, and five filament configurations.

The curves obtained from framing photographs are grouped much higher than those obtained by streak photograph analysis. The relationship between the curves for different filament configurations is consistant between the two photographic techniques however. One reason that the framing data indicated larger growth rate may be caused by an insufficient gray scale for Polaroid film. This means that the boundry region between plasma and vacuum is more pronounced and makes the filaments appear to be more widely separated than they really are. Examination of such a film with apparent widely separated filaments results in a larger calculated growth rate. On the other hand, data reduction of streak photographs employs a continuous calibration of light intensity versus film density so the problem mentioned above does not exist for this case.

The curves reduced from streak photographs have slopes that fall between those curves due to F.K.R. and J.Wesson. In particular, the magnitude of the experimental curve for three filaments fits between the theoretical curves. The theoretical curves were for a normalized wavenumber of $\alpha = 1$. Interestingly, from Table I of Chapter V-F we see that the three filament case corresponds to $k = 1.045\text{cm.}^{-1}$ Since the plasma width is about 2cm., we have for three filaments a normalized wavenumber of order $\alpha \sim 1$. Values of k for other filament configurations taken from the same table yield normalized wavenumbers of $\alpha \sim 0.5$ and $\alpha \sim 1.6$ for two and five filament cases respectively.

According to the analysis of Chapter II for resistive instabilities the growth rates of the two modes considered are as shown below.

Tearing: $p \sim \alpha^{-2/5} S^{2/5}$; $\alpha < 1$

Rippling: $p \sim \alpha^{2/5} S^{2/5}$; $\alpha > 1$, $\nabla\eta \neq o$

A particular mode can therefore be identified most simply by inspection of the inequality that α must satisfy[29]. Inspection of Figure V-42 shows that curves for two and five filament configurations have larger growth rates than the curve for three filaments ($\alpha \sim 1$). Since $\alpha \sim 0.5 < 1$ for the two filament case, this can be identified as mainly a tearing mode. Also, the five filament case has an $\alpha \sim 1.6 > 1$ and is therefore associated with a rippling mode rather than a tearing mode .

Again, the linearized theory appears adequate to describe the basically non-linear behavior of a resistive instability. The magnitude and functional dependence on α and S appear to be satisfied.

BIBLIOGRAPHY

1. H. P. Furth, J. Killeen, and M. N. Rosenbluth, Phys. Fluids 6, 459 (1963).
2. J. L. Johnson, J. M. Greene, and B. Coppi, Phys. Fluids 6, 469 (1963).
3. H. A. B. Bodin, Nuclear Fusion 3, 215 (1963).
4. I. F. Kvartskhav., et. al., Nuclear Fusion 5, 181 (1965).
5. N. N. Komarov, Nuclear Fusion 3, 174 (1963).
6. N. N. Komarov, et. al., Nuclear Fusion 5, 192 (1965).
7. U. S. Atomic Energy Commission, TID - 23277 (1964) p. VI - 4.
8. L. N. Zadoff and M. Begun, F. H. R. 2242-4, Fairchild Hiller Corp. Republic Aviation Division (1966).
9. M. N. Rosenbluth and C. L. Longmire, Annals of Physics 1, 120 (1957).
10. K. T. Lian, PIBMR - 1030-62 .
11. H. R. Griem, "Plasma Spectroscopy", McGraw-Hill Book Company, New York, (1964) p. 280.
12. H. R. Griem et. al., Nuclear Fusion, 1962 Supplement, Part 2, p. 543.
13. H. R. Griem, A. C. Kolb, and K. Y. Shen, "Stark Broadening of Hydrogen Lines in Plasma", NRL Report 5455.
14. J. Holtzmark, Ann. Physik 58, 577 (1919).
15. S. Glasstone and R. H. Lovberg, "Controlled Thermonuclear Reactions", Van Nostrand Company, Princeton, New Jersey, (1960) p. 180.
16. H. Friedman, M. S. Thesis, Polytechnic Institute of Brooklyn, (1963).
17. J. Milletta, M. S. Thesis, Polytechnic Institute of Brooklyn, (1967).
18. D. R. Inglis and E. Teller, Astrophys. Journal 90, 439 (1939).
19. H. R. Griem, "Plasma Spectroscopy", McGraw-Hill Book Company, New York, (1964) p. 305.
20. H. R. Griem, op. cit. p. 279.
21. H. R. Griem, op. cit. p. 148.
22. H. R. Griem, op. cit. p. 154.
23. H. R. Griem, op. cit. p. 156.

BIBLIOGRAPHY - cont'd

24. L. Sptizer, Jr., "Physics of Fully Ionized Gases", Interscience Publishers, Inc., New York (1956) p. 84.

25. K. Stuart, "Snowplow Model For a Hydrogen Toroidal Plasma", PIBMRI - 1295.2 - 66.

26. W. Marshall, A. E. R. E. Harwell Reports Nos. T/R 2356 and 2419(1958).

27. J. L. Johnson, Private Communication.

28. J. Wesson, Nuclear Fusion 6, 130 (1966).

29. H. P. Furth, op. cit., p. 467.

Unclassified

Security Classification

DOCUMENT CONTROL DATA - R & D

(Security classification of title, body of abstract and indexing annotation must be entered when the overall report is classified)

1 ORIGINATING ACTIVITY (Corporate author) Polytechnic Institute of Brooklyn, Electrophysics Department, Long Island Graduate Center, Route 110, Farmingdale, New York 11735	2a. REPORT SECURITY CLASSIFICATION Unclassified 2b. GROUP

3 REPORT TITLE

EXPERIMENTS ON RESISTIVE INSTABILITIES IN A TOROIDAL PLASMA

4 DESCRIPTIVE NOTES (Type of report and inclusive dates)

Research Report

5 AUTHOR(S) (First name, middle initial, last name)

Kenneth Stuart

6 REPORT DATE	7a. TOTAL NO OF PAGES	7b. NO OF REFS
December 1967	142	29

8a. CONTRACT OR GRANT NO	9a. ORIGINATOR'S REPORT NUMBER(S)
NONR 839(38) b. PROJECT NO ARPA Order No. 529 c. Program Code No. 5730 d.	PIBMRI-1379-67 9b. OTHER REPORT NO(S) (Any other numbers that may be assigned this report)

10 DISTRIBUTION STATEMENT

Distribution of this document is unlimited.

11 SUPPLEMENTARY NOTES	12. SPONSORING MILITARY ACTIVITY
	Advanced Research Projects Agency and Office of Naval Research Washington, D. C.

13 ABSTRACT Visual observations made on a pulsed toroidal plasma indicate that the current carrying plasma sheet breaks up into filaments parallel to the direction of the current and perpendicular to the direction of the magnetic field. This process involves the annihilation and fusion of initially opposite magnetic flux lines and leads to a final configuration which corresponds to a lower energy state. Such a state, however, would not be accessible in the absence of dissipation since its attainment requires slippage of the plasma across magnetic flux lines. The operating mechanism must then be associated with a resistive instability of the type first predicted by Furth, Kileen, and Rosenbluth and also by Coppi, Greene and Johnson in Physics of Fluids, Volume 6, 1963. Observations of resistive instabilities under laboratory conditions is of particular interest because these modes are held responsible for many astrophysical and geophysical phenomena such as solar flares and auroras as well as anomalous diffusion rates in fusion devices.

The experimental setup consists of a plasma filled ring-shaped container of rectangular cross section, where a discharge is induced by means of an iron cored transformer. The time development of the current distribution in the plasma is determined with the help of a combination of magnetic probes and an S. T. L. Image Converter Camera. Optical spectroscopy is used to calculate the temporal variation of electron number density and temperature.

DD FORM 1 NOV 65 1473

Unclassified

Security Classification

14 KEY WORDS	LINK A		LINK B		LINK C	
	ROLE	WT	ROLE	WT	ROLE	WT
Resistive Instability						
Magnetic Probes						
Optical diagnostics						
Electrodeless discharge						